eLife

Reviewed Preprint
v1 • January 13, 2026
Not revised

Reviewed Preprint
v2 • May 21, 2026
Revised by authors

Reviewed Preprint
v3 • June 16, 2026
Revised by authors

For correspondence:
wonpil@lehigh.edu

Competing interests: No competing interests declared

Funding: See page 48

Reviewing editor: Qiang Cui, Boston University, United States

Conformational Variability of HIV-1 Env Trimer and Viral Vulnerability

Yiwei Cao, Wonpil Im
Department of Biological Sciences, Lehigh University, Bethlehem, United States

eLife Assessment

In this **valuable** study, the authors conducted an impressive amount of atomistic simulations with a glycosylated HIV-1 envelope glycoprotein (Env) trimer in a realistic asymmetric lipid bilayer. The aim was to probe how Env transmembrane domain, cytoplasmic tail, and membrane environment influence ectodomain orientation and antibody epitope exposure. The simulations **convincingly** show that ectodomain motion is dominated by tilting relative to the membrane and explicitly demonstrate the role of membrane asymmetry in modulating the protein conformation and orientation, and the results are contextualized well in the revised version. Additional analyses of the authors' deposited MD trajectories could serve as invaluable extensions of this work to probe, for example, for exposure of cryptic epitopes and potential allosteric coupling.

https://doi.org/10.7554/eLife.110107.3.sa2

Abstract

HIV-1 envelope glycoprotein (Env) is critical for viral fusion and entry into host cells and remains a primary target for vaccine and antiviral drug development. Advances in soluble gp140 trimer design have provided insight into the ectodomain structure and dynamics. While structural information is available for the membrane-proximal external region (MPER) and transmembrane domain (TMD), these regions remain comparatively understudied. Furthermore, high-resolution structural information for the cytoplasmic tail (CT), particularly within the context of the intact trimer, is limited and largely uncertain. Additionally, previous studies have typically treated the ectodomain and TMD as separate entities. To investigate the trimeric gp120–gp41 as a complete entity and its structural flexibility, we built a full-length model of the gp120–gp41 trimer that is fully glycosylated with N-linked glycans and embedded in a lipid bilayer, and performed all-atom molecular dynamics simulations. Our results show that the ectodomain maintains a rigid internal structure stable in the prefusion state, whereas the intrinsic flexibility of the MPER enables the ectodomain to adopt a range of tilted orientations, potentially enhancing spatial alignment for receptor engagement. The centrally positioned R696 residue in the TMD interacts with lipid headgroups, ions, and CT residues, resulting in conformational variability in the TMD and perturbations in the surrounding membrane that may facilitate the fusion process. Finally, we demonstrate how simulation trajectories can be leveraged to evaluate the accessibility of antibody epitopes across different regions of the protein.

Introduction

Human immunodeficiency virus type 1 (HIV-1) is the most prevalent strain of HIV responsible for the development of acquired immunodeficiency syndrome (AIDS) (Sharp et al., 2011). The HIV-1 envelope (Env) consists of a host cell-derived lipid membrane and viral glycoproteins that play a crucial role in mediating viral entry into host cells. The Env glycoprotein is initially synthesized in the endoplasmic reticulum (ER) as a precursor gp160 and cleaved by furin into two subunits, gp120 and gp41. The non-covalently associated gp120–gp41 complex is transported to the cell surface in the form of a trimer, where it is subsequently incorporated into the envelope of nascent virions during viral assembly (Wyatt et al., 1998). Exposure of the Env protein is essential for binding to the primary receptor CD4 and co-receptors CCR5 or CXCR4, triggering membrane fusion (Dalgleish et al., 1984; Feng et al., 1996; Huang et al., 1996). However, this exposure also renders the virus susceptible to immune attack. In response to host immune pressure, Env is densely coated with N-linked glycans added during post-translational modification in the ER and Golgi apparatus, which effectively shield vulnerable epitopes from immune recognition (Wei et al., 2003).

Since HIV-1 was identified as the cause of AIDS in the early 1980s, extensive research has been conducted to elucidate the mechanisms of viral infection and immune response. A major advance was the development of soluble gp140 trimers, composing gp120 and the ectodomain portion of gp41, designed to stabilize the prefusion Env trimer for structural and immunological characterization. Native-like Env trimers, such as SOSIP (Sanders et al., 2013), native flexibly linked (NFL) (Sharma et al., 2015), and uncleaved prefusion-optimized (UFO) (Kong et al., 2016) constructs, mimic the structure of the viral spike and serve as valuable antigen targets for developing small molecule inhibitors and broadly neutralizing antibodies (bNAbs). With advances in structure determination techniques, such as X-ray crystallography and cryo-electron microscopy (cryo-EM), numerous high-resolution structures of gp140, both unliganded and antibody-bound, are now available in the Protein Data Bank (PDB). Despite this progress, the remaining portions of gp41, including the membrane-proximal external region (MPER), transmembrane domain (TMD), and cytoplasmic tail (CT), remain relatively understudied.

The MPER is a highly conserved region targeted by several bNAbs, including 10E8, 2F5, 4E10, and Z13e1 (Ofek et al., 2004; Cardoso et al., 2005; Pejchal et al., 2009; Huang et al., 2012). However, in most studies, the MPER is examined as a monomeric peptide bound to antibodies or as part of truncated Env constructs in membrane mimetics such as bicelles and nanodiscs (Rantalainen et al., 2020; Yang et al., 2022; Qi et al., 2025), which do not capture the structure and dynamics of the unliganded MPER in the context of an intact gp120–gp41 trimer embedded in a membrane bilayer. Despite the critical roles of the MPER and TMD in mediating the fusion of viral and host cell membranes (Salzwedel et al., 1999; Miyauchi et al., 2005), they are often excluded from structural studies due to difficulties in crystallization of hydrophobic TM segments while maintaining their native conformations. Therefore, nuclear magnetic resonance (NMR) spectroscopy remains one of the few viable methods for obtaining structural information of the MPER and TMD. However, NMR studies from different research groups have yielded conflicting conclusions regarding the oligomeric state of the TMD. Reported TMD structures include trimeric coiled coils (Dev et al., 2016; Kwon et al., 2018; Piai et al., 2020; Piai et al., 2021), monomeric helices (Apellaniz et al., 2015), and trimers that are not tightly bundled (Reardon et al., 2014).

Similarly, conclusions differ regarding the conformation and orientation of the MPER. Some studies suggest that gp41 bends at the MPER-TMD boundary (around residue 673), with the entire MPER adopting a helical conformation that lies nearly parallel to the membrane (Sun et al., 2008; Kwon et al., 2018), while others show that the C-terminal residues of the MPER form a continuous helix with the TMD (Dev et al., 2016; Chiliveri et al., 2018; Piai et al., 2020; Piai et al., 2021). In addition, the exceptionally long CT plays an important role in facilitating the incorporation of the Env glycoprotein into virions (Checkley et al., 2011). While the CT is known to contain three conserved amphipathic α-helical segments, referred to as lentiviral lytic peptides (LLPs), proposed models differ in the arrangement of LLPs (Murphy et al., 2017; Piai et al., 2021), and the complete structure of the CT and its location in the membrane remain inconclusive.

Molecular dynamics (MD) simulations have been employed to investigate the stability and conformational properties of both monomeric and trimeric TMD. An early study of the trimeric TMD established a foundational understanding of the domain's stability, though it was limited by the computational resources available at the time (Kim et al., 2009). Subsequent work utilizing metadynamics found that the monomeric TMD is characterized by significant conformational plasticity and multiple metastable states, with the individual helix tilting in the bilayer and the midspan arginine (R696) interacting with lipid headgroups in either leaflet (Gangupomu et al., 2010; Baker et al., 2014). Baker et al. also simulated the monomeric TMD on Anton supercomputers, extended sampling to the multi-microsecond time scale, and demonstrated that TMD tilting and the interaction of R696 with lipids lead to local membrane thinning and water defects (Baker et al., 2014). Hollingsworth et al. modeled and simulated trimeric TMD in an asymmetric membrane and observed that TMD tilting and membrane thinning also occurred for the trimeric helical bundle, where water and ions permeated to stabilize the three positively charged R696 residues (Hollingsworth et al., 2018).

Piai et al. determined the NMR structure of a construct comprising the MPER, TMD, and CT, which currently serves as the only PDB structure to include the majority of the CT residues. They complemented this structural work with MD simulations to assess the structural stability of the trimeric MPER–TMD–CT complex (Piai et al., 2021). Recently, Majumder et al. simulated the same MPER–TMD–CT complex and applied a machine learning-based approach to classify the diverse conformational ensemble of the MPER-TMD-CT (Majumder et al., 2025). Maillie et al. combined conventional MD, steered MD, and coarse-grained simulations to demonstrate that interactions between MPER-targeting antibodies and membrane lipids are critical for effective epitope recognition (Maillie et al., 2025). In addition, MD simulations have been extensively applied to characterize the well-studied ectodomain.

Despite these advances, it remains challenging to investigate the gp120–gp41 trimer as an intact entity due to its structural complexity. In this work, we built a model of full-length gp120–gp41 trimer embedded in a lipid bilayer mimicking the lipid composition of the mammalian plasma membrane (van Meer et al., 2008; Sampaio et al., 2011; Ingolfsson et al., 2014; Pogozheva et al., 2022) (Figure 1). We chose this composition as a representative baseline, though we acknowledge that the native viral envelope may exhibit a distinct lipid profile that could influence protein-lipid interactions. Given the limited structural information and consequent uncertainty regarding the conformational organization of the CT, we also generated a CT-truncated model and used it as the primary system for analysis. While host furin cleavage of the gp160 precursor into gp120 and gp41 is a prerequisite for viral infectivity (McCune et al., 1988), native virions also incorporate a fraction of uncleaved gp160 (Zhang et al., 2021). Furthermore, many current immunogen designs, such as NFL and UFO constructs, utilize a covalent linker to stabilize the metastable prefusion conformation (Sharma et al., 2015; Kong et al., 2016). Therefore, we simulated both cleaved and uncleaved trimers to explore how the absence of proteolytic cleavage impacts the conformational landscape. We prepared simulation systems varying in the presence of the cleavage site and CT, as well as the initial position of protein in the membrane. Multiple microsecond-long all-atom MD simulations were performed for each system to explore the motions of individual protein domains and the membrane, and to examine how their conformational variability is affected by the difference in the initial configurations. Our results demonstrate that the ectodomain undergoes substantial tilting relative to the membrane plane while maintaining a rigid internal structure. In contrast, the MPER and TMD display highly diverse conformations, and their structural variations are influenced by the presence of the CT and the initial TMD position in the membrane. Moreover, by analyzing epitopes targeted by various bNAbs, we demonstrate that the simulation trajectories can be leveraged to assess the epitope accessibility.

Results

The ectodomain maintains a rigid internal structure and tilts independently of the TMD

The combination of cleavage state (cleaved vs. uncleaved), sequence length (full-length vs. CT-truncated), and initial TMD position in the membrane (high vs. low) resulted in eight distinct configurations, and we performed three independent 1-μs all-atom MD simulations for each configuration. Simulations trajectories are denoted as $\mathrm{CH}^{\mathrm{CT}}1$, $\mathrm{UL}^{\mathrm{CT}}2$, $\mathrm{CL}^{\Delta\mathrm{CT}}3$, $\mathrm{UH}^{\Delta\mathrm{CT}}3$, etc., where the first letter (C/U) indicates cleaved or uncleaved, the second letter (H/L) indicates the high or

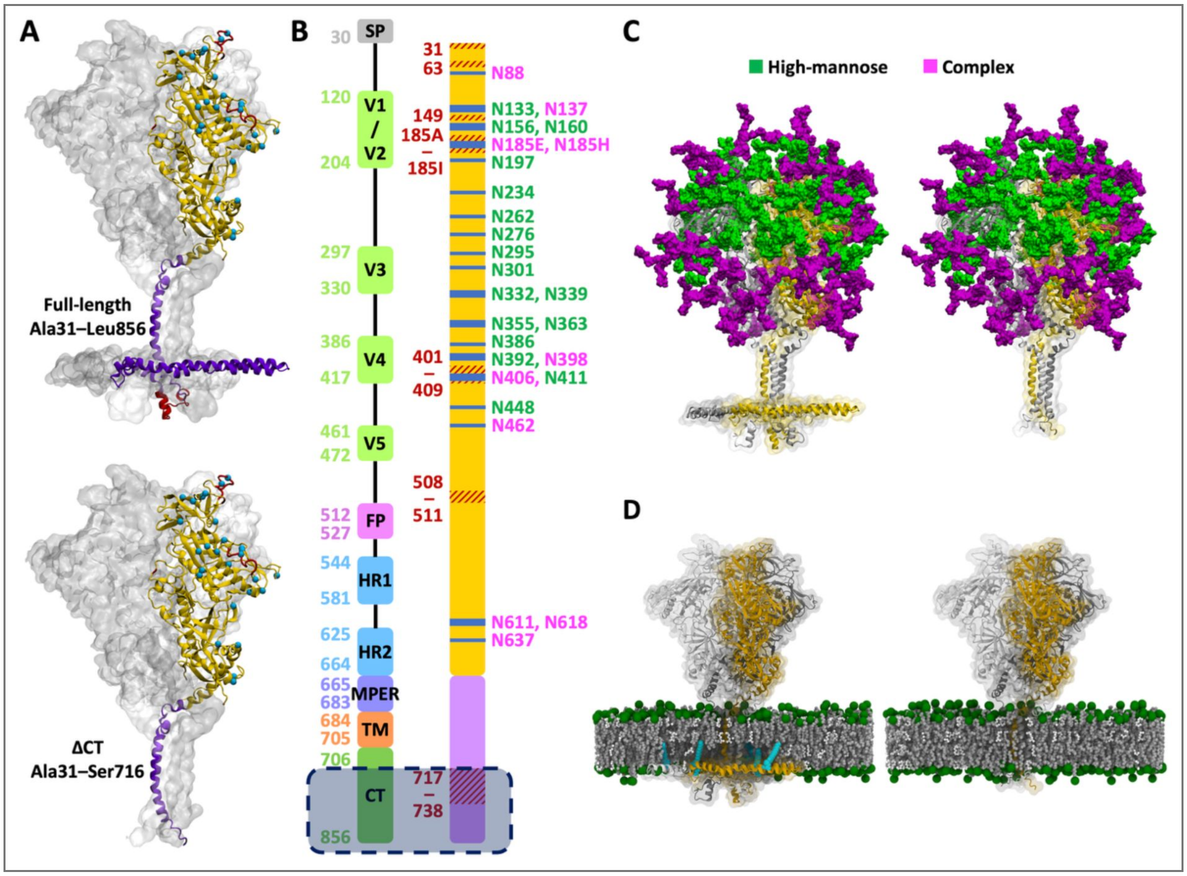

Figure 1. **Model structure of a fully glycosylated full-length HIV Env trimer embedded in a membrane.**

(**A**) The model structure built by combining the cryo-EM structure of the ectodomain (yellow, PDB ID: 6B0N) with the NMR structure of the MPER, TMD, and CT (purple, PDB ID: 7LOI). The full-length model includes residues A31 to L856, while the CT-truncated (ΔCT) model includes residues A31 to S716. The missing loops in the PDB structures are highlighted in red, and the glycosylation sites are marked by cyan spheres. (**B**) Left: assignment of functional domains with boundary residue numbers, including signal peptide (SP), variable regions (V1-V5), fusion peptide (FP), heptad repeats (HR1 and HR2), membrane-proximal external region (MPER), transmembrane domain (TMD), and cytoplasmic tail (CT). Right: missing residues (red) and glycosylation sites (blue). The shaded region at the bottom marks CT residues excluded in the ΔCT model. (**C**) N-linked glycans shown as high-mannose (green) and complex (magenta) types. The full-length model is shown on the left and the ΔCT model on the right. (**D**) Env trimer embedded in a membrane. Lipid headgroups are highlighted by green spheres and glycans are omitted for visual clarity. The palmitoyl groups covalently attached to C764 and C837 are shown in cyan. Molecular illustrations were prepared using Visual Molecular Dynamics (VMD) (Humphrey et al., 1996).

low initial TMD position, CT/ΔCT indicates the presence or absence of the CT, and the numeric suffix specifies the trajectory index among three replicas (Supplementary file 1–Supplementary Table 1).

In all simulations, both the ectodomain and TMD adopted variable orientations relative to the bilayer plane. To quantify the tilting of these two domains, we defined the tilt angles for the ectodomain (θ_{EC}) and TMD (θ_{TM}) (Figure 2A). θ_{EC} is measured between the bilayer normal and the vector from the center of mass (COM) of G594 (on all three protomers) to the COM of D167, while θ_{TM} is measured between the bilayer normal and the vector from the COM of I684 to the COM of V705. Across trajectories, θ_{EC} typically ranges from 0° to 40°, with only 0.7‰ exceeding 40°. Representative structures for different θ_{EC} values are shown in Figure 2A. In contrast to the wide range of θ_{EC}, θ_{TM} generally remained within 0° to 20° with rare excursions to 30° observed in a small fraction of trajectories. Each 1-μs trajectory is divided into four consecutive 0.25-μs intervals, and data points from each interval are distinguished by four different colors (Figure 2—figure supplements 1–4). The variations of θ_{EC} and θ_{TM} over time show that large conformational changes predominantly occurred during the first 0.5 μs, followed by convergence of the θ_{EC} and θ_{TM} distributions during the second 0.5 μs in most trajectories. The temporal evolution of θ_{EC} and θ_{TM} is additionally shown in Figure 2—figure supplements 5–8.

For the CT-truncated systems, the joint probability densities of θ_{EC} and θ_{TM} calculated from the final 0.5 μs of each trajectory are shown in Figure 2B, while those for the full-length systems are shown in Figure 2—figure supplement 9. Although the combined dataset spans a broad range of θ_{EC} (0°–40°) and θ_{TM} (0°–30°), each individual trajectory explored only a portion of this space. For instance, CH$^{\Delta CT}$1 sampled large θ_{EC} with small θ_{TM}, whereas CH$^{\Delta CT}$3 sampled small θ_{EC} with medium-to-large θ_{TM}. Thus, multiple independent simulations are essential to capture a wide region of the conformational space. Notably, no consistent correlation was observed between θ_{EC} and θ_{TM}, either within single trajectories or across all trajectories combined. Pearson correlation coefficients for θ_{EC} and θ_{TM} in single trajectories varied between -0.5 and 0.5, with examples such as CH$^{\Delta CT}$1 and CH$^{\Delta CT}$2 showing similar θ_{TM} but distinct $\mathrm{\theta}_{EC}$ values, and CL$^{\Delta CT}$1 and CL$^{\Delta CT}$3 showing similar $\mathrm{\theta}_{EC}$ but distinct θ_{TM} values. We also calculated the dynamical cross-correlation maps (Ichiye et al., 1991) of Cα atoms for all systems using CPPTRAJ (Roe et al., 2013). The results indicate only very weak correlations between the ectodomain and the TMD (Figure 2—figure supplements 10–13). Although Figure 2—figure supplements 12 and 13 also show low correlations between the ectodomain and the CT, we do not further interpret the coupling of the CT with the other domains due to its structural heterogeneity and the inherent uncertainty in its experimental structure.

Despite the considerable tilting of the ectodomain relative to the membrane, its internal structure remained rigid and well-preserved throughout the simulations. The root-mean-square fluctuation (RMSF) and root-mean-square deviation (RMSD) of the ectodomain were calculated after the snapshots from each trajectory were aligned to the initial structure by maximizing the overlap in the ectodomain. The majority of the ectodomain displayed low RMSF (< 2 Å), and the RMSD stabilized around 4 Å after an initial rise during the first 250 ns (Figure 3A, Figure 3—figure supplement 1). Higher RMSF values were observed only in the residues missing from the cryo-EM structure (PDB ID: 6B0N) (Sarkar et al., 2018), which was used as the template for the ectodomain in model building (these missing residues are highlighted in red in Figure 1A, B), and in part of HR1 (Q551-H564) that forms a flexible loop at the interface between two neighboring protomers.

In addition, the RMSF of the MPER was calculated with the trajectories aligned by the ectodomain. The entire MPER (K665–R683) and the adjacent heptad repeat 2 (HR2) segment (L660–D664) at the C-terminus of the ectodomain exhibited elevated fluctuations. The gp120–gp41 model was built based on the NMR structure in which the MPER adopts a bent conformation consisting of two helices joined by a sharp turn. The resulting trimer widens from the HR2 helix to the midpoint of the MPER (F673) and narrows from F673 to the TMD. However, this specific conformation was not maintained throughout the simulations. We measured the inter-chain distances between the Cα atoms of corresponding residues (G644, E654, D664, and F673) on neighboring protomers to

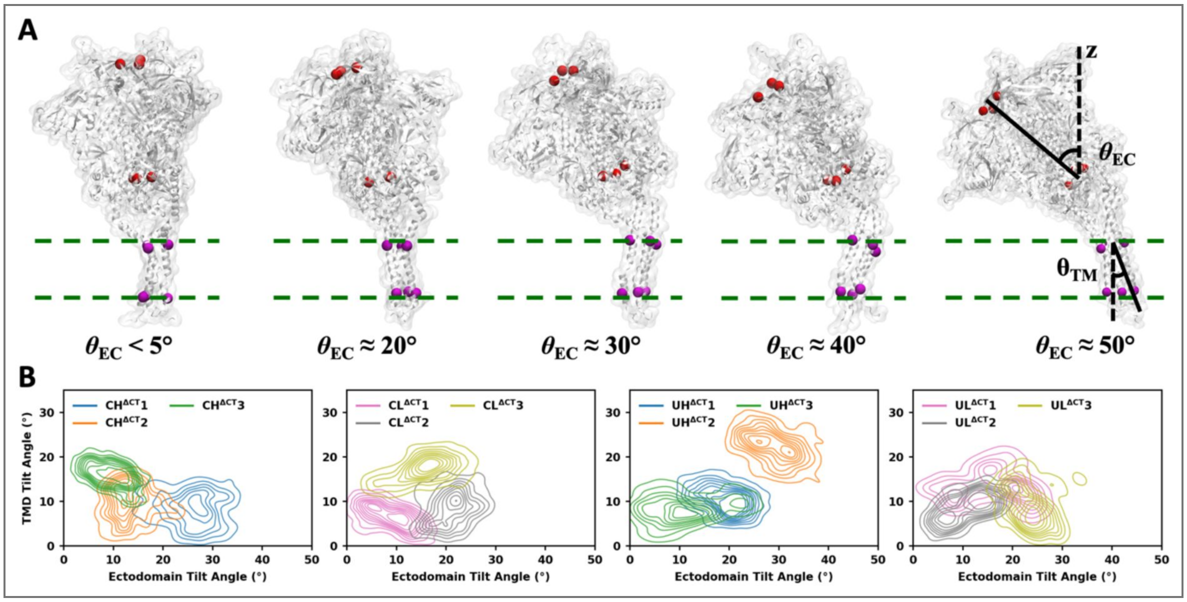

Figure 2. **Tilting motions of the ectodomain and TMD are independent.**

(**A**) Representative structures illustrating different ectodomain tilt angles and the schematic showing how tilt angles are calculated. (**B**) Probability densities of ectodomain and TMD tilt angles, calculated from CT-truncated systems with various initial configurations.

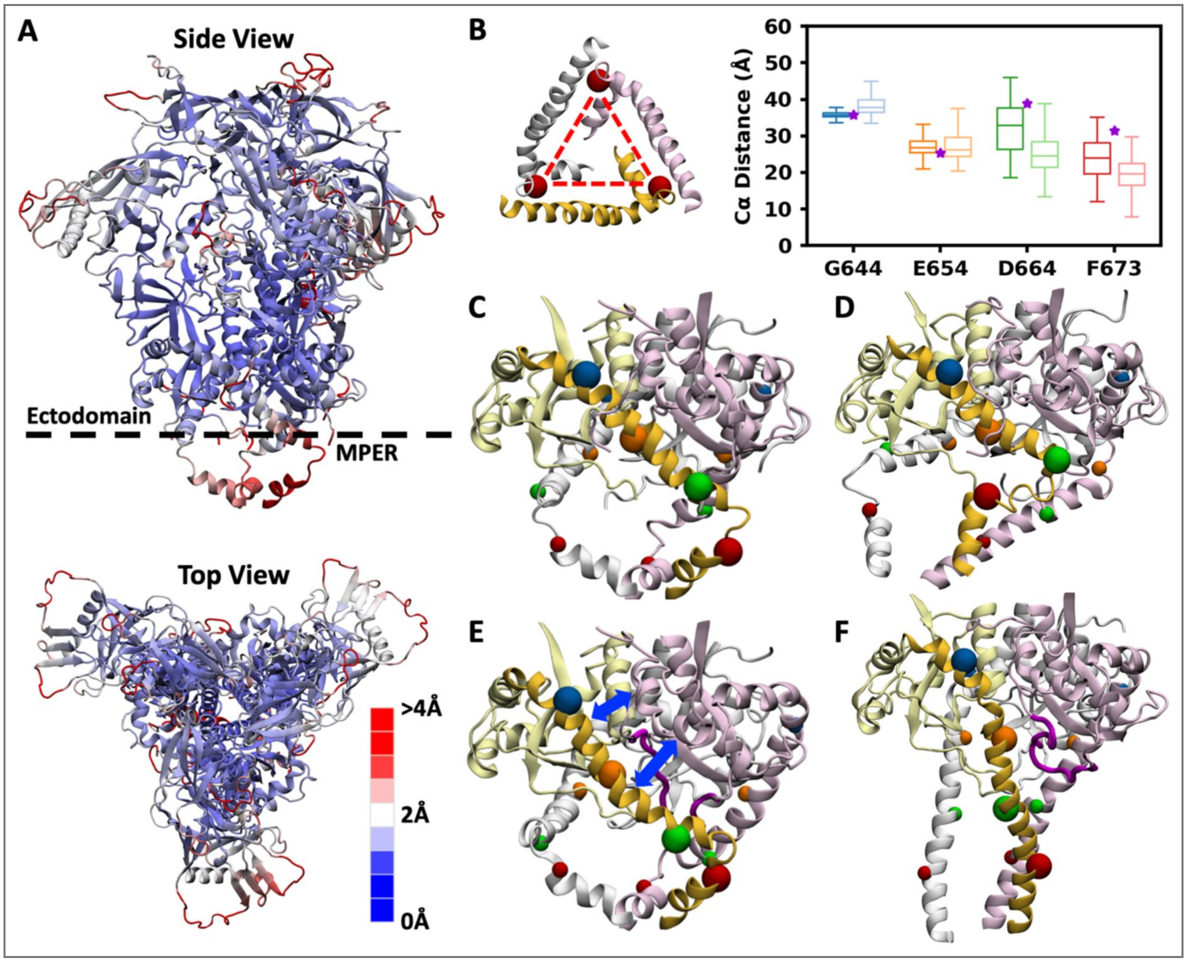

Figure 3. **Ectodomain is rigid, whereas the MPER is highly flexible and adopts diverse conformations.**

(**A**) Top and side views of the ectodomain and MPER in the cleaved system, with RMSF indicated by color. (**B**) Schematic illustrating the calculation of interchain distances and their distributions at the Cα atoms of G644, E654, D664, and F673. For each residue, the distribution from cleaved systems is shown in dark color (left), and that from uncleaved systems is shown in light color (right). represented by solid and transparent colors, respectively. The initial values of interchain distances are marked by purple stars. (**C–F**) Local structures of the ectodomain C-terminus and MPER. The HR2 helix and MPER in one protomer are highlighted in dark yellow, with the Cα atoms of four selected residues marked by blue, orange, green and red spheres. (**C**) The initial conformation and (**D**) representative snapshot from simulations of the cleaved system. (**E**) The initial conformation and (**F**) representative snapshot from simulations of the uncleaved system.

characterize the structural variation along the HR2 helix and the MPER (Figure 3B). The inter-chain distances of G644 and E654 maintained narrow distributions centered on their initial values, while those of D664 and F673 exhibited broader distributions, reflecting inward shifts of three protomers. This effect was more pronounced in uncleaved systems. In cleaved systems, the HR2 helix interacted with residues M530–N543 and L619–N625 of neighboring protomers, which helped to stabilize the bent MPER conformation (Figure 3C, D). However, these interactions were not consistently observed across all protomers and all simulations; therefore considerable conformational variability remained in this region. In uncleaved systems, the closed loop at the cleavage site occupied the space between the HR2 helix and the neighboring protomer, disrupting their interactions and facilitating the inward shift of the HR2 helix (Figure 3E, F).

The energetically unfavorable R696 in the hydrophobic core results in asymmetric, kinked TMD conformations and disrupts membrane integrity

Unlike the predominantly hydrophobic TMDs commonly found in many viral envelope proteins, the gp41 TMD contains multiple charged residues: R683 at the N-terminal boundary, R707 and R709 at the C-terminal boundary, and a central arginine, R696 (Figure 4A). In our simulations, R683 consistently interacted with lipid headgroups in the exoplasmic leaflet, while R707 and R709 interacted with those in the cytoplasmic leaflet, together acting as anchors that secured the TMD within the bilayer. In the NMR structure (PDB ID: 7LOI) (Piai et al., 2021), the side chain of R696 forms a cation-π interaction with the side chain of F699 and a hydrogen bond with the backbone carbonyl group of L692, but it is oriented outward from the helical bundle. When embedded in the bilayer, however, this configuration is energetically unfavorable, as the positively charged side chain directly contacts hydrophobic lipid tails (Cheng et al., 2012). Early in the equilibration stage, the TMD rapidly rearranged to allow R696 residues to interact with more favorable partners, including negatively charged lipid headgroups from either leaflet, ions and water molecules diffusing into the bilayer center, as well as polar and positively charged groups in the CT when present. Once the interactions between R696 residues and their binding partners (lipid headgroups, ions or CT residues) were established, they remained stable with minimal changes throughout the production stage. Because the limited space at the TMD core can only accommodate at most two inward-facing arginine residues, at least one R696 was forced outward to interact with lipid headgroups or CT residues. The differences in arginine orientation and interacting partners gave rise to asymmetric protomer conformations and distinct TMD tilts (Figure 4A–F). When R696 pointed outward, its interactions with lipid head groups or CT residues were strong enough to destabilize the local helix, introducing a kink into the TMD. Representative snapshots from different trajectories illustrate these asymmetric kinked conformations (Figure 4—figure supplements 1–8).

Beyond local deformation of the TMD, R696–lipid interactions perturbed bilayer organization, inducing the translocation of lipid headgroups and water molecules toward the bilayer center (Figure 4G). We calculated the interaction frequencies of each TMD residue with lipid headgroups, lipid tails, and water molecules. The results show that the membrane disruption is persistent as many non-terminal TMD residues maintained frequent contacts with water and lipid headgroups throughout the simulations (Figure 4H). Previously, Kim et al. reported that the inter-chain interactions between protonated R696 gradually diminished over a short simulation time (23 ns), leading to increased crossing angles and reduced bundle length (Kim et al., 2009). Gangupomu et. al and Baker et. al observed that R696 snorkeled toward either exoplasmic or endoplasmic headgroups in simulations of the TMD monomer, resulting in TMD tilting and membrane thinning due to water penetration and lipid headgroups interacting with R696 (Gangupomu et al., 2010; Baker et al., 2014; Baker et al., 2014). These observations are consistent with our findings. Hollingsworth et. al also reported membrane thinning; however, they attributed this effect to interfacial interactions of R683 and R707 with both leaflets and proposed that R696 only interacted with water and ions permeating into the center of the TMD timer (Hollingsworth et al., 2018).

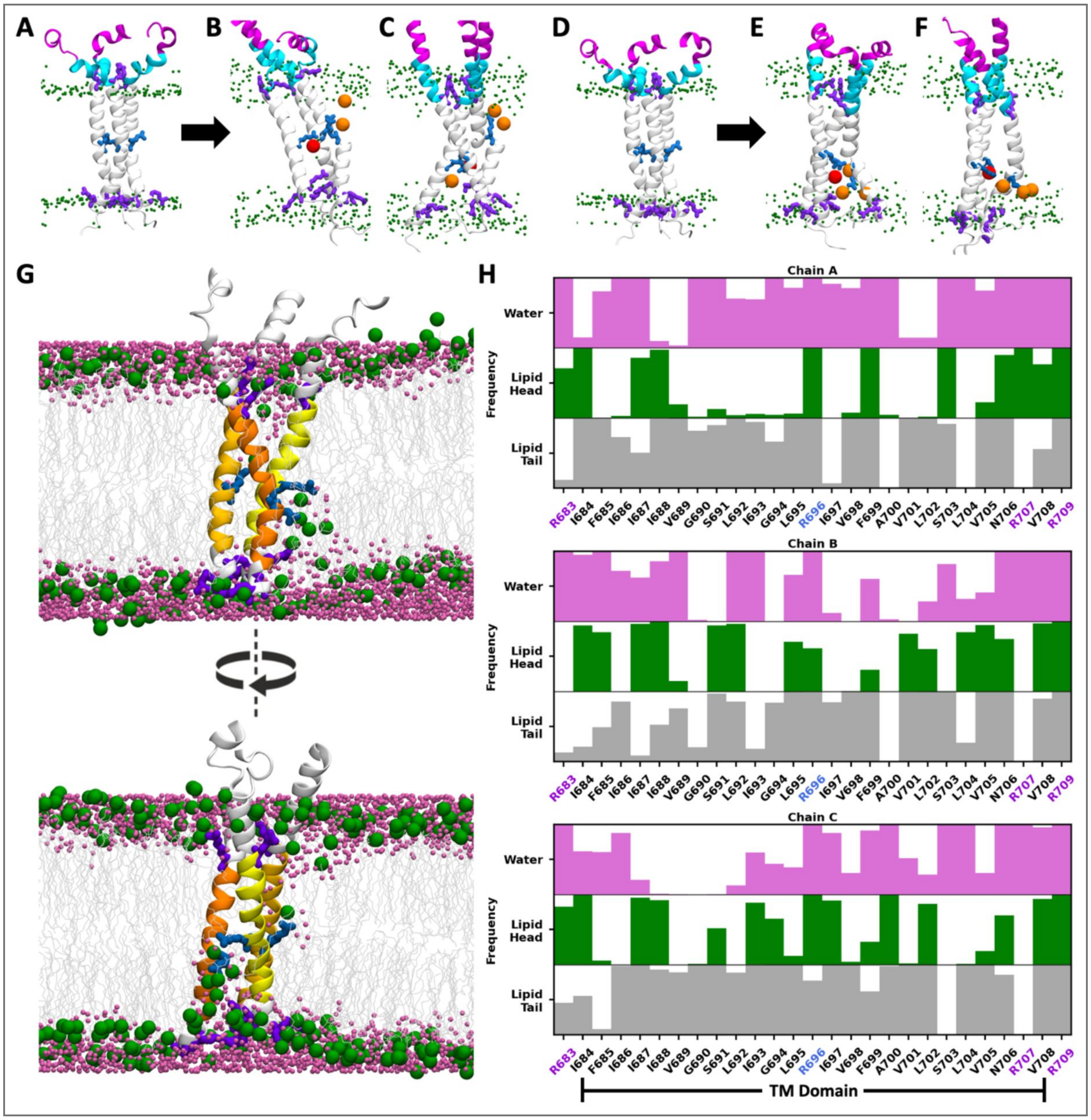

Figure 4. **R696 interacts with lipid headgroups and disrupts membrane integrity.**

(**A–C**) MPER and TMD in the CT-truncated system with the “high” TMD configuration. MPER-N, MPER-C, and TMD are shown in magenta, cyan, and white, respectively. Lipid headgroups, R696, and the residues anchored in the lipid headgroups (R683, R707 and R709) are shown in green, blue, and purple, respectively. Lipid headgroups and ions interacting with R696 are highlighted in orange and red, respectively. (**A**) Initial conformation. (**B, C**) Representative snapshots from different trajectories. (**D–F**) MPER and TMD in the CT-truncated system with the “low” TMD configuration. (**G**) Two side views of the same snapshot where R696 of one protomer interacts with lipid headgroups in the exoplasmic leaflet and R696 of two protomers interact with lipid headgroups in the cytoplasmic leaflet. Lipid headgroups and tails are shown in green and gray, and water molecules in magenta. TMD of three protomers (i.e., chains A, B and C) are shown in light yellow, dark yellow and orange, respectively. (**H**) Frequency of TMD residues interacting with lipid headgroups, lipid tails, and water. For each TMD residue–interacting component pair, the frequency represents the fraction of snapshots in which the heavy atoms of the TMD residue and the corresponding component are within 5 Å. Bar shading reflects this fraction, with fully filled bars indicating 100% and empty bars indicating 0%.

To explore whether R696 exhibits a preference for the exoplasmic versus cytoplasmic leaflet, or interacts with either randomly, we generated two initial structures ("high" and "low") with the TMD positioned at two distinct positions, separated by 4 Å along the membrane normal (see Methods). In simulations initiated from the "high" TMD configuration, R696 residues in three protomers interacted with the lipid headgroups in either leaflet (Figure 4B, C, Figure 4—figure supplements 1, 3) In contrast, in simulations initiated from the "low" TMD configuration, R696 residues interacted exclusively with the headgroups in the cytoplasmic leaflet (Figure 4E and F, Figure 4—figure supplements 2, 4). In the full-length systems, the plate-shaped CT occupies a substantial space within the cytoplasmic leaflet, displacing lipids during model construction. Because the CT is not thick enough to fully span the cytoplasmic leaflet, an empty gap remained between the CT and the exoplasmic leaflet (Figure 1D). Over time, lipids in the exoplasmic leaflet shifted downward while the CT residues moved upward to fill this space, causing local bilayer thinning. Under these conditions, upward-oriented R696 can still interact with the headgroups in the exoplasmic leaflet, but downward-oriented R696 primarily contacted CT residues, with rare cases of lipids migrating upward from the cytoplasmic leaflet to approach the protein. A comparison of all full-length systems (Figure 4—figure supplements 5–8) shows that R696 preferentially adopted downward orientations in the simulations initiated from the "low" TMD configuration (Figure 4—figure supplements 6, 8). In these cases, upward-shifted CT residues interacted with the C-terminal half of the TMD, rather than solely with R696, resulting in deeper burial of the TMD in the membrane. Taken together, these observations suggest that interactions of R696 with lipid headgroups and CT residues may modulate TMD tilt and kink formation during viral entry. However, whether the orientation of R696 dynamically switches between the two leaflets over longer timescales, and whether a preference exists for either leaflet, remain to be examined in future experimental and/or enhanced sampling simulation studies.

MPER adopts diverse conformations, and its exposure depends on both MPER and TMD conformations

Starting from the initial helix-turn-helix conformation consisting of two separate helical segments, the N-terminal half (MPER-N) and the C-terminal half (MPER-C), MPER underwent rapid rearrangements, and a wide variety of conformations were sampled across all trajectories from all systems. In the initial structure, the trimeric MPER was positioned perpendicular to the membrane, with the helical MPER-N tilted inward and MPER-C tilted outward (Figure 4A). Such conformation and orientation were maintained in some trajectories such as $\mathrm{CL}^{\Delta\mathrm{CT}}3$ (the third trajectory of the cleaved, CT-truncated system with the low TMD position, Figure 4—figure supplement 2C). In other trajectories, such as $\mathrm{CL}^{\mathrm{CT}}1$, the helix-turn-helix MPER in one protomer shifted into a horizontal orientation parallel to the membrane surface (Figure 4—figure supplement 6A). In $\mathrm{UL}^{\Delta\mathrm{CT}}1$, the entire MPER adopted a more vertical arrangement, with both MPER-N and MPER-C tilted outward (Figure 4E, Figure 4—figure supplement 4A). We also observed in $\mathrm{UH}^{\Delta\mathrm{CT}}3$ and $\mathrm{UL}^{\Delta\mathrm{CT}}3$ that the HR2 helix in the ectodomain, MPER, and TMD merged into a continuous long helix (Figure 4C, F, Figure 4—figure supplements 3C, 4C). In addition, loss of helical structure within the MPER was common, particularly in the MPER-C region, which often transitioned to a random coil. Therefore, the distinct MPER conformations reported in various experimental studies can be all valid as each captures a possible state within the highly flexible conformational landscape of the MPER. It is noteworthy that the MPER in three protomers can adopt different conformations and orientations, resulting in asymmetric local structures.

Because the MPER is a target of multiple bNAbs, we next examined how its exposure is affected by TMD conformation. As described above, interactions between R696 and lipid headgroups affect the burial depth of the TMD, thereby influencing the positioning of the adjacent MPER. To quantify MPER exposure, we measured the vertical distance from the Cα of F673, approximately the midpoint of the MPER, to the highest point of the neighboring lipid headgroups, denoted by d_{F673}. Positive values indicate that F673 lies above the bilayer surface, and negative values indicate its membrane burial. In the initial "low" and "high" TMD configurations, d_{F673} was 6.1 Å and 9.1 Å, respectively, but it spanned a wide range from -15 Å to 20 Å across simulations (Figure 5A, B, Figure 5—figure supplement 1). Two examples illustrate this variability. In the first example, all three R696 residues interacted with the cytoplasmic leaflet, drawing the TMD deeper into the membrane. Consequently, the entire MPER-C and most of MPER-N were buried in the membrane, with one F673 positioned 11.3 Å below the membrane surface, thus bringing the ectodomain in close proximity to the membrane (Figure 5C, E). In the second example, two R696 residues interacted with the exoplasmic leaflet, while one interacted with the cytoplasmic leaflet. In the protomer with upward-oriented R696, the MPER-N, MPER-C, and TMD formed a continuous helix. As a result, most of the MPER extended outside the bilayer, with d_{F673} reaching 18.0 Å and the ectodomain displaced farther from the membrane (Figure 5D, F).

The d_{F673} distributions across all cleaved CT-truncated systems suggest that d_{F673} tends to be smaller when the simulations start from the “low” TMD configuration (Figure 5B). In both “high” and “low” configurations, the mean d_{F673} calculated from the simulation trajectories is smaller than its value in the initial structure, due to both protein conformational changes and lipid diffusion. In the “low” configuration, d_{F673} decreased by 5.0 Å (from 6.1 Å to 1.1 Å), a slightly larger reduction than in the “high” configuration where d_{F673} dropped by 3.5 Å (from 9.1 Å to 5.6 Å). This indicates that deeper MPER burial arises from a larger-scale protein motion rather than merely from a lower initial placement.

Ectodomain epitopes are conditionally accessible, whereas MPER epitopes are virtually inaccessible in the closed prefusion state

To access the accessibility of epitopes on different regions of the trimeric Env protein in the prefusion state, we quantified how frequent their epitopes were exposed without steric clashes from neighboring protein residues, glycans or membrane lipids. We examined six selected antibodies: PGT128 targeting the V3 loop and the N332 glycan (PDB ID: 5JSA) (Kong et al., 2016); PG9 targeting the V1/V2 loop (PDB ID: 3U2S) (McLellan et al., 2011); VRC01 targeting the CD4 binding site (PDB ID: 4LST) (Zhou et al., 2013); 35O22 targeting the gp120–gp41 interface (PDB ID: 4TVP) (Pancera et al., 2014); and 10E8 (PDB ID: 6VPX) (Rantalainen et al., 2020) and 4E10 (PDB ID: 1TZG) (Cardoso et al., 2005) targeting the MPER (Figure 6A, Supplementary file 1–Supplementary Tables 2–5).

The epitope of PGT128 comprises the V3 loop and the N332 glycan. It is widely recognized that PGT128 binding is mediated by the protein-protein interaction with the V3 loop and the protein-glycan interaction with the N332 glycan, facilitated by its extra-long HCDR3 loop penetrating the glycan shield (Figure 6—figure supplement 1). Due to the absence of defined secondary structures, glycans exhibit greater conformational flexibility than the protein, although the crowded surface of gp120–gp41 may partially restrict the motion of glycans. The N332 glycan must adopt specific conformations to enable interactions with PGT128, whereas most conformations block antibody approach. Additional glycans on N137, N156, and N301 can further occlude the site (Figure 6B). Epitope accessibility for PGT128 varied widely across protomers and trajectories, with many cases exceeding 35%. When considering all trajectories from all systems collectively, approximately half of them exhibited at least one protomer with >35% accessibility (Supplementary file 1–Supplementary Table 2). For instance, in trajectory $\mathrm{CH}^{\Delta\mathrm{CT}}1$, two protomers showed accessibility >40%, whereas in $\mathrm{CL}^{\mathrm{CT}}2$, all three protomers are <5%. The high accessibility frequency observed for the PGT128 epitope aligns with its exceptional potency. As demonstrated by Walker et al., PGT128 is capable of neutralizing approximately 72% of global isolates with a median IC_{50} of ~0.02 μg/mL. This potency is approximately 10-fold greater than that of PG9 and VRC01, though its breadth is lower than the 93% reported for VRC01 (Walker et al., 2011). This comparatively lower breadth may be attributed to strict sequence dependency. Because PGT128 recognition depends on the N332-centered glycan epitope, loss, truncation, or shifting of the N332 glycan to N334 prevents productive engagement regardless of local steric accessibility.

The second antibody, PG9, targets the V1/V2 apex, where binding can be hindered by six glycans, N156, N160, and N185E on the same protomer, and N160, N185E, and N185H on the neighboring protomer (Figure 6—figure supplement 2). In most trajectories, the epitopes on all three

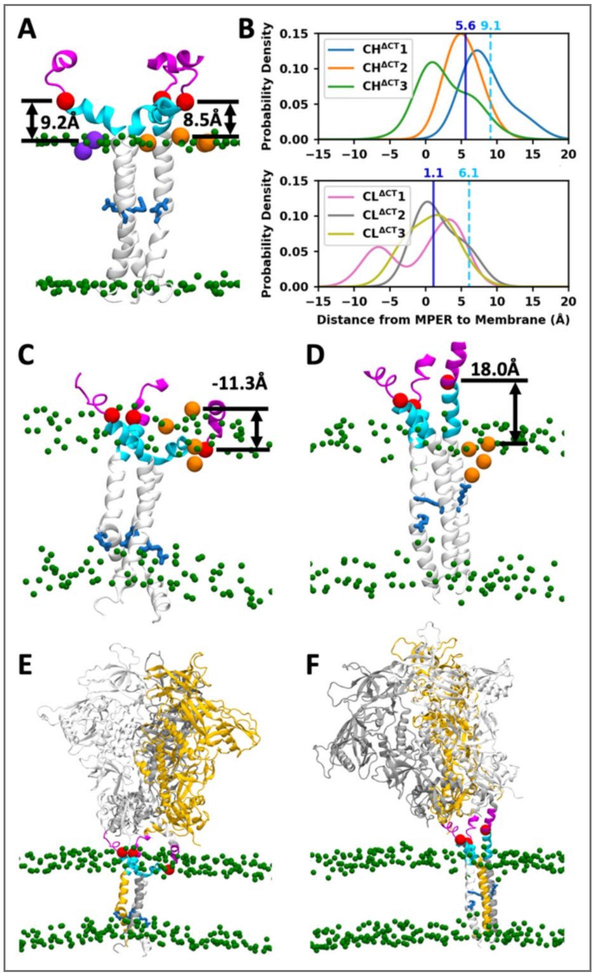

Figure 5. MPER exhibits diverse conformations, and its exposure depends on both MPER and TMD.

(**A**) The initial structure of the $CH^{\Delta CT}$ system, where d_{F673} of two promoters equals 8.5 Å and 9.2 Å. Lipid headgroups are shown in green and R696 in blue. d_{F673} is defined as the distance from the Cα of F673 (red) to the highest among the adjacent lipid headgroups (orange and purple). (**B**) Distribution of d_{F673} in the $CL^{\Delta CT}$ and $CH^{\Delta CT}$ systems. The cyan dashed line indicates the mean d_{F673} of three protomers in the initial structure, and the blue solid line indicates the mean across all data sampled from simulations. (**C, D**) Representative snapshots illustrating the buried (**C**) and exposed (**D**) MPER. (**E, F**) The entire trimer structures corresponding to (**C**) and (**D**), respectively.

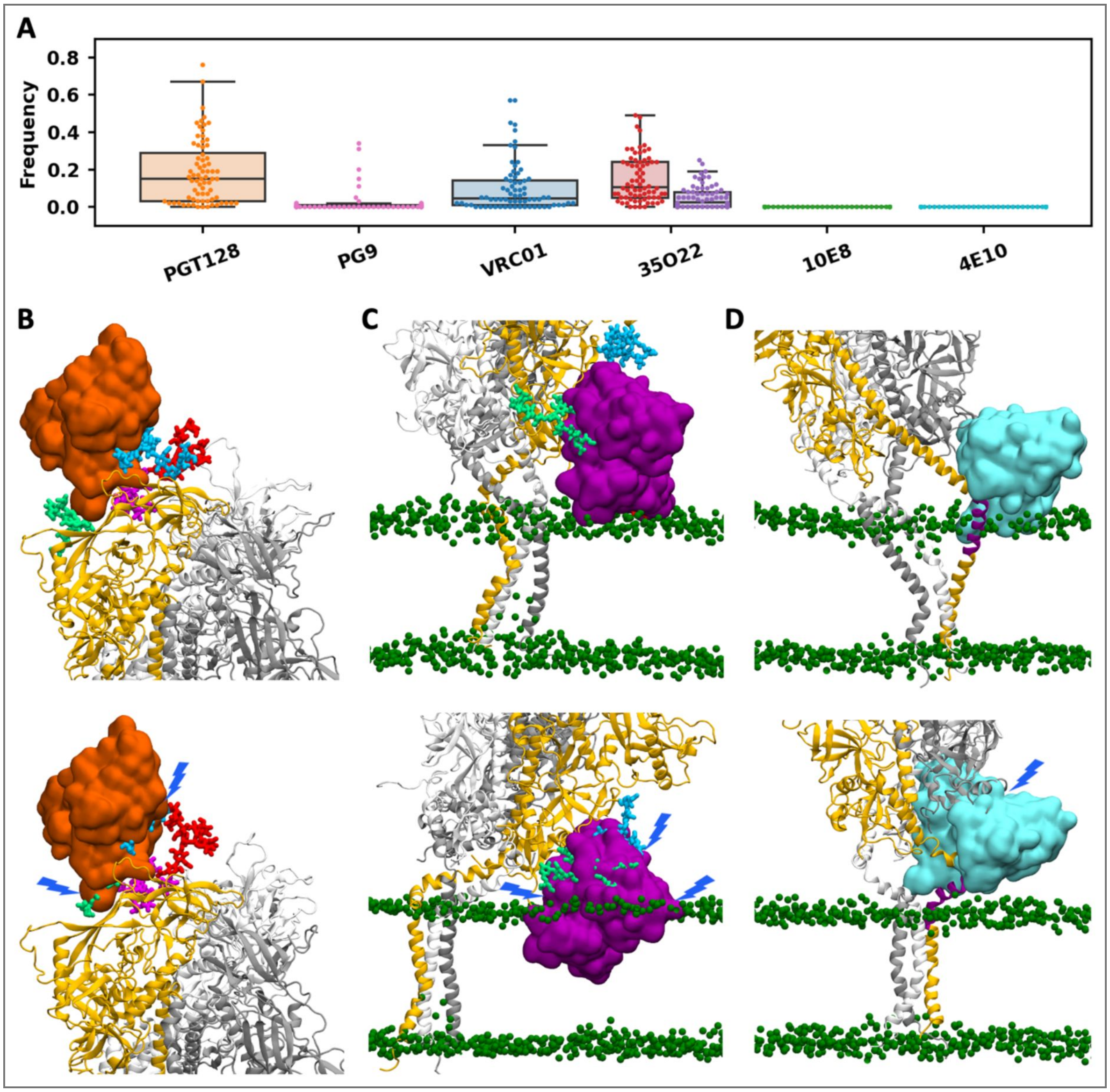

Figure 6. **Antibody epitope accessibility.**

(**A**) The frequency of accessibility. Each marker represents the epitope on one of the three protomers across all trajectories. For 35O22, red indicates the accessibility frequency without considering steric clashes with the membrane, while purple indicates the frequency accounting for clashes with the membrane. (**B–D**) Representative snapshots showing conformations with the epitope exposed (upper) and shielded (lower) for antibodies PGT128, 35O22, and 4E10, respectively. The antibody V_H and V_L domains are shown in surface representation, with lipid head groups in green spheres and glycans that may interfere with the antibody in distinct colors.

protomers were occluded in >95% of the snapshots, with a few exceptions ($\mathrm{CH}^{\Delta\mathrm{CT}}1$, $\mathrm{CH}^{\Delta\mathrm{CT}}2$, and $\mathrm{CL}^{\Delta\mathrm{CT}}3$) where accessibility was non-negligible (Supplementary file 1–Supplementary Table 3). This is consistent with the lower neutralization potency and moderate breadth of PG9, which exhibits a median IC_{50} of ~0.22 μg/mL and a breadth of ~79% (Walker et al., 2009).

The third antibody, VRC01, targets the CD4 binding site where six glycans, N185H, N197, N276, N363, and N462 on the same protomer and N301 on the neighboring protomer, can interfere with antibody binding (Figure 6—figure supplement 3). The VRC01 epitope is moderately to highly accessible on at least one protomer in many trajectories, whereas in some trajectories, the epitopes on all three protomers are nearly completely shielded (Supplementary file 1–Supplementary Table 4). This intermediate accessibility is consistent with the biological requirement for the CD4 binding site to remain periodically available for receptor engagement while maintaining a certain degree of glycan shielding to evade neutralization. The potency of VRC01 is even lower than that of PG9, with a reported median IC_{50} of ~0.32 μg/mL, but it possesses an exceptionally high breadth of ~93% (Wu et al., 2010; Walker et al., 2011).

35O22 targets the gp120–gp41 interface that is not intrinsically membrane-proximal. However, its binding orientation combined with ectodomain tilting can lead to steric clashes between the antibody and the membrane (Figure 6—figure supplement 4). Comparing accessibility with and without including the steric effects of membrane lipids shows that the membrane can substantially hinder 35O22 binding, particularly when the antibody approaches from the direction of ectodomain tilt (Figure 6C). For example, in system $\mathrm{UH}^{\Delta\mathrm{CT}}2$, the accessibility frequencies of the three protomers were 49%, 5%, and 25%, when only the shielding of three glycans (N88, N234, and N618) was considered. When the steric effects of both glycans and membrane lipids were included, the first protomer's frequency dropped from 49% to 1%, while the other two remained essentially unchanged (Supplementary file 1–Supplementary Table 5). Altogether, these results demonstrate that epitope accessibility for this antibody is highly sensitivity to the membrane environment, glycan orientation and ectodomain tilting. This complex dependency provides a structural context for the experimental profile of 35O22, which exhibits high potency with a median IC_{50} of ~0.03 μg/mL, but a relatively limited breadth of ~62% (Huang et al., 2014).

The remaining two antibodies, 10E8 and 4E10, target the MPER. In the PDB structures of 10E8, the epitope is a 17-residue peptide corresponding to residues 671-687 in this work. In the PDB structure of 4E10, the epitope is a 12-residue peptide corresponding to residues 669-680. Superposition of these antibodies onto the initial simulation structure revealed extensive clashes with the protein and glycans linked to N611, N618, and N637 on the neighboring protomer, as well as slight steric clashes with the membrane (Figure 6—figure supplements 5, 6). Using the strict criteria (≤10 heavy-atom clashes with protein/glycan and ≤20 with lipids), no snapshot was identified in which the epitope of either antibody was accessible. Even with relaxed criteria (≤20 heavy-atom clashes with protein/glycan or ≤40 with lipids), accessible cases remained rare, which require either large ectodomain tilts to create space on the opposite side or the MPER transitioning into continuous helices to displace the ectodomain from the membrane (Figure 6D, Figure 6—figure supplements 7–10). Given the extremely low frequency of such specific conformations, MPER epitopes are effectively inaccessible in the prefusion trimer. Though differing in potency — with 10E8 exhibiting a median IC_{50} of ~0.35 μg/mL compared to ~1.93 μg/mL for 4E10 — both antibodies demonstrate extremely high breadth of ~98% (Huang et al., 2012). This extensive breadth is primarily attributed to the high sequence conservation of the MPER across global isolates. The negligible epitope accessibility observed in the prefusion trimer supports the conclusion that these antibodies require the transition of the Env trimer into intermediate states to fully engage their epitopes (Frey et al., 2008).

Discussion

The hydrophobic and flexible nature of the MPER has made it difficult to crystallize, and most structural insights have come from NMR studies. However, structural information for the MPER and TMD has been inconsistent in the literature. For example, one study of the MPER in DPC micelles suggested that it adopted a distorted helical structure lying parallel to the membrane surface (Sun et al., 2008), while NMR studies using gp41 fragments containing part of the MPER and TMD embedded in bicelles or bilayers reached conflicting conclusions. Some proposed a kink (Apellaniz et al., 2015) or a turn (Kwon et al., 2018) between the MPER and TMD, whereas others suggested that the MPER and TMD formed a continuous helix aligned perpendicular to the membrane (Dev et al., 2016; Chiliveri et al., 2018). In the NMR structure (PDB ID: 7LOI) used to build our model structure, a kink appears between the MPER and TMD, along with a turn in the middle of the MPER (Fu et al., 2018; Piai et al., 2021). Crystal structures of MPER peptides bound to various antibodies show that in addition to the helix-turn-helix conformation, the MPER can also adopt alternative structures in which the MPER-C remains helical while part of the MPER-N becomes unstructured (Williams et al., 2017). Such variability underscores the intrinsic structural flexibility of the MPER, with each experimental method likely capturing only a subset of possible states under specific conditions. In this study, we employed all-atom MD simulations to sample a broader conformational landscape and gain a more comprehensive view of the structural heterogeneity of the MPER. Our results reveal that the MPER can adopt virtually all of the conformations reported experimentally. This is consistent with the all-atom simulations of MPER–TMD–CT and MPER–TMD in an asymmetric membrane conducted by Majumder et al., which likewise demonstrated multiple conformational states, including helix-turn-helix and extended helical conformations (Majumder et al., 2025). While MPER plasticity has been linked to its role in virus-host membrane fusion because it enables the ectodomain and TMD to adopt distinct orientations during large-scale structural rearrangements (Salzwedel et al., 1999), our results show that this flexibility is already inherently present in the prefusion state. At this stage, the MPER functions as a flexible hinge that facilitates ectodomain tilting, which can be critical for the spatial alignment of the CD4-binding site with the host receptor for efficient receptor engagement.

Comparison of the full-length and CT-truncated systems shows that the primary difference arises from changes in the lipid bilayer, particularly in the exoplasmic leaflet, whereas differences in protein conformation and dynamics are less evident. Previous experimental studies have reported that mutations of TMD residues and CT truncation can substantially affect the antigenicity of the ectodomain (Edwards et al., 2002; Chen et al., 2015; Dev et al., 2016). However, the ectodomain remains relatively rigid in our simulations for both full-length and CT-truncated systems. It is unclear whether this behavior reflects insufficient conformational sampling or potential artifacts associated with the model structures. Structural information for the CT is very limited, and the NMR structure (PDB ID: 7LOI) was the only available CT structure at the time the simulation systems were constructed. As a result, the extent to which this structure represents the native CT conformation remains uncertain. Additional experimental structural characterization of the CT will be important for achieving a more complete understanding of its functional role. Similar limitations apply to other modeled regions where structural information is incomplete, including missing loops in the ectodomain, the cleavage site and the HR2 region where two PDB structures (IDs: 6B0N and 7LOI) were merged. These regions introduce additional uncertainty, and the extent to which they influence the interpretation of our results remains an open question.

Our analysis of the ectodomain and TMD coupling indicates that the motions of these two domains are largely independent. This observation does not contradict experimental studies demonstrating functional coupling between the TMD, CT, and the antigenic profiles of Env (Chen et al., 2015; Dev et al., 2016). Munro et al. proposed that unliganded Env is intrinsically dynamic, transitioning among three distinct prefusion conformations: a closed ground state (predominant), a transient state, and a CD4-/co-receptor-stabilized state. Both laboratory-adapted and clinically isolated strains can spontaneously transition among these three states, although their relative occupancies differ (Munro et al., 2014). It is therefore possible that TMD mutations or CT truncation alter the equilibrium distribution among these states, thereby affecting the epitope exposure, particularly for epitopes that are occluded in the closed ground state while exposed in the CD4-/co-receptor-stabilized state. However, transition among these three states occur on millisecond-to-second timescales (Munro et al., 2014). Our simulations on microsecond timescales primarily capture conformational variations within the closed ground state and suggest that the MPER acts as a hinge, providing substantial flexibility that enables the ectodomain and

TMD to move independently while Env remains in the closed ground state. Enhanced sampling methods could be applied to more thoroughly explore the conformational landscape, including not only variations within the closed ground state but also transitions among the closed ground, transient and CD4-/co-receptor-stabilized states.

In addition to the limitations inherent to protein structure modeling, the choice of lipid composition remains an open question. In this work, we selected an asymmetric mammalian plasma membrane because it is one of the 18 complex biomembrane systems we previously studied (Pogozheva et al., 2022), and among them, it provides the closest available approximation to the HIV membrane. Nevertheless, experimental studies have reported differences in lipid composition between HIV virions and the host plasma membrane (Aloia et al., 1993; Brugger et al., 2006; Huarte et al., 2016; Mucksch et al., 2019; Tomishige et al., 2023). Although we do not anticipate that our main conclusions regarding Env domain motions and MPER flexibility would change substantially, evaluating the influence of lipid composition represents an important direction for future work.

To probe antibody recognition, we assessed epitope accessibility using snapshots extracted from simulation trajectories. Unlike static experimental structures, this approach incorporates protein dynamics and the influence of glycans and membrane lipids, yielding a frequency-based measure of how often each epitope is accessible rather than a binary classification. It is worth noting that viral glycans vary highly in both site occupancy and the specific glycoforms present at each glycosylation site, as indicated by mass spectrometry data (Behrens et al., 2016; Cao et al., 2017). For structure modeling, however, we assumed full occupancy at all glycosylation sites and selected a single representative glycoform per site. As a result, the estimated glycan shield may not fully reflect the *in vivo* situation. Furthermore, this analysis is based on geometric and steric criteria without accounting for potential conformational adaptations of gp120–gp41, antibodies, or the membrane. The resulting accessibility frequencies should therefore be interpreted as an approximation rather than a definitive indicator of binding competence. Our results indicate that ectodomain epitopes, though heavily shielded by glycans, can still become transiently accessible in the closed prefusion state. The frequency provides a quantitative measurement of how vulnerable each epitope is to antibody binding. When estimating steric clashes between the membrane and antibodies, we adopted relaxed cutoffs to account for lipid fluidity, but the membrane due to fast lipid dynamics may in reality accommodate even greater steric overlap. Although the MPER can transiently extend out of the membrane when gp120–gp41 remains in the prefusion state, MPER-targeting antibodies encounter substantial steric hindrance from the bulky gp120 subunit, surrounding glycans, and the membrane throughout nearly all simulations. Therefore, these antibodies are unlikely to adopt the orientations required to bind their epitopes, which is consistent with experiment studies suggesting that MPER-targeting antibodies bind effectively only after the gp120–gp41 trimer undergoes major conformational rearrangements toward a fusion-intermediate or post-fusion state (Frey et al., 2008; Alam et al., 2009; Chen et al., 2014; Lee et al., 2016). Shehata et al. also built a model of the full-length gp120–gp41 trimer embedded in a lipid bilayer and performed all-atom simulations, in which a tilting motion of the ectodomain was observed. Based on the analysis of accessible surface area using different probe radii, they reported that antibody epitopes on the ectodomain are largely shielded by glycans, while the MPER epitope is mainly occluded by the membrane, with tilt angles above 30° required to achieve greater MPER exposure (Shehata et al., 2025).

Overall, the data presented here demonstrate that structural modeling integrated with all-atom MD simulations can be applied to complex biomolecular systems like the gp120–gp41 trimer embedded in a membrane bilayer, which enables detailed characterization of protein dynamics at the molecular level and facilitates the investigation of antigen-antibody interactions, thereby offering potential guidance for rational vaccine design.

Materials and methods

System building

Modeling of full-length gp120–gp41 trimer

The full-length gp120–gp41 trimeric model was generated by combining the crystal structure of the ectodomain with the NMR structure containing the MPER, TMD, and CT (Figure 1A, Figure 1—figure supplement 1A). Considering structure resolution and the number of missing residues, we selected the crystal structure of a soluble Env trimer exhibiting a closed-form, native-like prefusion conformation (PDB ID: 6B0N) (Sarkar et al., 2018). This structure contains the entire ectodomain, including the V1-V5 loops, fusion peptide (FP), heptad repeat 1 (HR1), and heptad repeat 2 (HR2) (Figure 1B). In contrast to the ectodomain well represented in the PDB with numerous crystal and cryo-EM structures, structural data for the MPER, TMD and CT are scarce. For these regions, we chose the NMR structure (PDB ID: 7LOI) (Piai et al., 2021) containing the MPER, TMD, and CT. Both 6B0N and 7LOI are trimeric structures and the C-terminus of 6B0N includes five residues (L660–D664) overlapping with the N-terminus of 7LOI. Measurement of the Cα–Cα distances for D664 in the three protomers revealed that the inter-protomer spacing in 7LOI (16 Å) was significantly shorter than in 6B0N (39 Å) (Supplementary file 1–Supplementary Figure 1A). To reconcile this difference, we performed short MD simulations on 6B0N with residues E32–Q640 fixed and a distance restraint applied to D664 to reduce the Cα–Cα distance to 33 Å. Similarly, for 7LOI, residues I675–L856 were fixed, and a distance restraint was applied to D664 to increase the Cα–Cα distance to 33 Å (Supplementary file 1–Supplementary Figure 1B). These two adjusted structures were then combined by aligning the overlapping residues (Supplementary file 1–Supplementary Figure 1C). The missing loops in 6B0N (T63, D149, E185A–N185I, S401–G409) and the unresolved region between the TMD and CT in 7LOI (F717–G738) were grafted from a modeled structure generated by I-TASSER (Yang et al., 2015).

6B0N is a native flexibly linked (NFL) trimer in which the furin cleavage site ^{508}REKR^{511} is substituted with a 10-residue linker ^{508}GGGGSGGGGS^{511}, but the underlined residues are unresolved in the structure. To construct the cleaved gp120–gp41 model, we removed the initial “GG” and final “S” from 6B0N. For the uncleaved gp160 model, we closed the cleaved loop by adding ^{508}REKR^{511} back to the structure. If we simply connect G507 and A512 without adjusting the conformation of flanking loops on both sides of the cleavage site, two neighboring protomers become entangled, yielding a knot-like fold (Supplementary file 1–Supplementary Figure 2A, B). In 6B0N, the helical HR2 region lies at the C-terminus of each protomer, allowing it to thread through a loop formed by the neighboring protomer (Supplementary file 1–Supplementary Figure 2C). However, in the context of the full-length gp120–gp41, it is implausible that the three protomers are entangled as it does not conform to a realistic folding pathway. Therefore, we performed short MD simulations with restraints to adjust the conformations of the flanking loops and the HR2 helix before closing the loop with REKR fragment (Supplementary file 1–Supplementary Figure 2D, E).

Finally, two mutations (S764C and S837C) were introduced in the CT to restore the palmitoylation sites, and lipid tails oriented towards the hydrophobic core of the bilayer were then attached to the palmitoylation sites using the PDB Manipulation module in CHARMM-GUI (Jo et al., 2008; Jo et al., 2014; Park et al., 2023) (Figure 1D). In addition to the full-length model, we built the CT-truncated model by removing modeled residues F717–G738 that are originally unresolved in the PDB structure 7LOI, and residues E739–L856 that form the large CT plate.

Glycosylation

N-linked glycans were modeled using *Glycan Reader & Modeler* (Jo et al., 2011; Park et al., 2017; Park et al., 2019) in CHARMM-GUI. The reported mass spectrometry (MS) experiments have revealed the probability of different types of N-linked glycans at each glycosylation site (Behrens et al., 2016; Cao et al., 2017). For each site, we selected the one with the highest probability. As the MS data provide only the glycan type (high-mannose, hybrid, and complex) and composition (number of each monosaccharide unit), a representative isomer was chosen whenever multiple isomers corresponded to the same composition. For example, HexNAc(2)Hex(9), i.e., the Man_9 glycan, has a single isomer, whereas HexNAc(2)Hex(8), i.e., the Man_8 glycan, has multiple isomers depending on which non-reducing terminal mannose is trimmed from Man_9. For complex N-linked glycans, a single composition can correspond to multiple isomers differing in the number of branches on the α1-3 and α1-6 arms and in the placement of non-reducing terminal neuraminic acid (Neu5Ac). In the absence of linkage-specific information, one isomer was arbitrarily selected from available possibilities. The selected glycan sequences for the 27 glycosylation sites in each promoter are summarized in Supplementary file 1–Supplementary Table 6. The selected glycan sequences were represented in the Glycan Reader Sequence format (Jo et al., 2011; Park et al., 2017) and added to the corresponding glycosylation sites using the *Glycan Reader & Modeler* graphical interface.

Membrane

The full-length and CT-truncated models were embedded into an asymmetric lipid bilayer with the lipid composition corresponding to a mammalian plasma membrane (van Meer et al., 2008; Sampaio et al., 2011; Ingolfsson et al., 2014; Pogozheva et al., 2022), which consists of phosphatidylcholine (PC), phosphatidylethanolamine (PE), phosphatidylinositol (PI), phosphatidylserine (PS), phosphatidic acid (PA), sphingomyelin (SM), cholesterol (CHOL), and glucosylceramide (GlcCer). In the CT-truncated system, the exoplasmic and cytoplasmic leaflets contain similar numbers of lipids, despite differences in composition. In the full-length system, the cytoplasmic leaflet contains approximately 100 fewer lipids than the exoplasmic leaflet due to the space occupied by the CT. The lipid composition is summarized in Supplementary file 1–Supplementary Table 7. Membrane systems were constructed using CHARMM-GUI Membrane Builder, which provides a user-friendly graphical interface for selecting lipid types and defining their numbers in each leaflet (Jo et al., 2007; Jo et al., 2009; Wu et al., 2014; Lee et al., 2016; Lee et al., 2019). Although it is recognized that the charged residues R683, R707, and R709, flanking the N- and C-termini of the TMD, are anchored within the lipid headgroups, there remains flexibility to shift the TMD slightly up or down within the membrane. Assuming the lipid bilayer is aligned parallel to the xy-plane, the protein was positioned at two distinct depths along the z-axis, differing by approximately 4 Å, referred to as the “high” and “low” TMD configurations. To examine whether this subtle difference in the initial configurations leads to distinct conformational changes during simulations, we initiated independent simulations from each configuration. The glycoprotein-membrane system was solvated in a box of approximately 210 × 210 × 260 $Å^3$ using the TIP3P water model (Jorgensen et al., 1983), and KCl was added at a concentration of 0.15 M to neutralize the system. The final simulation input files were automatically generated by CHARMM-GUI.

Simulation details

The CHARMM36(m) force field (Guvench et al., 2009; Klauda et al., 2010; Raman et al., 2010; Guvench et al., 2011; Huang et al., 2017) was used for proteins, carbohydrates, and lipids. The total number of atoms is approximately 1,100,000 (including ~300,000 water molecules and ~1,700 ions), with small variations between systems. van der Waals interactions were smoothly switched off over 10–12 Å using a force-based switching function (Steinbach et al., 2004), and long-range electrostatic interactions were calculated using the particle-mesh Ewald method (Essmann et al., 1995) with a mesh size of ~1 Å. All simulations were performed using GROMACS (Van Der Spoel et al., 2005). Bond lengths and angles involving hydrogens were constrained using the LINCS algorithm (Hess et al., 1997). The system was equilibrated in the canonical (NVT) ensemble at 310.15 K for 2 × 1.25 ns with a 1-fs time step using the Berendsen thermostat (Berendsen et al., 1984) (coupling constant τ_t = 1 ps), and then switched to the isothermal–isobaric (NPT) ensemble for 1.25 ns with a 1-fs time step, followed by 3 × 5 ns with a 2-fs time step using the Berendsen thermostat (τ_t = 1 ps) and barostat (reference pressure = 1 bar, coupling constant τ_p = 5 ps, compressibility = 4.5×10^{-5} bar^{-1}). Positional and dihedral restraints were applied to proteins, glycans, and lipids, with force constants progressively reduced over successive intervals (Supplementary file 1–Supplementary Table 8). In the production runs, temperature was maintained using the Nosé–Hoover thermostat (Hoover, 1985; Nosé, 2006) and the pressure coupling was applied using the semi-isotropic Parrinello–Rahman barostat (Parrinello et al., 1981; Nosé et al., 2006). A 4-fs time step was used with the hydrogen mass repartitioning technique (Hopkins et al., 2015) and all restraint potentials were removed. The Python library MDTraj (McGibbon et al., 2015) was used to analyze the simulation trajectories.

Assessment of antibody epitope accessibility

We selected six antibodies based on epitope locations and the availability of PDB structures containing both antibody and epitope: PGT128 targeting the V3 loop and the N332 glycan (PDB ID: 5JSA); PG9 targeting the V1/V2 loop (PDB ID: 3U2S); VRC01 targeting the CD4 binding site (PDB ID: 4LST); 35O22 targeting the gp120–gp41 interface (PDB ID: 4TVP); 10E8 (PDB ID: 6VPX) and 4E10 (PDB ID: 1TZG) targeting the MPER. For each antibody–epitope complex, TM-align (Zhang et al., 2005) was used to identify the optimal alignment between the epitope from the PDB structure and each protomer of the trimeric protein. The resulting rotation matrix was applied to position the antibody relative to each protomer. Steric clashes were quantified by counting any heavy atoms of the protein, glycans, or lipids within 2 Å of a heavy atom of the antibody. An epitope was classified as occluded by the protein and glycans if more than 10 heavy-atom clashes occurred with these components. To account for the inherent flexibility and fluidity of the membrane, a more permissive threshold was adopted for lipids: an epitope was classified as occluded by the membrane only if more than 20 lipid heavy-atom clashes were detected. To calculate the frequency of epitope accessibility, snapshots were extracted from simulation trajectories, and then structural alignment and assessment of steric clashes were performed on each snapshot.

Data availability

The modeled structures, force field parameters, and GROMACS input files are available on Zenodo [*https://doi.org/10.5281/zenodo.17259909*]. The code used in this article can be found at *https://doi.org/10.5281/zenodo.17259951*. The simulation trajectories can be found at *https://doi.org/10.5281/zenodo.18853902*, *https://doi.org/10.5281/zenodo.18854615*, and *https://doi.org/10.5281/zenodo.18854639*.

Figure supplements

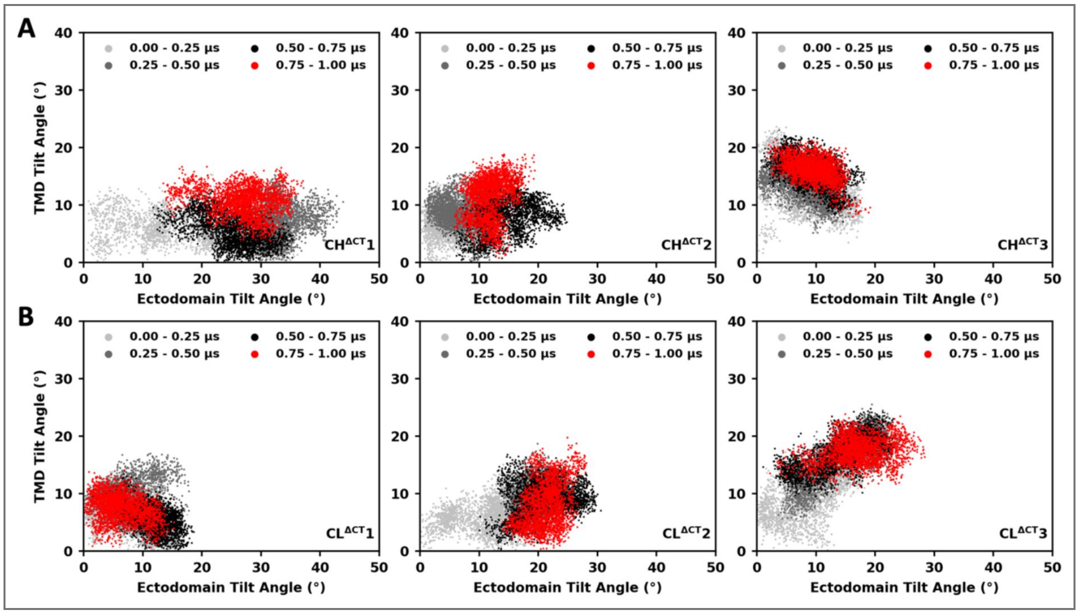

Figure 2—figure supplement 1. Ectodomain tilt versus TMD tilt, grouped by time intervals (cleaved CT-truncated systems). (**A**) Three trajectories starting from the “high” TMD configuration. (**B**) Three trajectories starting from the “low” TMD configuration. The 1-μs trajectory was divided into four intervals, with values from each interval shown in light gray, dark gray, black, and red, respectively.

Figure 2—figure supplement 2. Ectodomain tilt versus TMD tilt, grouped by time intervals (uncleaved CT-truncated systems).

Labeling and color coding are the same as in Figure 2—figure supplement 1.

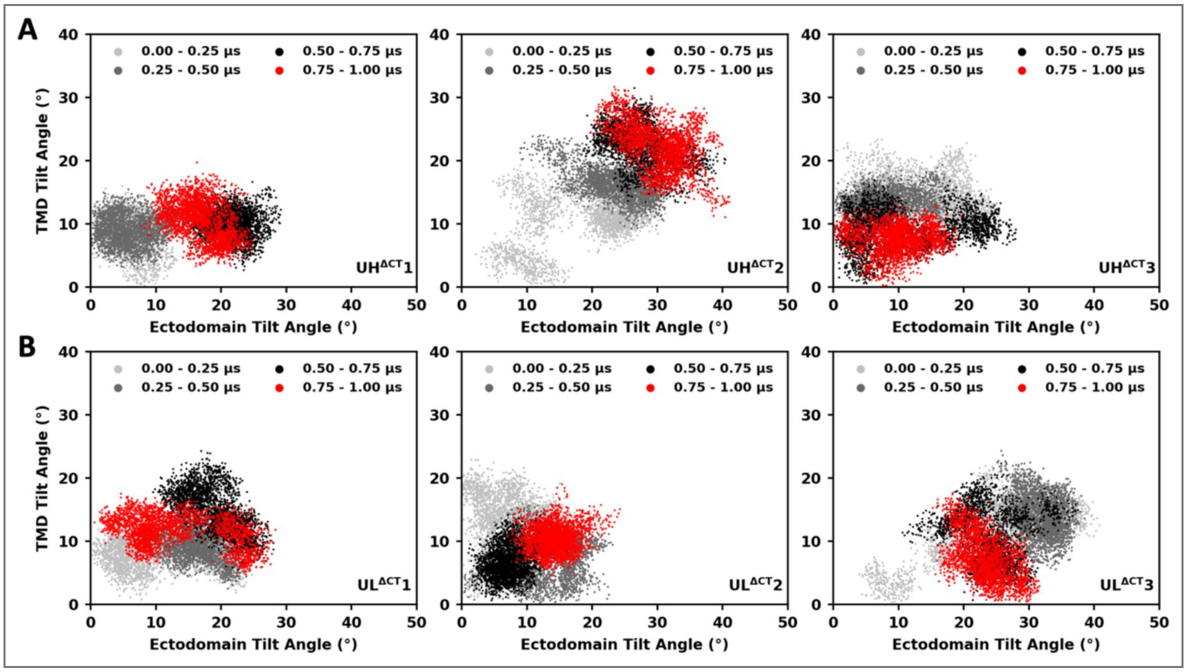

Figure 2—figure supplement 3. Ectodomain tilt versus TMD tilt, grouped by time intervals (cleaved full-length systems).

Labeling and color coding are the same as in Figure 2—figure supplement 1.

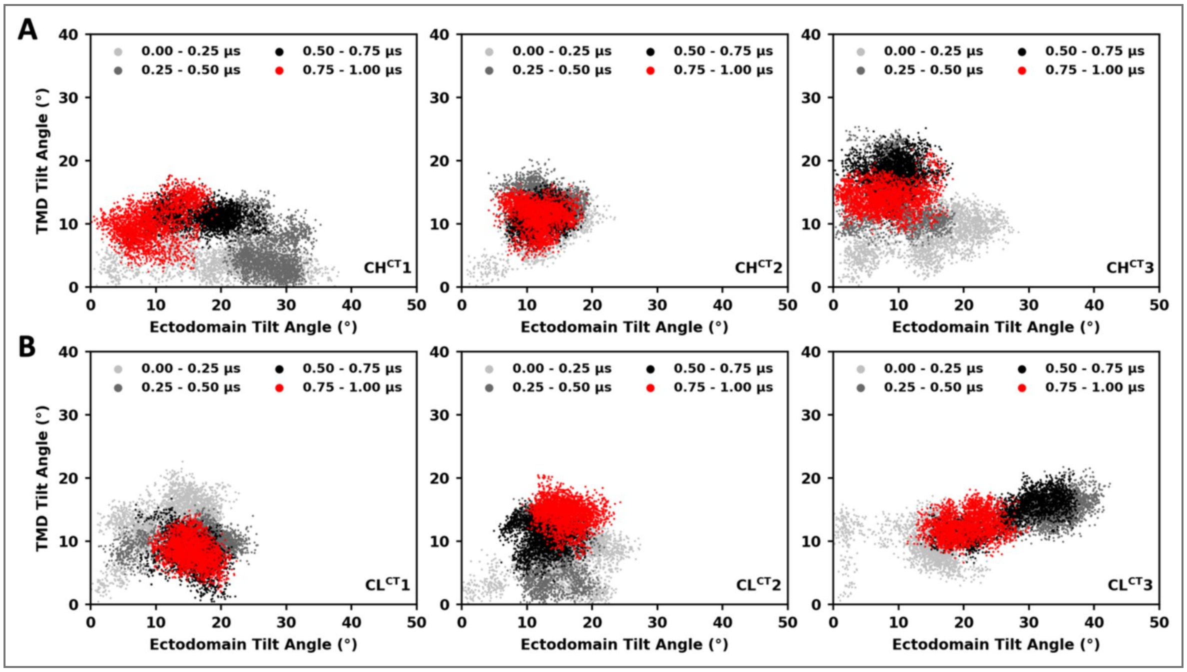

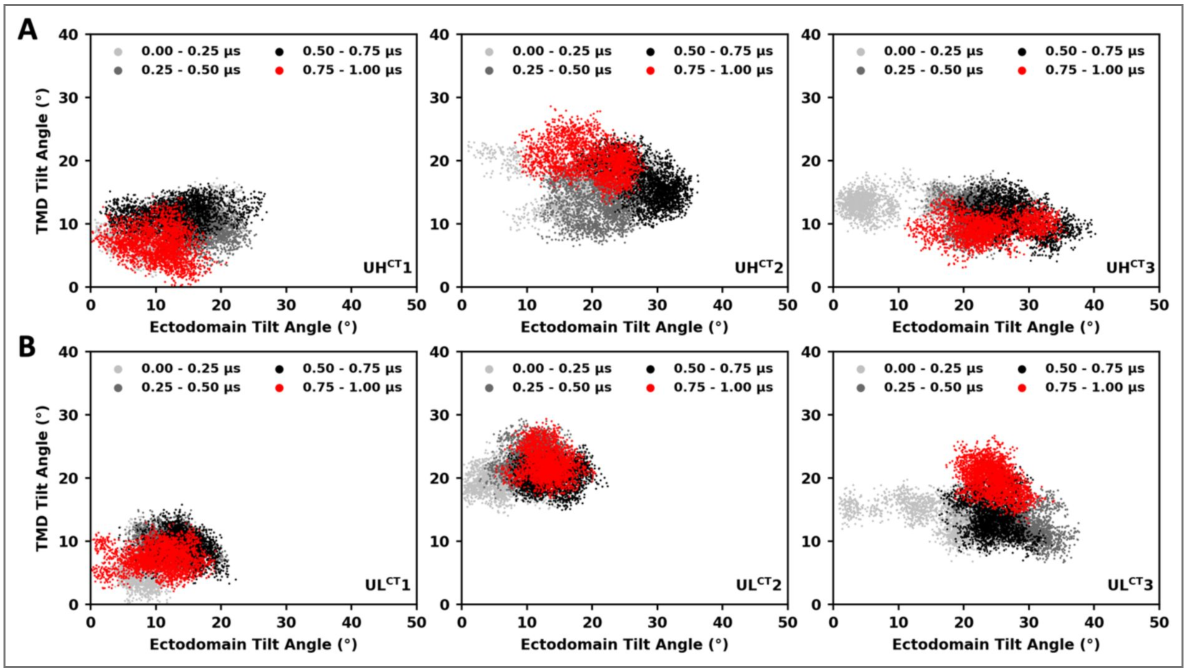

Figure 2—figure supplement 4. **Ectodomain tilt versus TMD tilt, grouped by time intervals (uncleaved full-length systems).**

Labeling and color coding are the same as in Figure 2—figure supplement 1.

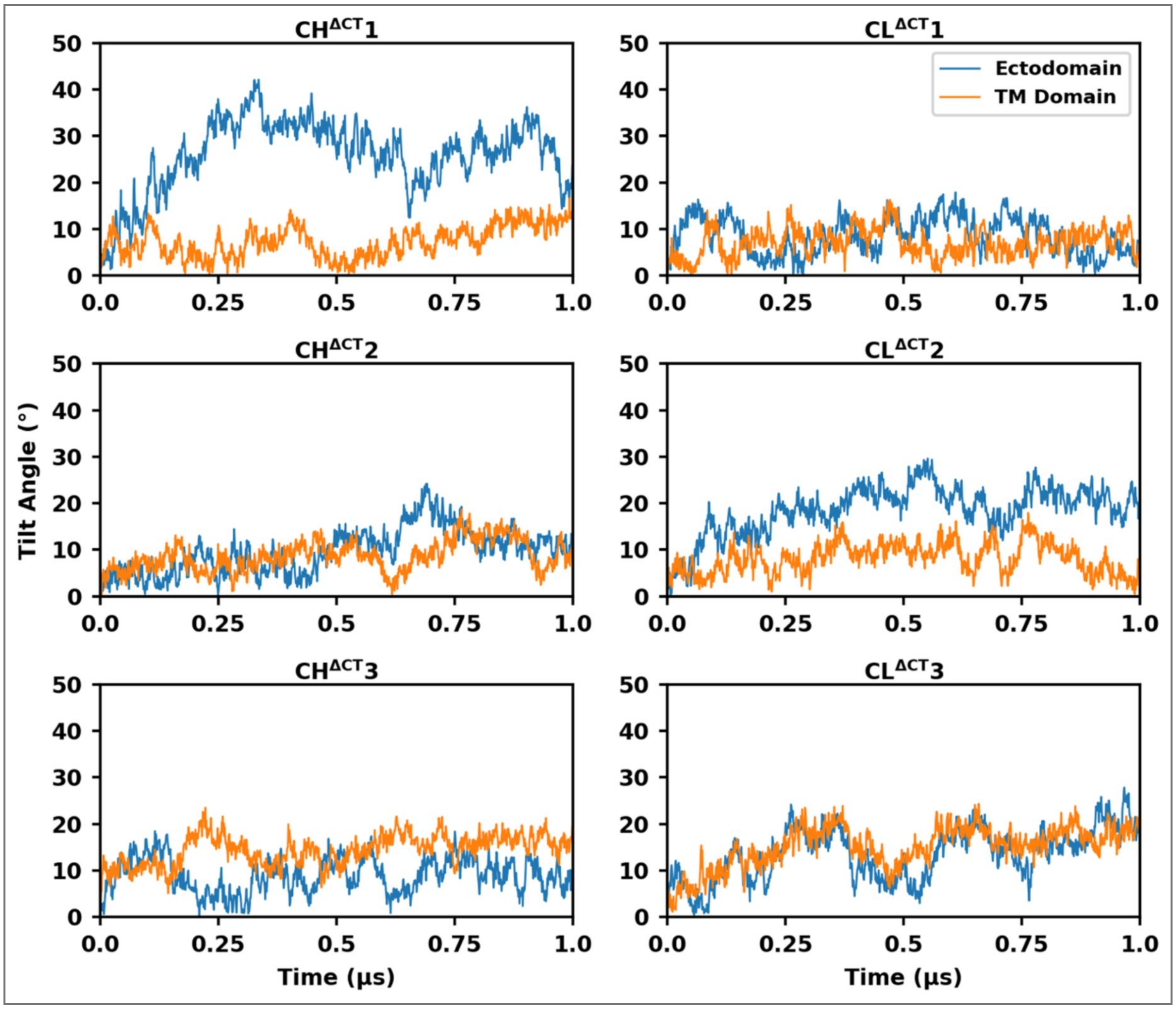

Figure 2—figure supplement 5. **Temporal evolution of Ectodomain and TMD tilt angles (cleaved CT-truncated systems).**

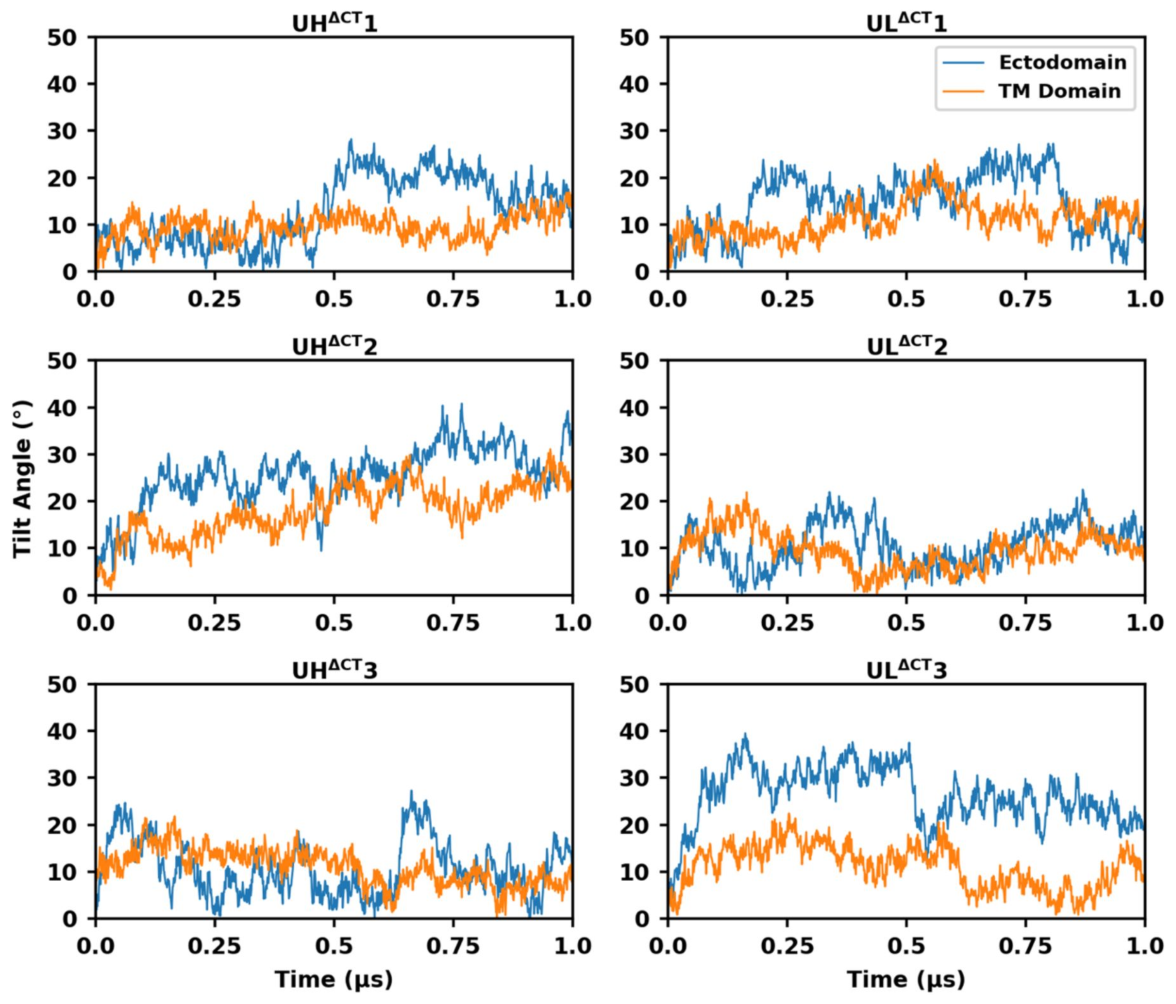

Figure 2—figure supplement 6. Temporal evolution of Ectodomain and TMD tilt angles (uncleaved CT-truncated systems).

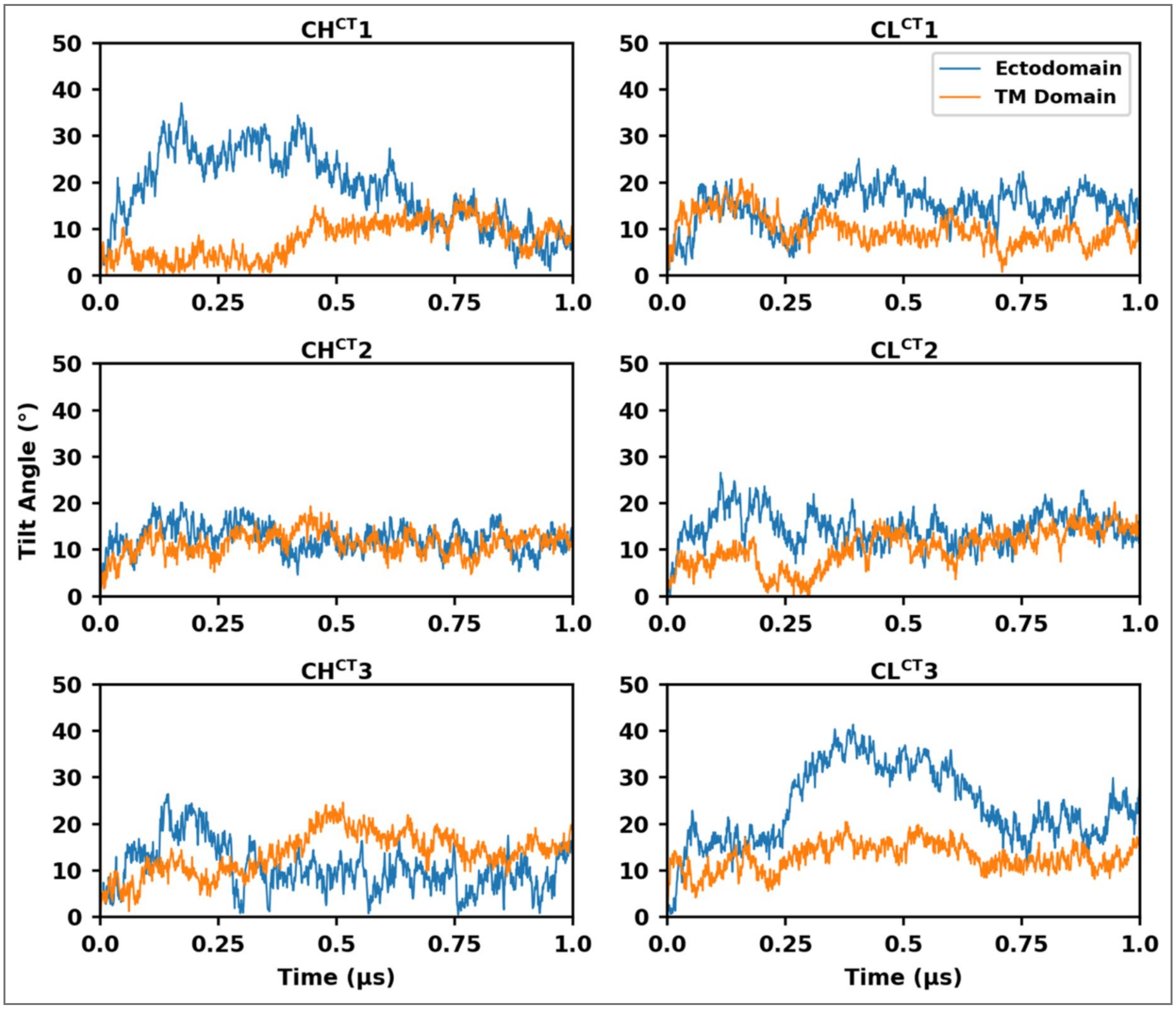

Figure 2—figure supplement 7. **Temporal evolution of Ectodomain and TMD tilt angles (cleaved full-length systems).**

Figure 2—figure supplement 8. Temporal evolution of Ectodomain and TMD tilt angles (uncleaved full-length systems).

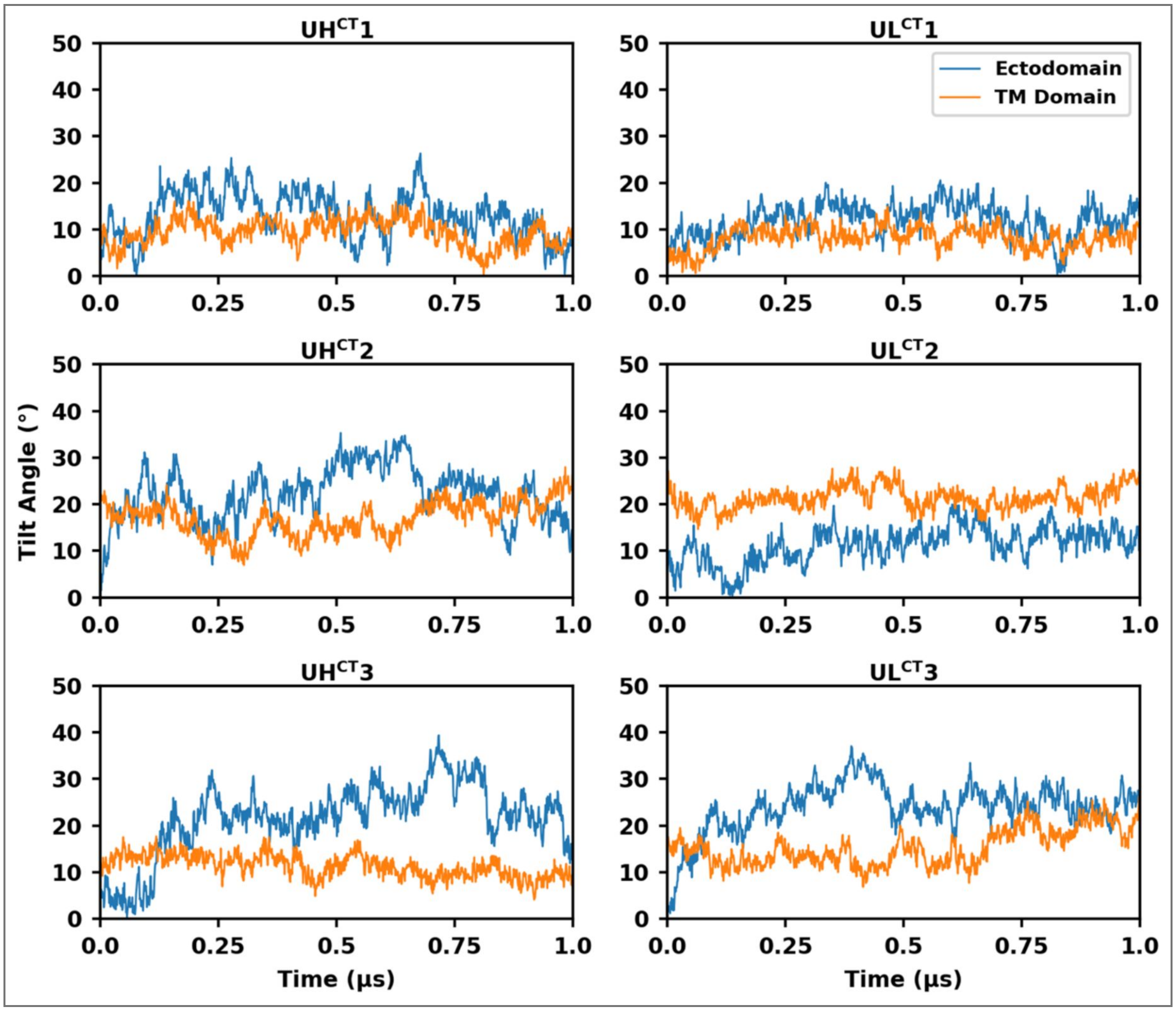

Figure 2—figure supplement 9. Probability densities of ectodomain and TMD tilt angles (full-length systems).

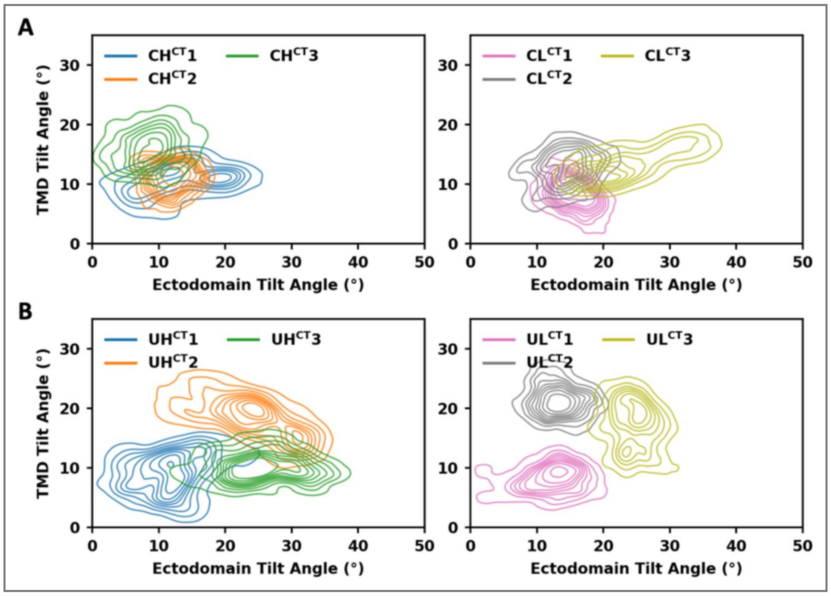

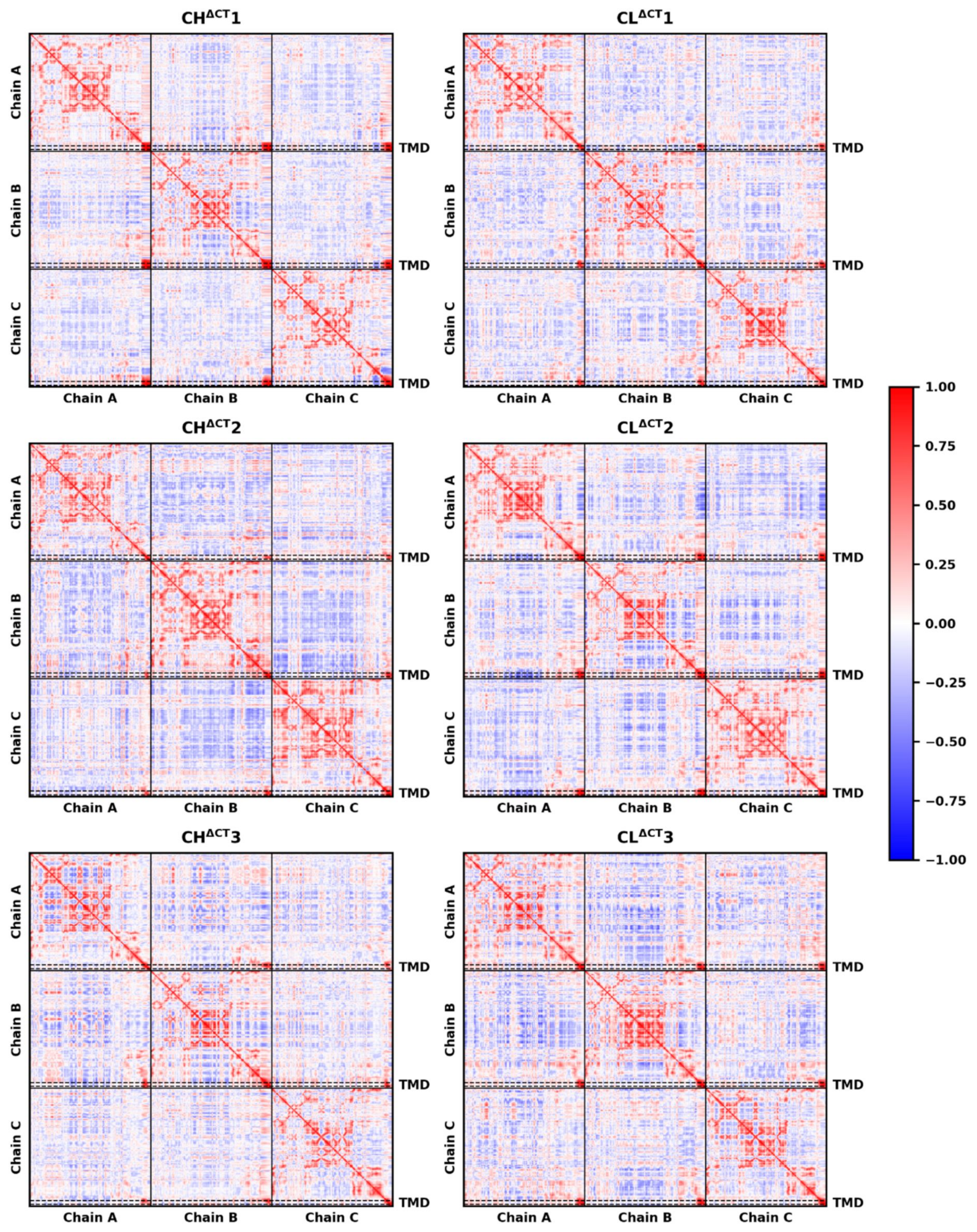

Figure 2—figure supplement 10. **Dynamic cross-correlation matrix of Cα atoms (cleaved CT-truncated systems).**

The x-axis (left to right) and the y-axis (top to bottom) correspond to residue indices ranging from 31 to 716 for each of the three protomers, where residues 31-664 compose the ectodomain. The TMD (residues 684-705) is indicated by dashed boxes. Corelated and anti-correlated motions are color-coded from red to blue, respectively.

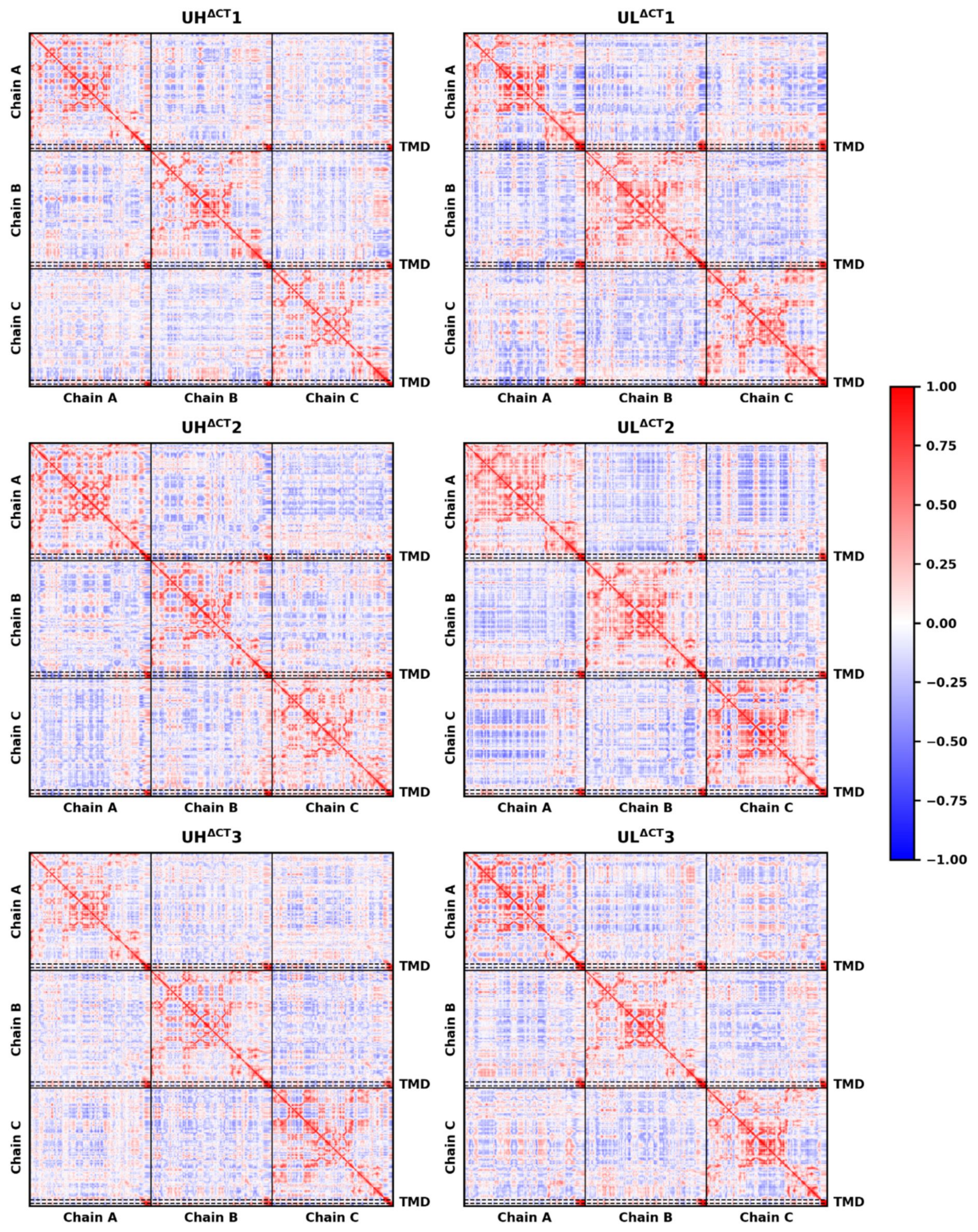

Figure 2—figure supplement 11. Dynamic cross-correlation matrix of Cα atoms (uncleaved CT-truncated systems).

The x-axis (left to right) and the y-axis (top to bottom) correspond to residue indices ranging from 31 to 716 for each of the three protomers, where residues 31-664 compose the ectodomain. The TMD (residues 684-705) is indicated by dashed boxes. Corelated and anti-correlated motions are color-coded from red to blue, respectively.

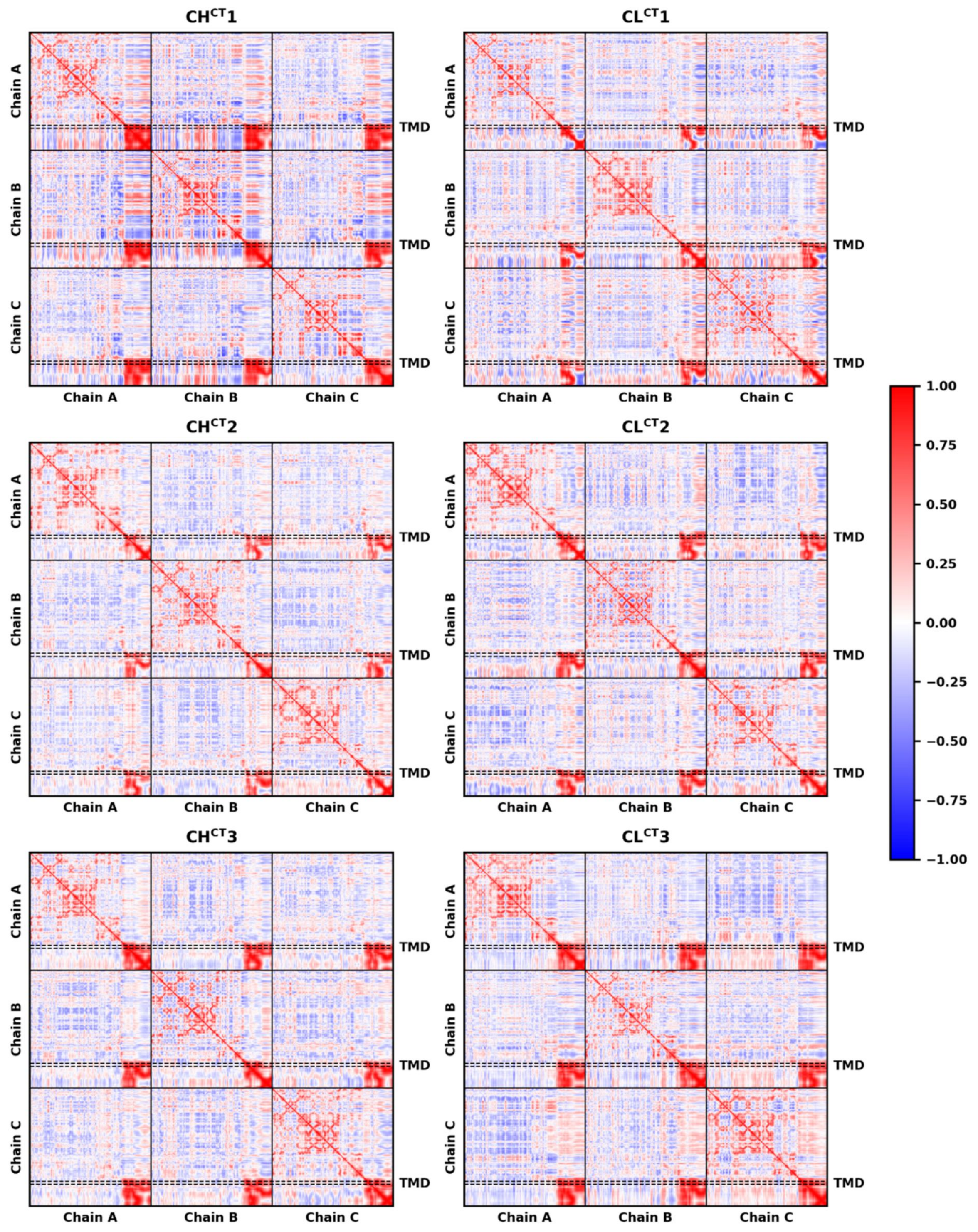

Figure 2—figure supplement 12. **Dynamic cross-correlation matrix of Cα atoms (cleaved full-length systems).**

The x-axis (left to right) and the y-axis (top to bottom) correspond to residue indices ranging from 31 to 716 for each of the three protomers. Residues 31-856 compose the ectodomain, and residues 706-856 compose the CT. The TMD (residues 684-705) is indicated by dashed boxes. Corelated and anti-correlated motions are color-coded from red to blue, respectively.

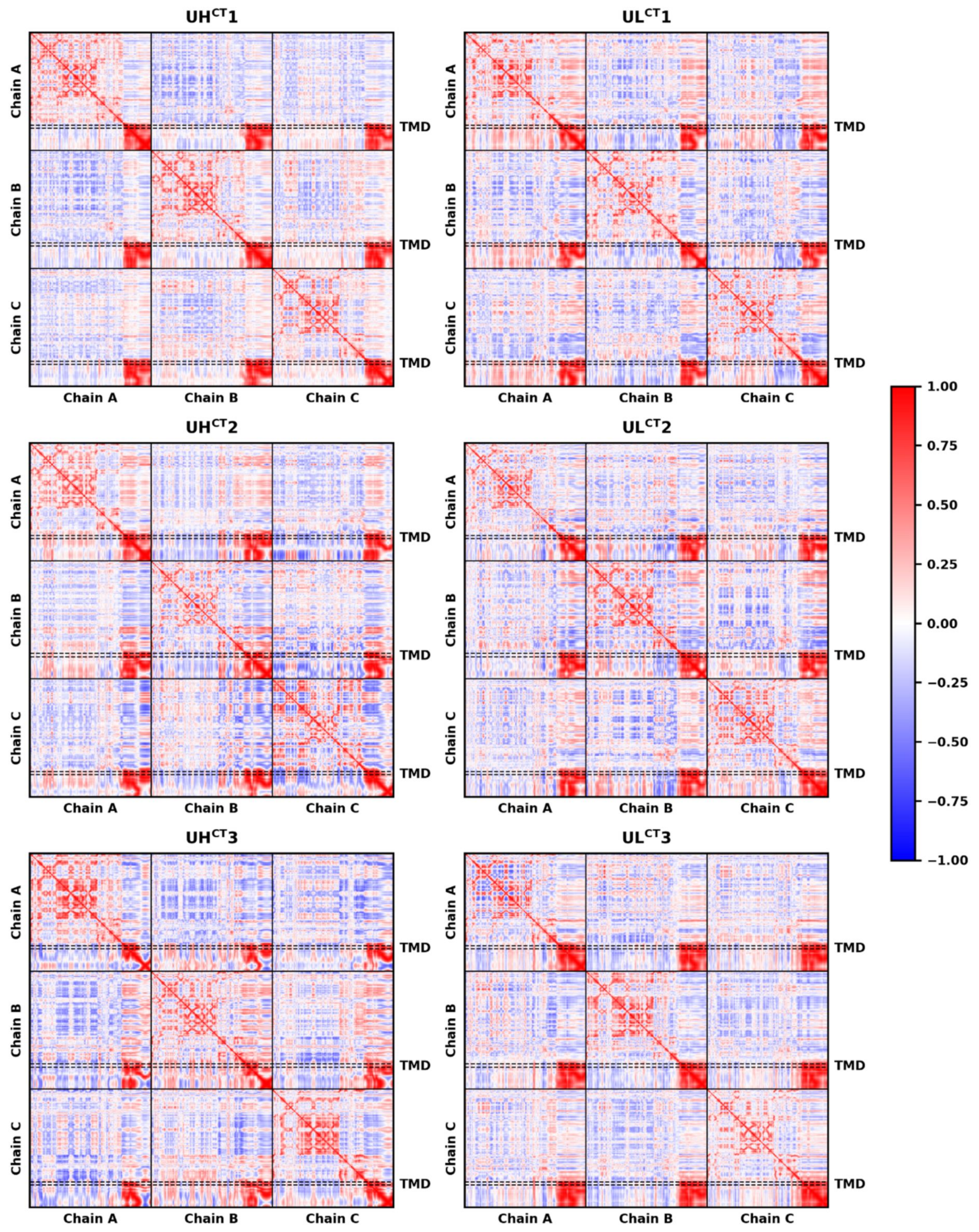

Figure 2—figure supplement 13. **Dynamic cross-correlation matrix of Cα atoms (uncleaved full-length systems).**

The x-axis (left to right) and the y-axis (top to bottom) correspond to residue indices ranging from 31 to 716 for each of the three protomers. Residues 31-856 compose the ectodomain, and residues 706-856 compose the CT. The TMD (residues 684-705) is indicated by dashed boxes. Corelated and anti-correlated motions are color-coded from red to blue, respectively.

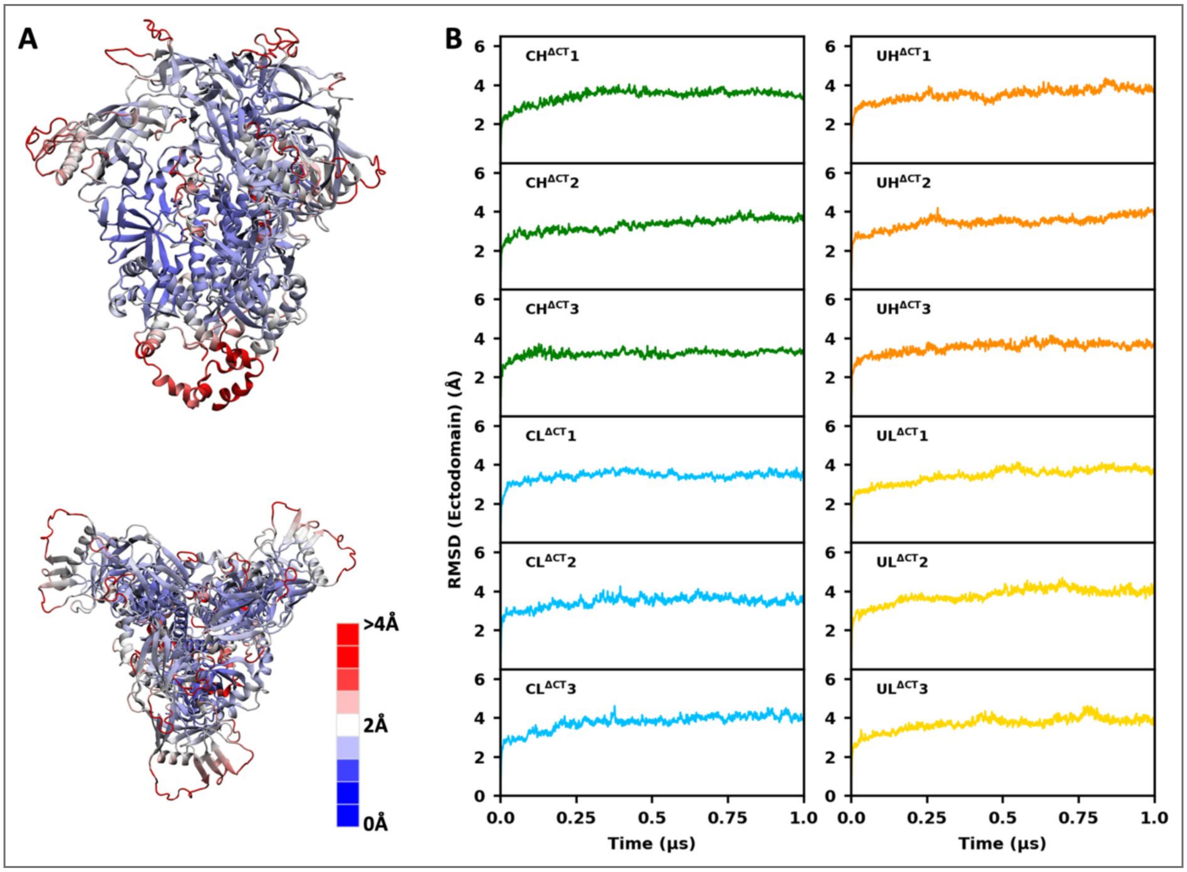

Figure 3—figure supplement 1. RMSF and RMSD of the ectodomain.

(**A**) Top and side views of the ectodomain and MPER in the uncleaved system, with RMSF indicated by color. (**B**) RMSD relative to the initial model as a function of time, calculated from the trajectories of CT-truncated systems.

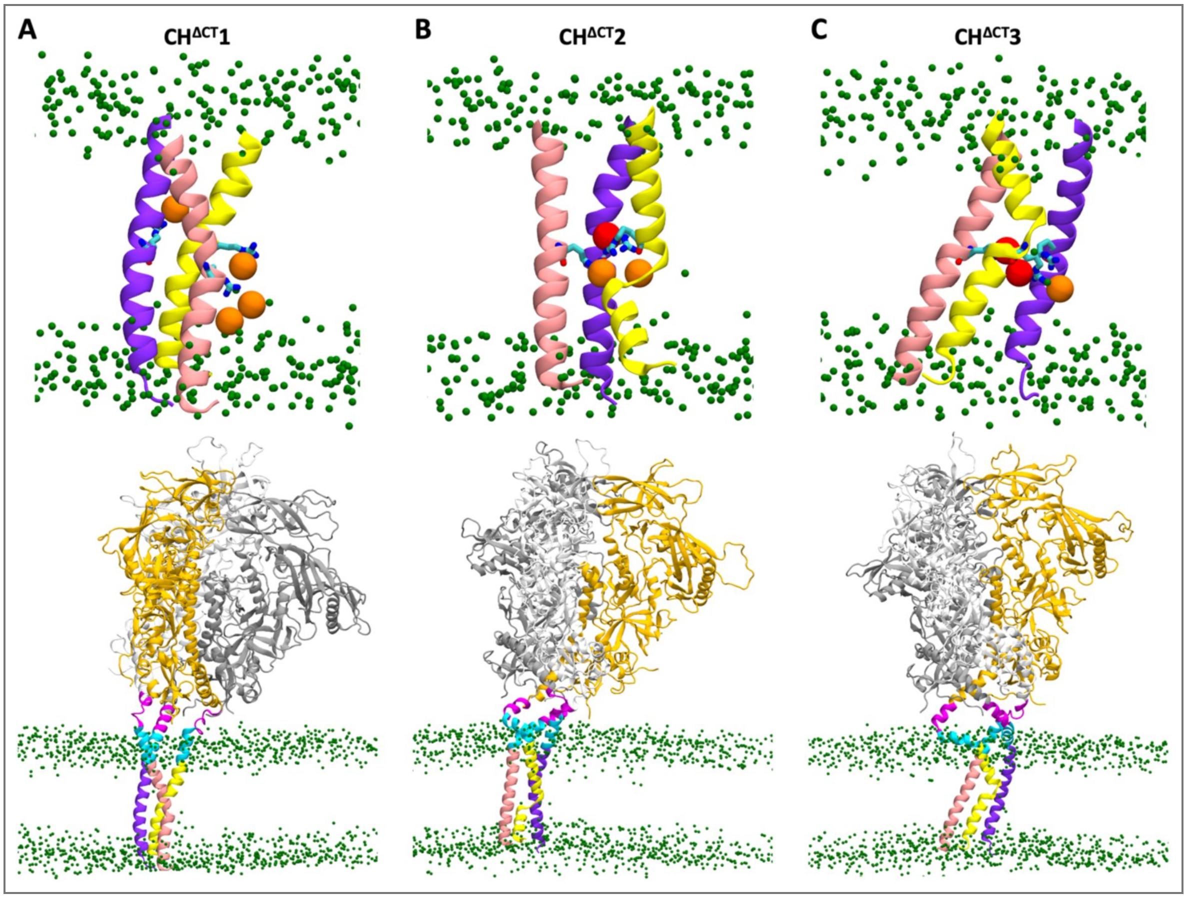

Figure 4—figure supplement 1. **Local conformations of the TMD and global conformations of protein and membrane ($CH^{\Delta CT}$ systems).**

Three protomers of the TMD are shown in light yellow, purple, and pink; three protomers of the ectodomain in dark yellow, gray, and white; MPER-N and MPER-C in magenta and cyan, respectively; and lipid headgroups in green. Lipid headgroups interacting with R696 are highlighted in orange, and the ions interacting with R696 in red.

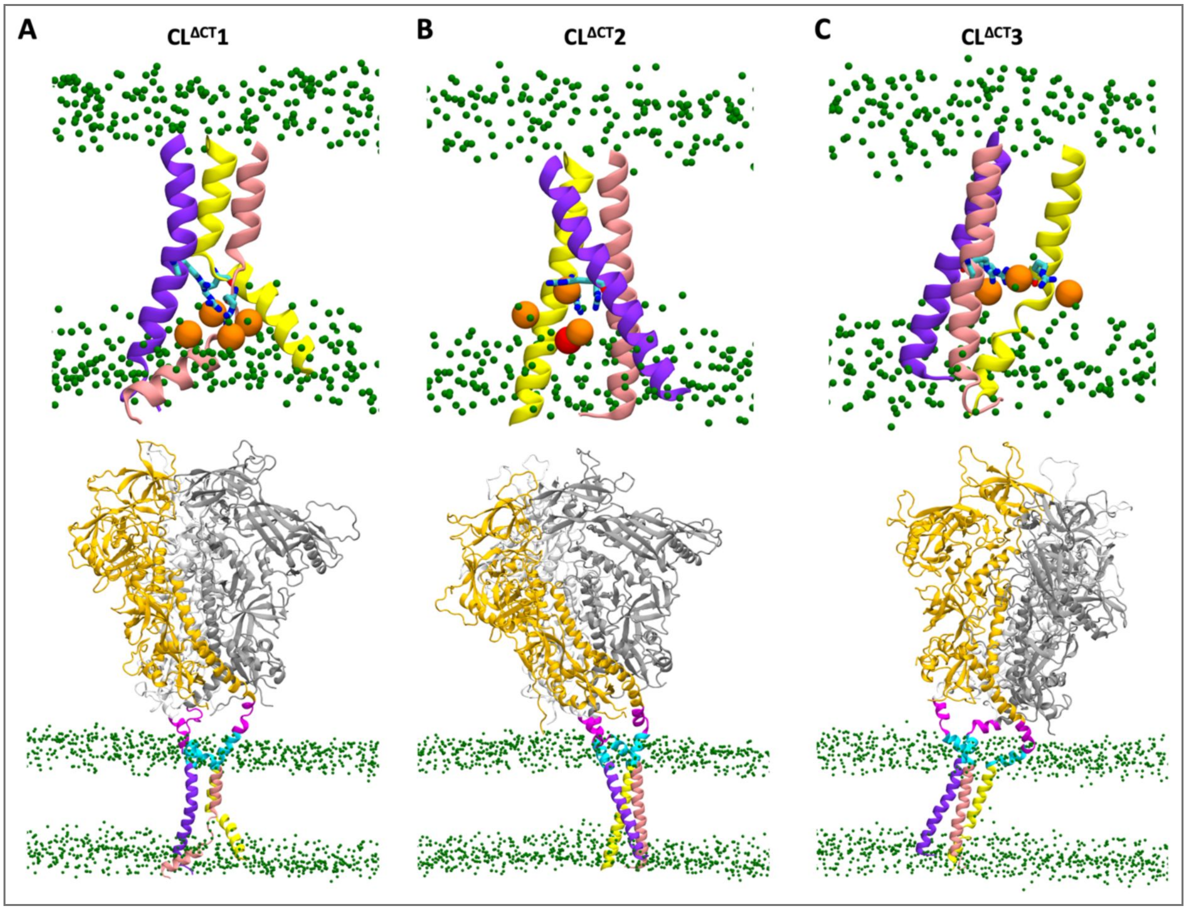

Figure 4—figure supplement 2. Local conformations of the TMD and global conformations of protein and membrane ($CL^{\Delta CT}$ systems).

Labeling and color coding are the same as in Figure 4—figure supplement 1.

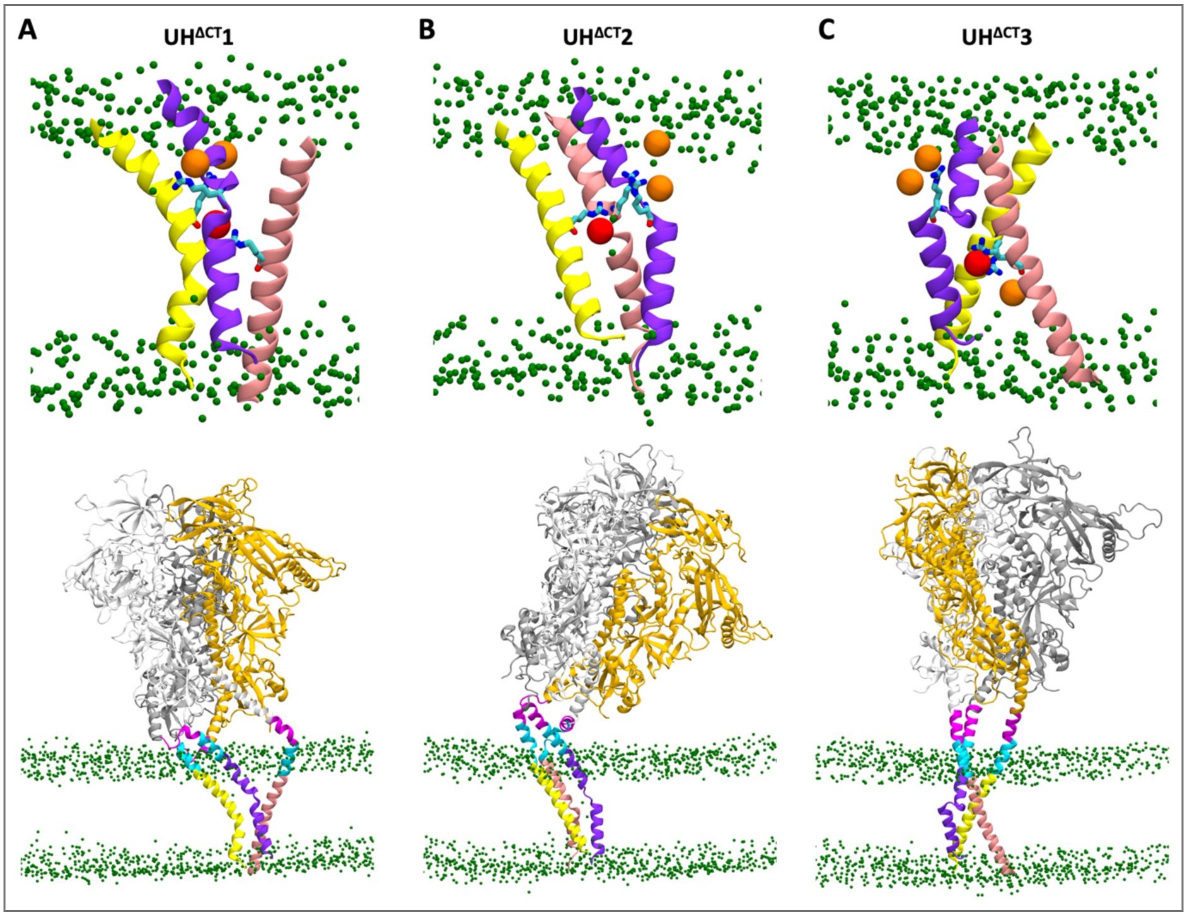

Figure 4—figure supplement 3. **Local conformations of the TMD and global conformations of protein and membrane ($UH^{\Delta CT}$ systems).**

Labeling and color coding are the same as in Figure 4—figure supplement 1.

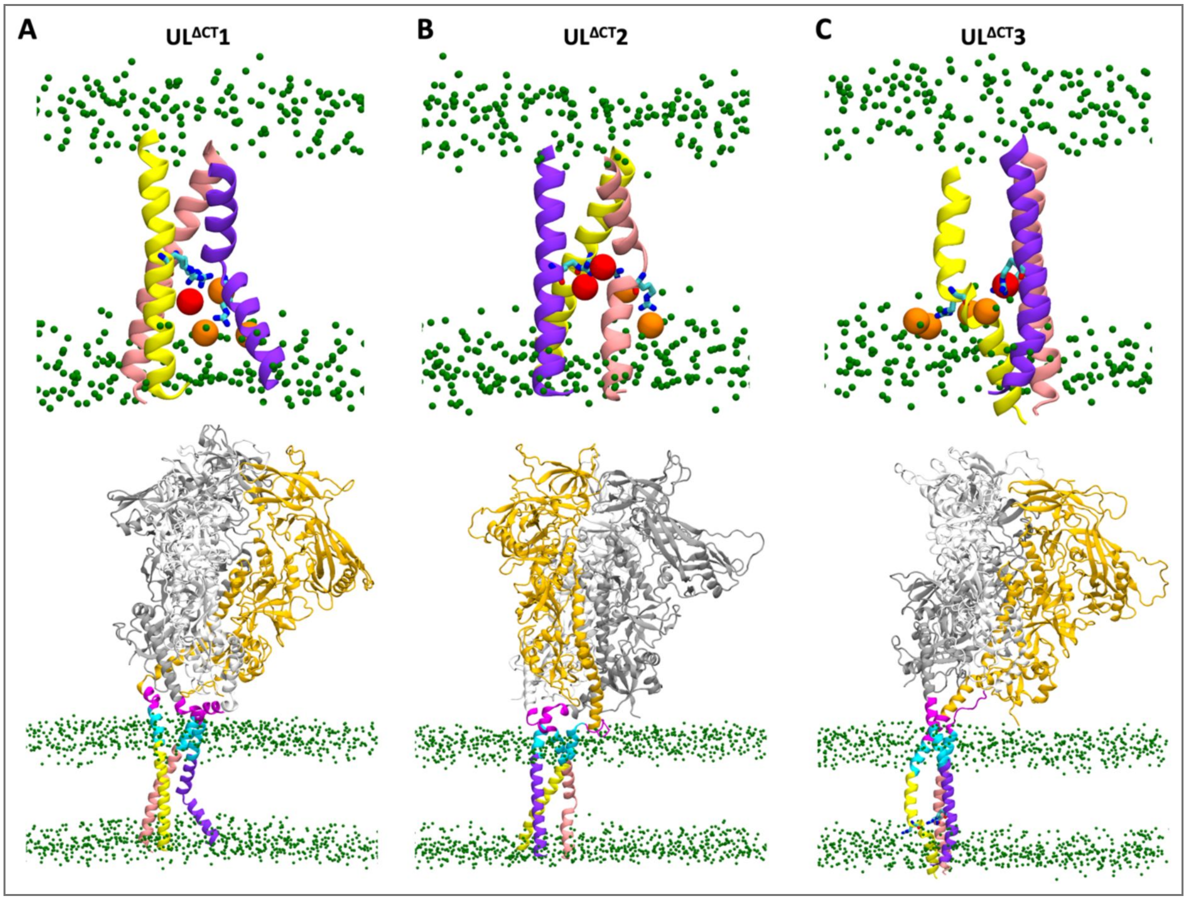

Figure 4—figure supplement 4. **Local conformations of the TMD and global conformations of protein and membrane ($UL^{\Delta CT}$ systems).**

Labeling and color coding are the same as in Figure 4—figure supplement 1.

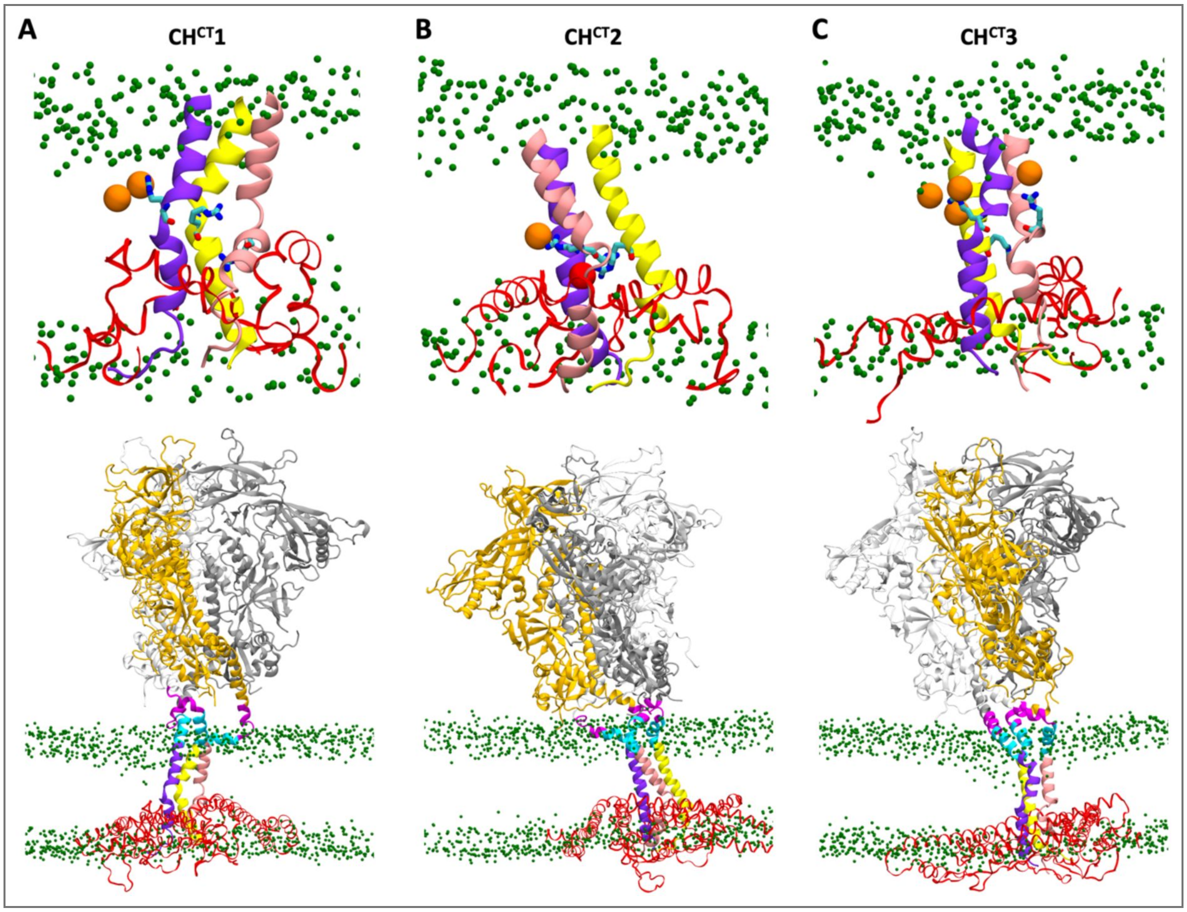

Figure 4—figure supplement 5. Local conformations of the TMD and global conformations of protein and membrane (CH^{CT} systems).

Labeling and color coding are the same as in Figure 4—figure supplement 1, with the CT additionally shown in red.

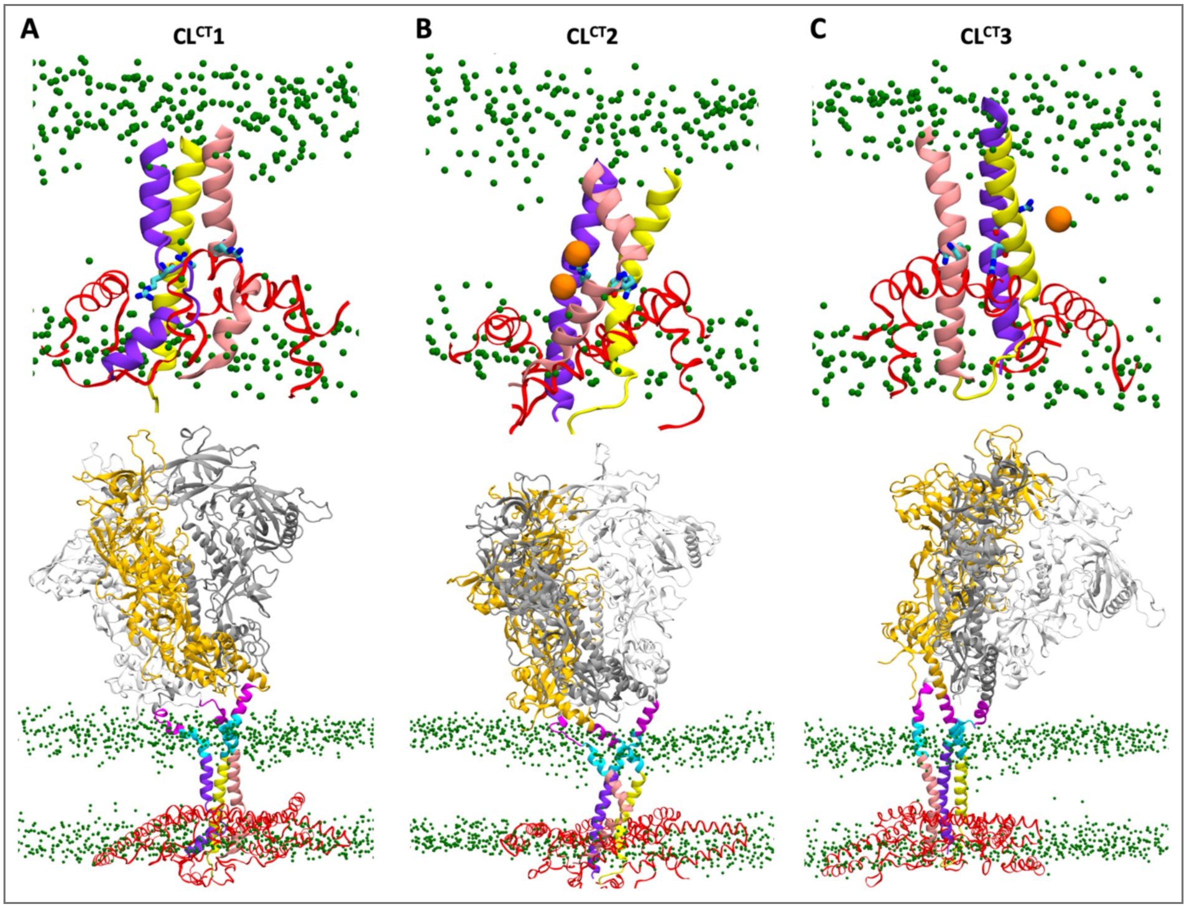

Figure 4—figure supplement 6. **Local conformation of the TMD and global conformation of protein and membrane (CL^{CT} systems).**

Labeling and color coding are the same as in Figure 4—figure supplement 5.

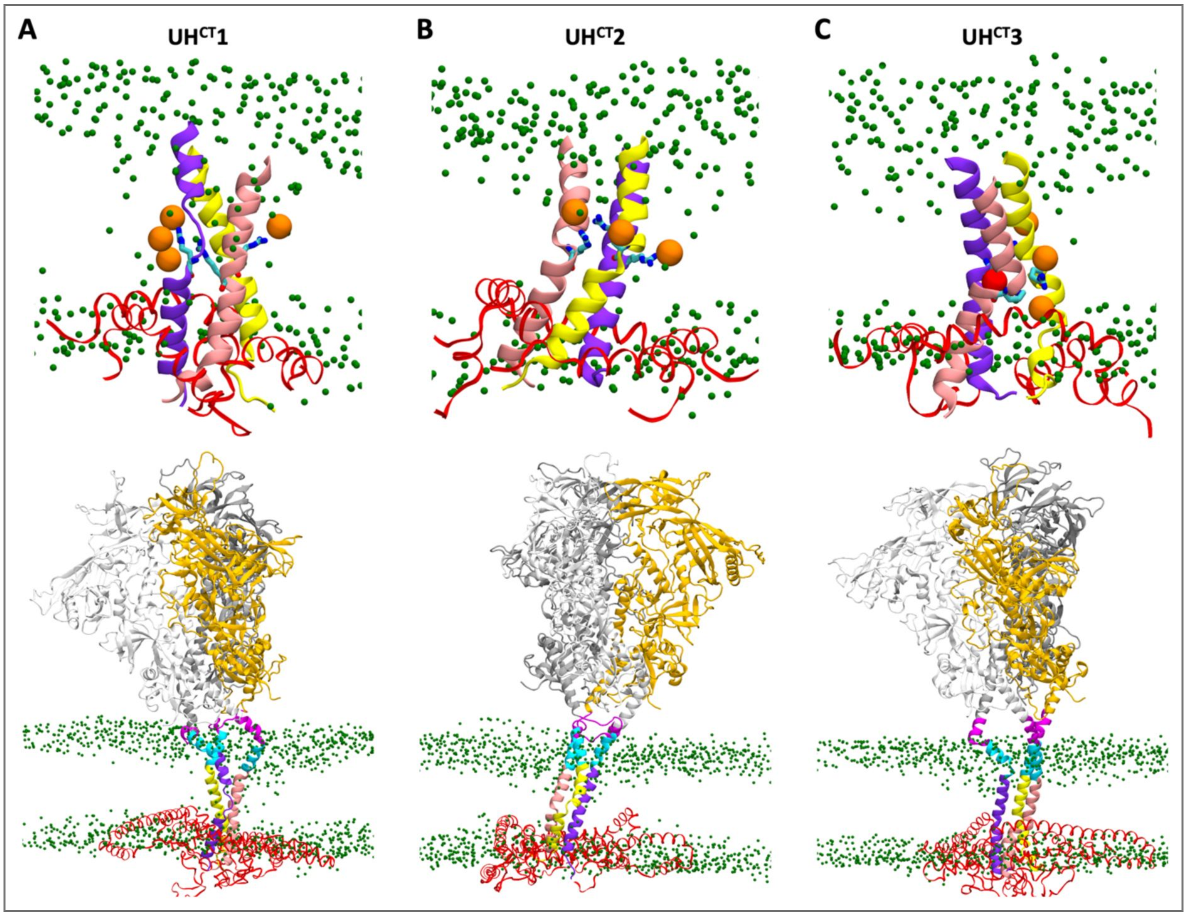

Figure 4—figure supplement 7. **Local conformations of the TMD and global conformations of protein and membrane (UH^{CT} systems).**

Labeling and color coding are the same as in Figure 4—figure supplement 5.

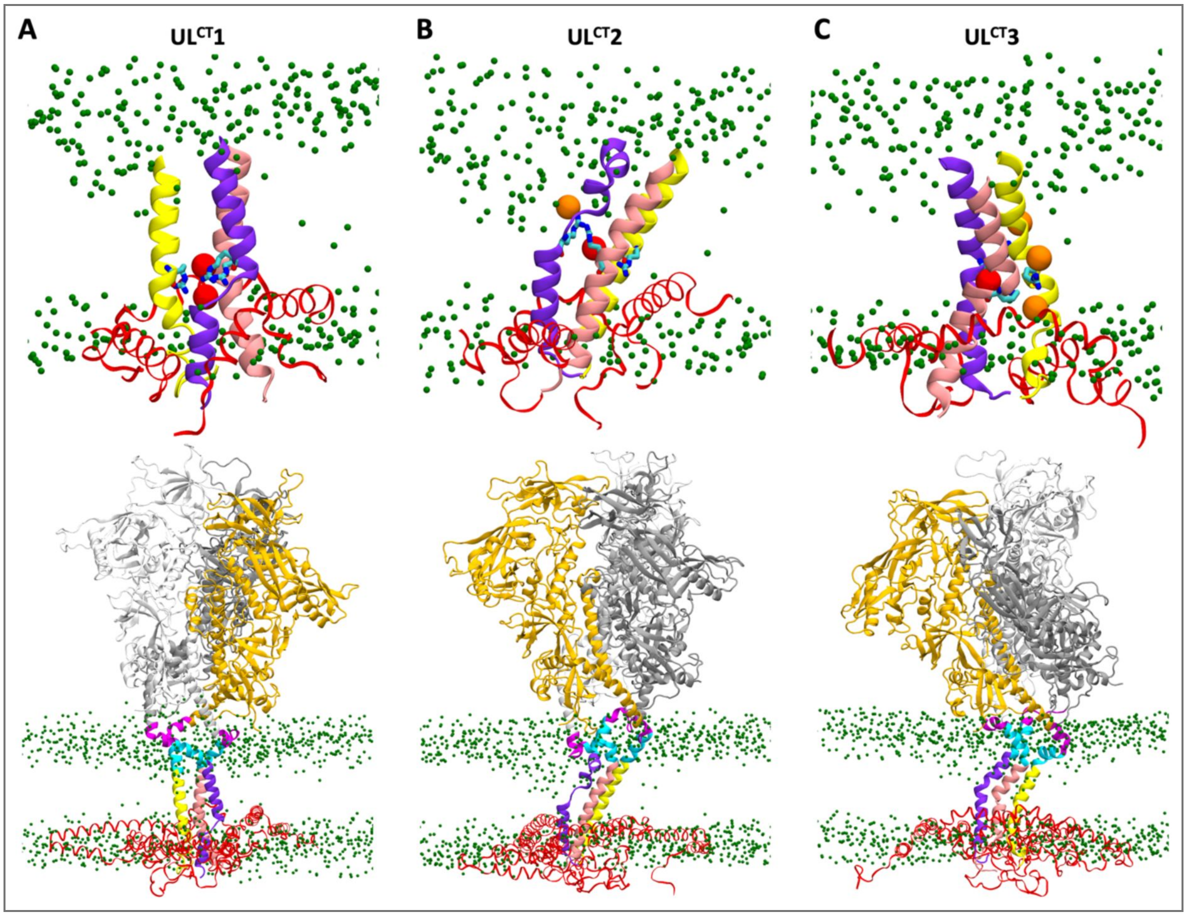

Figure 4—figure supplement 8. **Local conformations of the TMD and global conformations of protein and membrane (UL^{CT} systems).**

Labeling and color coding are the same as in Figure 4—figure supplement 5.

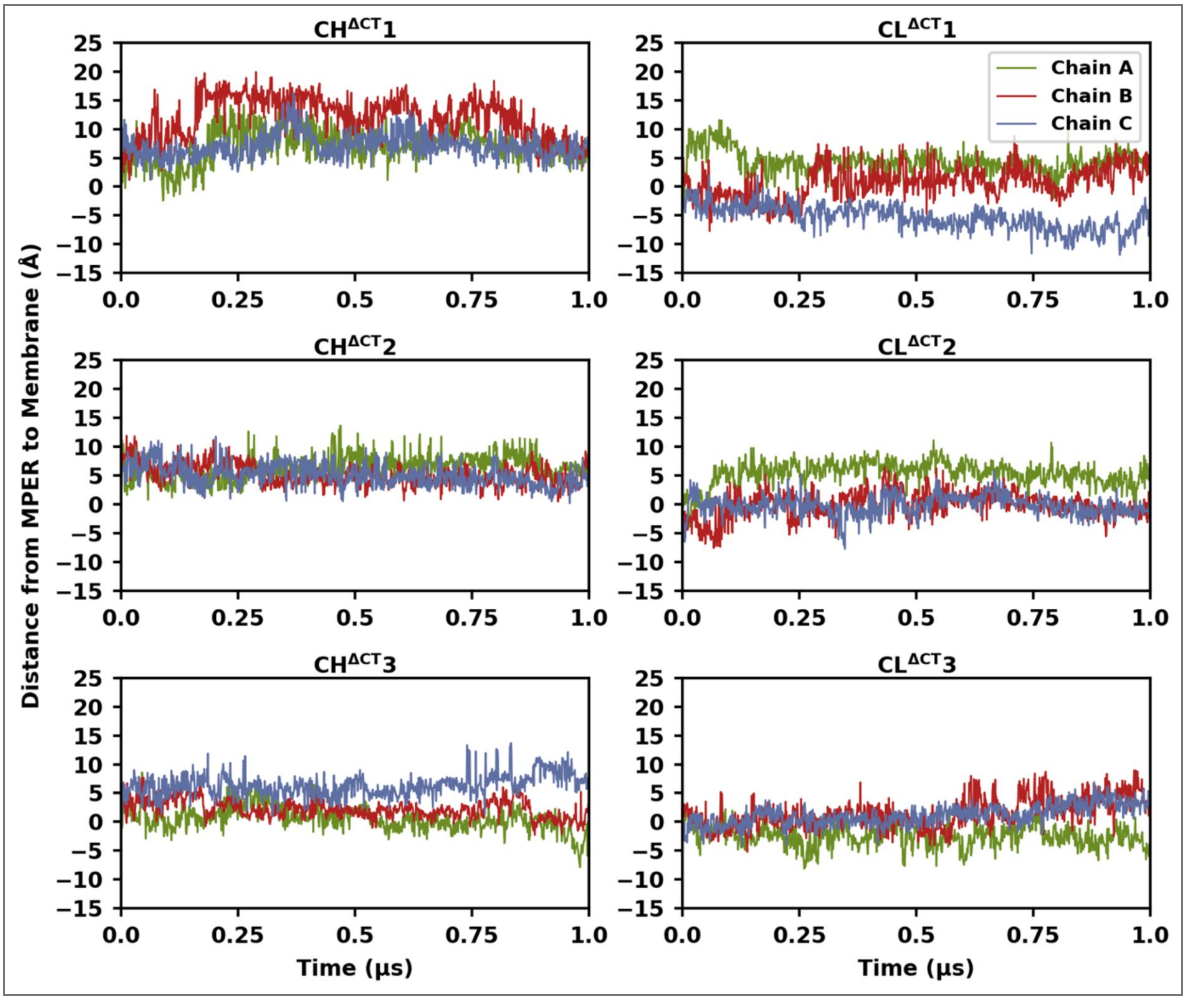

Figure 5—figure supplement 1. **Temporal evolution of the distance from the MPER midpoint to the membrane surface.**

The distance d_{F673}, defined in Figure 5A, is shown as a function of simulation time for the $CH^{\Delta CT}$ and $CL^{\Delta CT}$ systems.

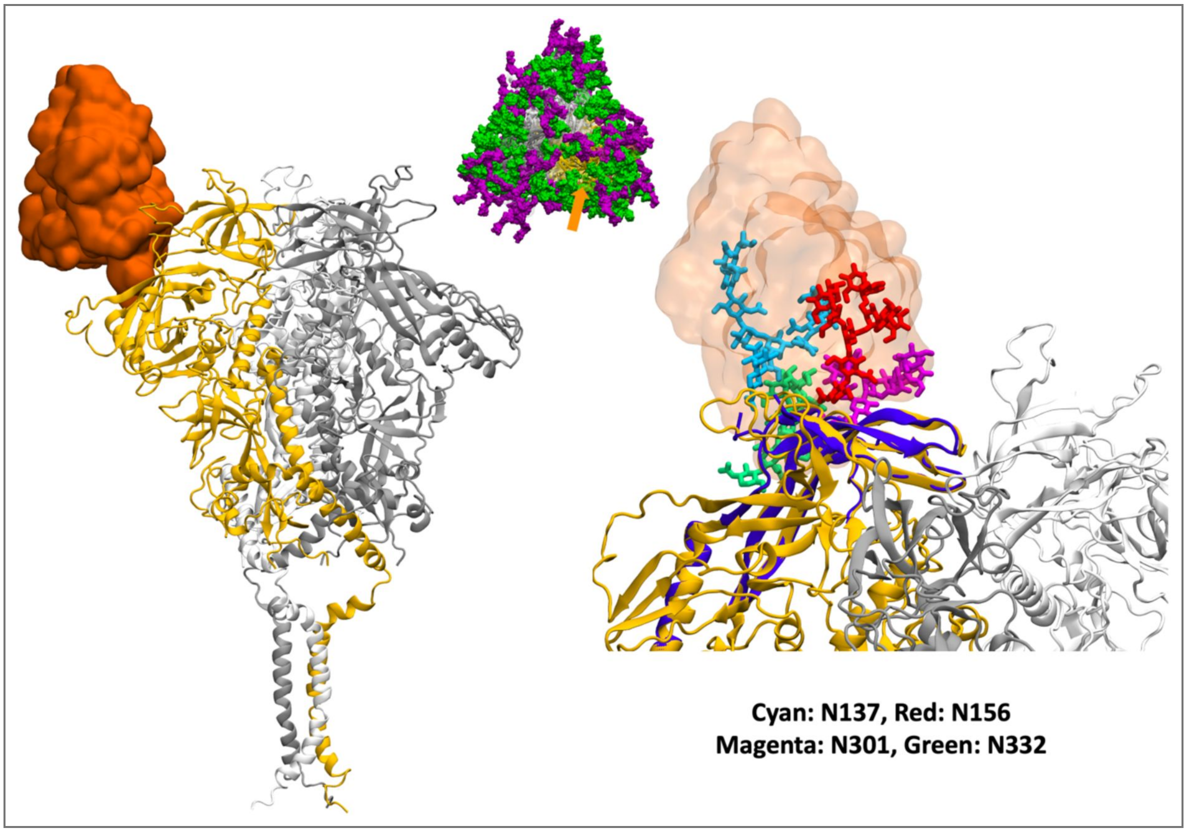

Figure 6—figure supplement 1. **Shielding of antibody PGT128 epitope.**

(**Left**) Variable domains of the heavy and light chains aligned onto our modeled structure. (**Middle**) Top view of the glycosylated trimeric protein, with the orange arrow indicating the epitope location. (**Right**) Part of the epitope in the antibody-epitope complex PDB structure was used for structural alignment and is highlighted in purple. Glycans capable of hindering antibody binding are shown in various colors.

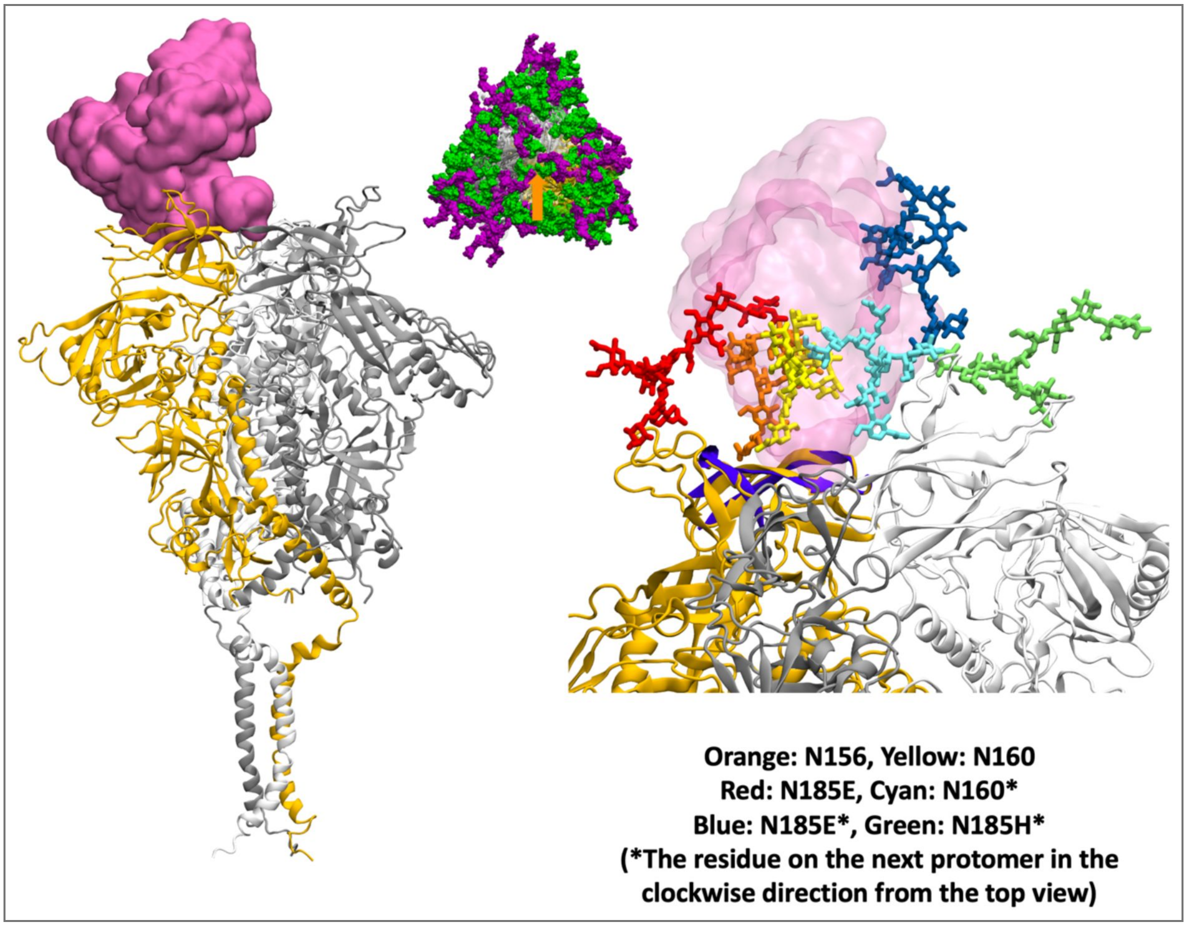

Figure 6—figure supplement 2. **Shielding of antibody PG9 epitope.**

Labeling and color coding are the same as in Figure 6—figure supplement 1.

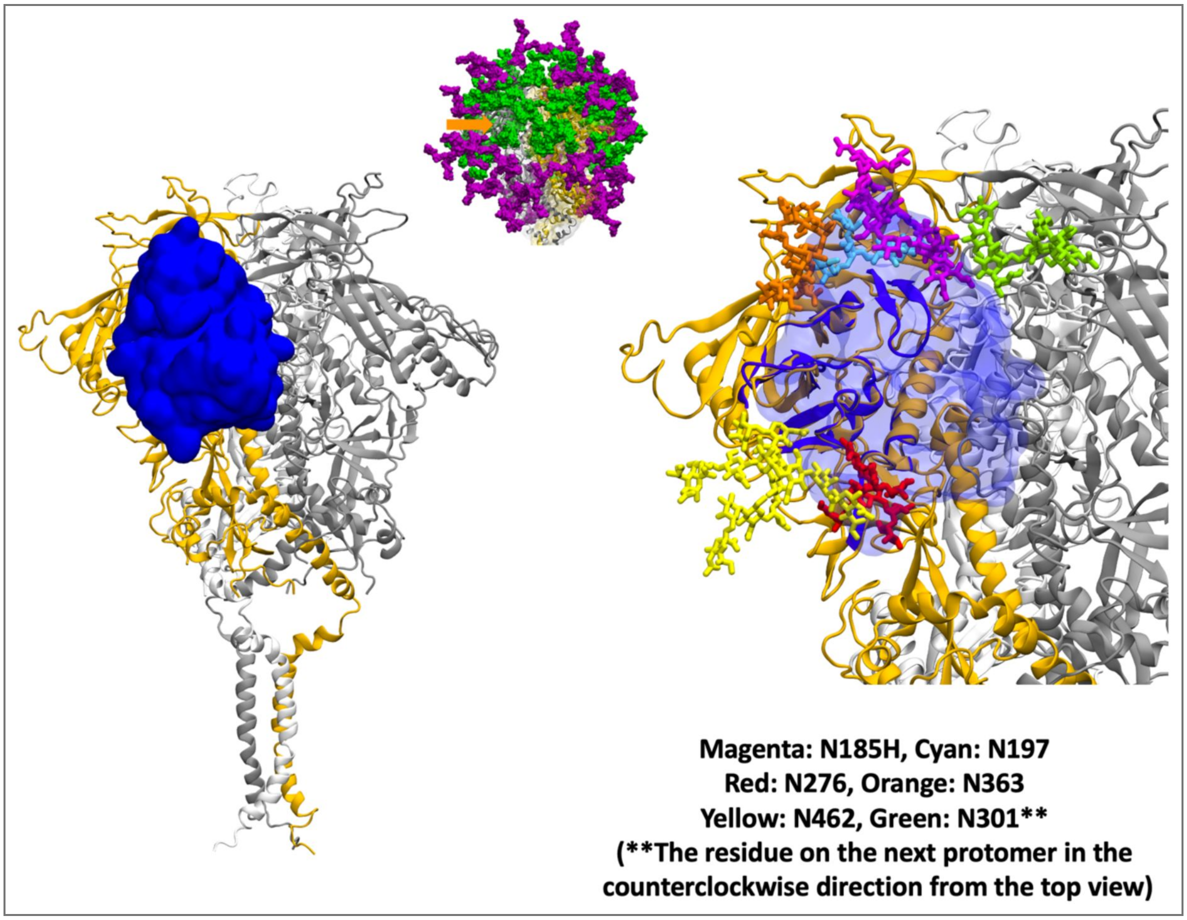

Figure 6—figure supplement 3. **Shielding of antibody VRC01 epitope.**

Labeling and color coding are the same as in Figure 6—figure supplement 1. (**Middle**) The glycosylated trimeric protein is shown in a side view instead of the top view.

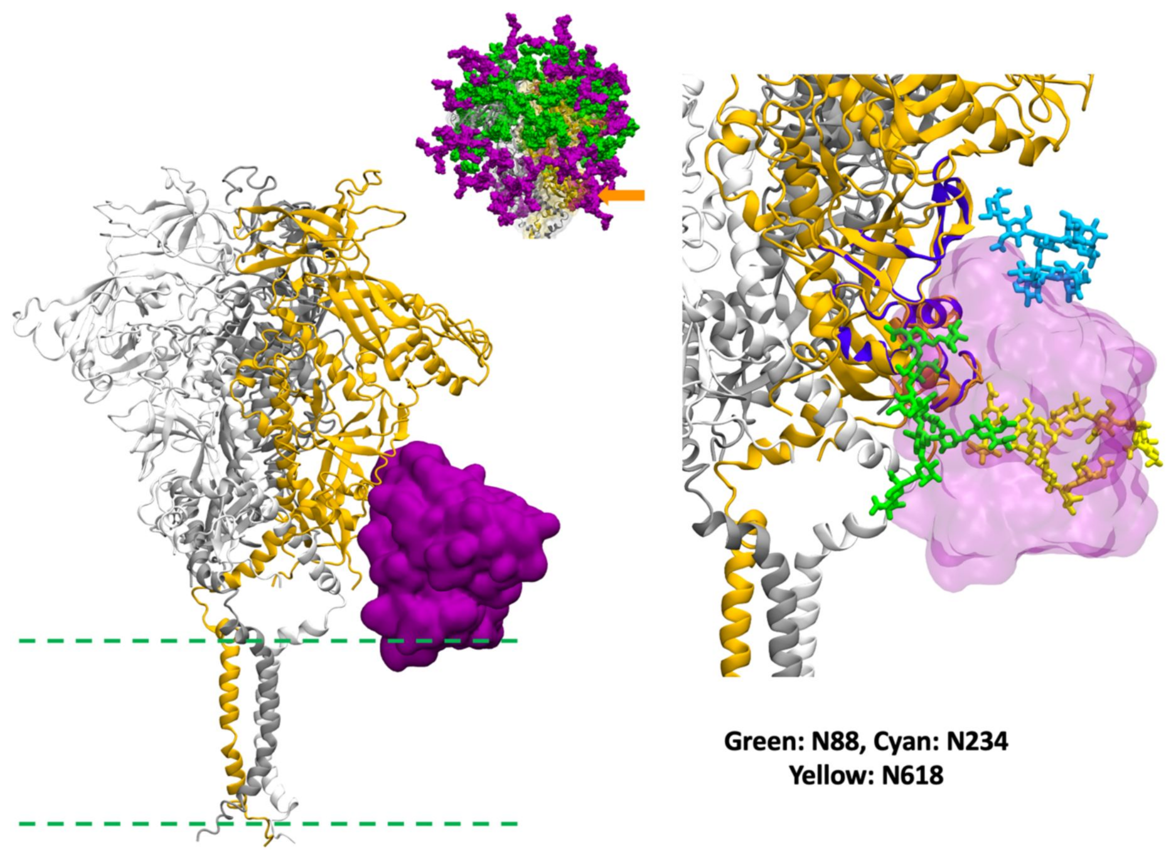

Figure 6—figure supplement 4. **Shielding of antibody 35O22 epitope.**

Labeling and color coding are the same as in Figure 6—figure supplement 3. (**Left**) The dashed greens indicate the approximate location of the lipid headgroups.

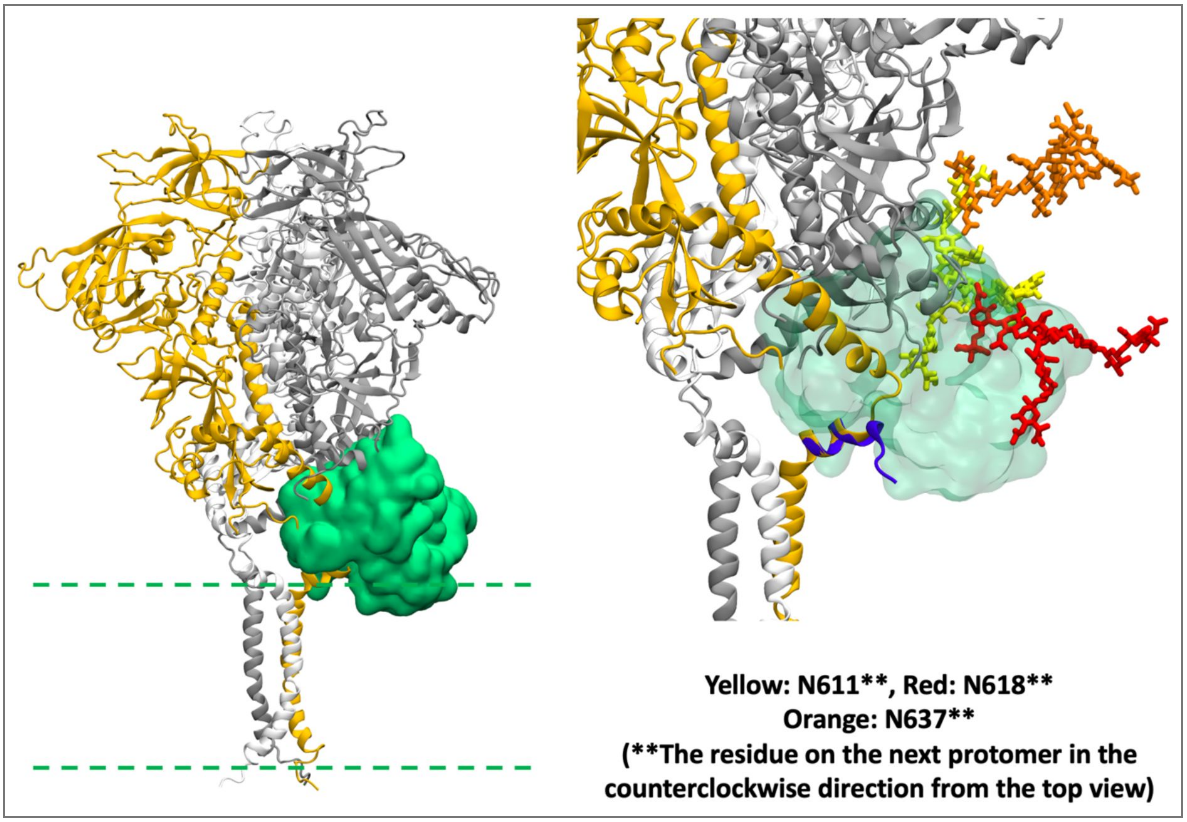

Figure 6—figure supplement 5. **Shielding of antibody 4E10 epitope.**

Labeling and color coding are the same as in Figure 6—figure supplement 4.

Figure 6—figure supplement 6. Shielding of antibody 10E8 epitope.

Labeling and color coding are the same as in Figure 6—figure supplement 4.

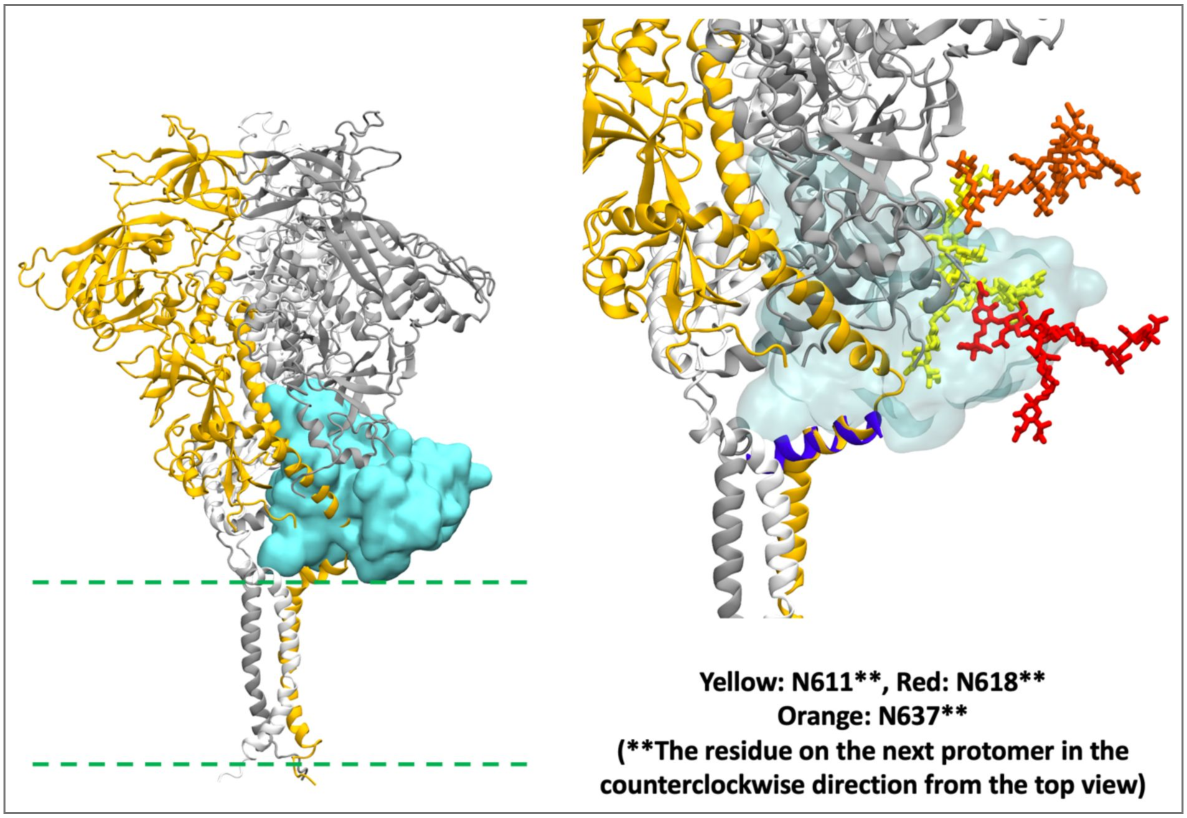

Figure 6—figure supplement 7. Snapshots showing the MPER of one protomer accessible to either 4E10 or 10E8.

(**A**) Snapshot in which the MPER of the white protomer is accessible to 4E10 (cyan transparent surface) but not to 10E8. (**B**) Snapshot in which the MPER of the white protomer is accessible to 10E8 (green transparent surface) but not to 4E10.

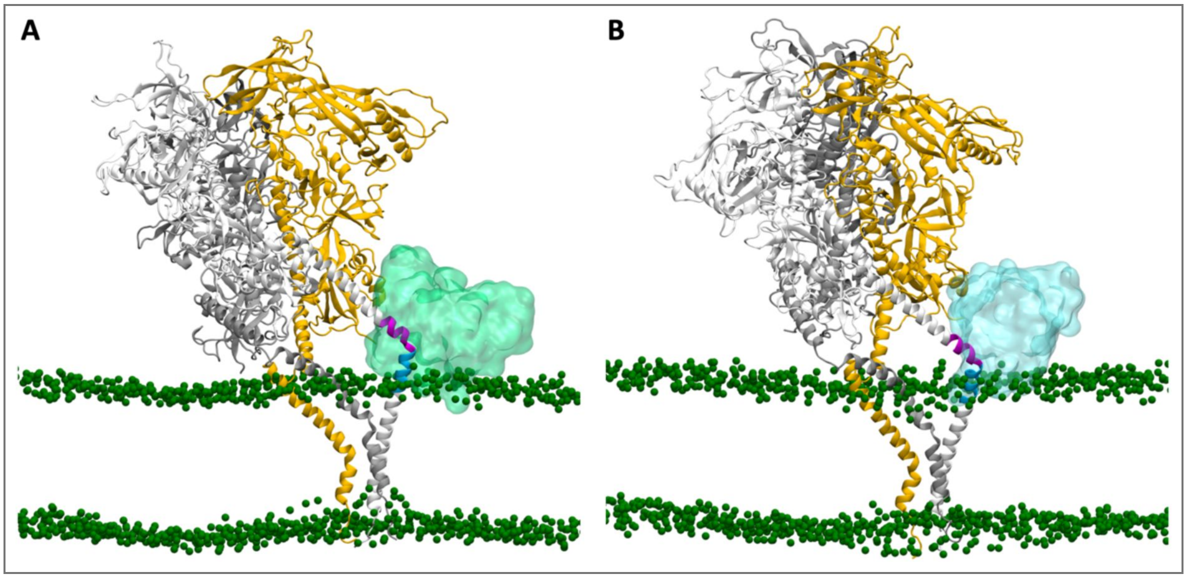

Figure 6—figure supplement 8. Snapshots showing the MPER of two protomers are accessible to 4E10.

The MPER is accessible to 4E10, (**A**) exclusively in the yellow protomer, and (**B**) exclusively in the gray protomer.

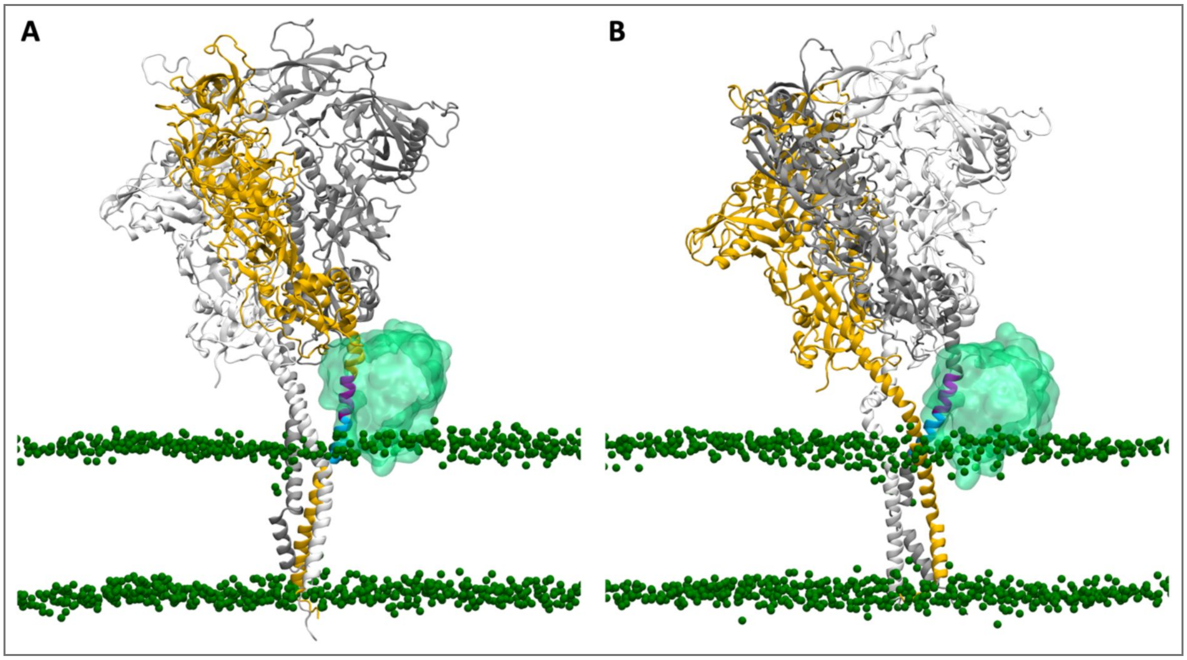

Figure 6—figure supplement 9. Snapshots showing the MPER of two protomers are accessible to 10E8.

The MPER is accessible to 4E10, (**A**) exclusively in the yellow protomer, and (**B**) exclusively in the white protomer.

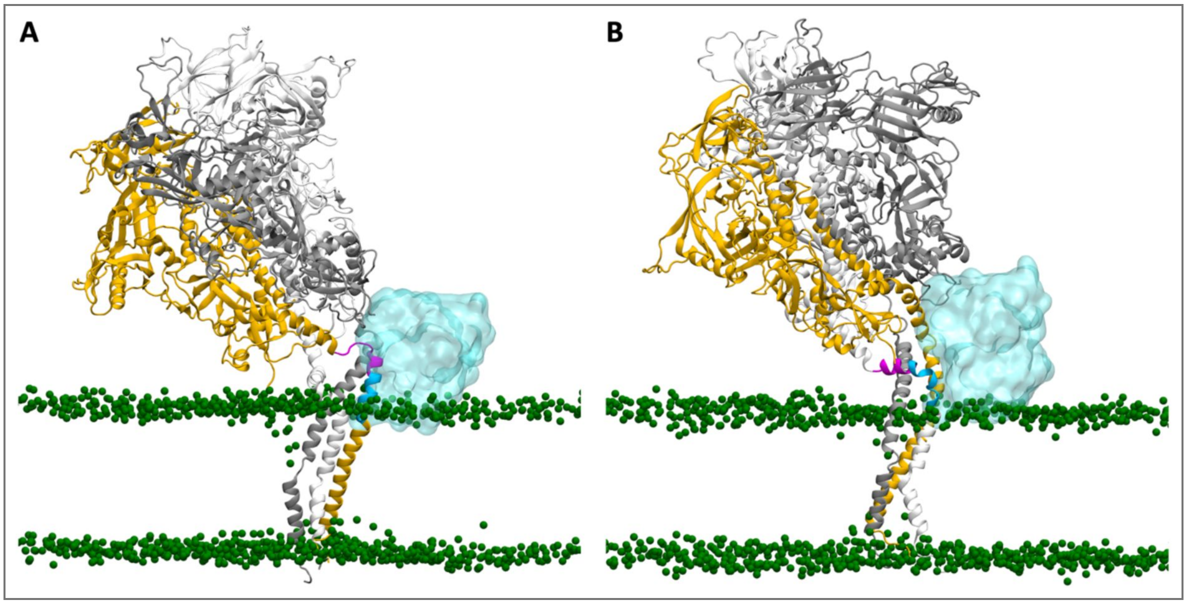

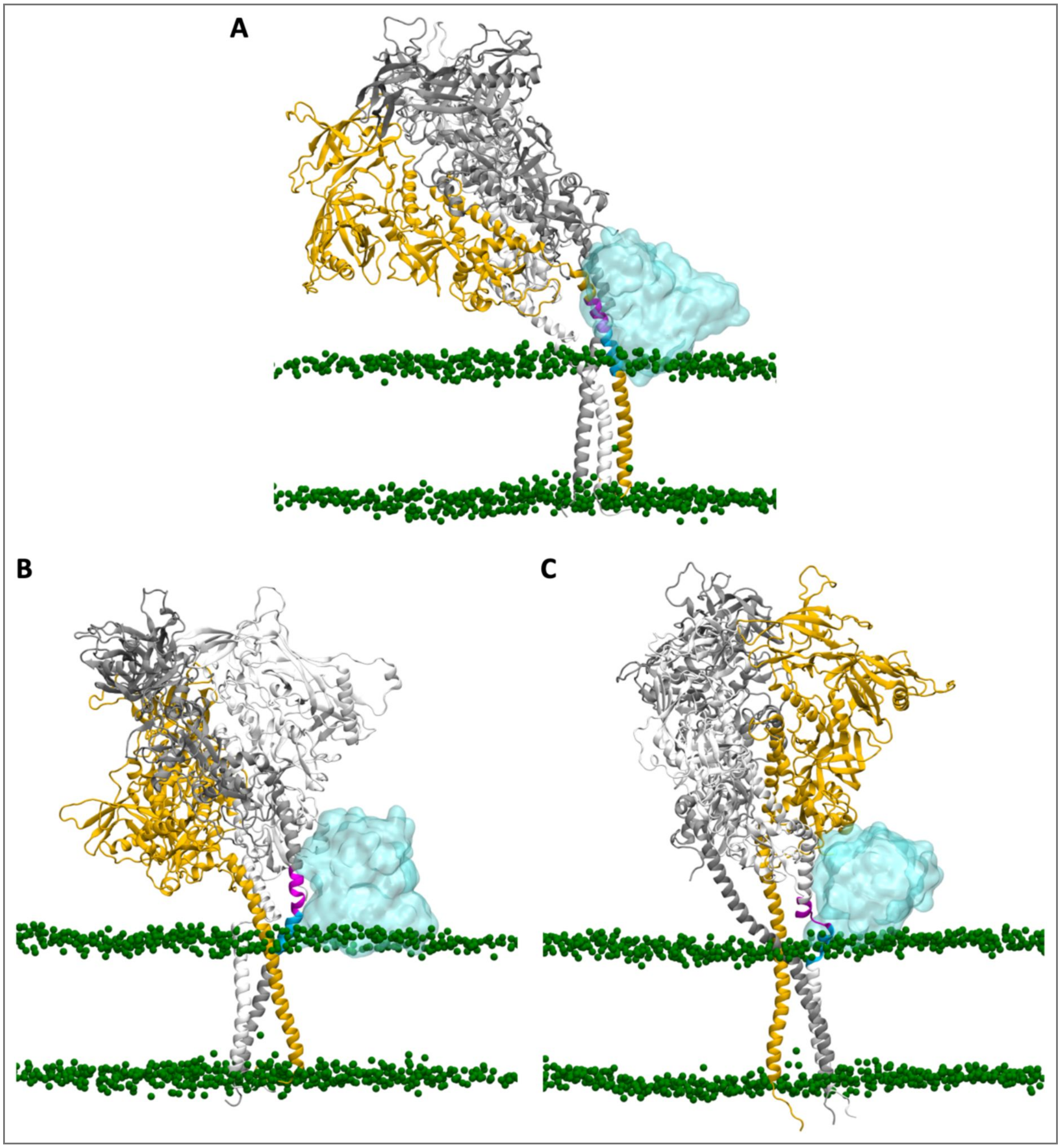

Figure 6—figure supplement 10. Snapshots showing the MPER of three protomers are accessible to 10E8.

The MPER is accessible to 4E10, (**A**) exclusively in the yellow protomer, (**B**) exclusively in the gray protomer, and (**C**) exclusively in the white protomer.

Additional information

Author contributions

Yiwei Cao: Conceptualization, Formal analysis, Investigation, Methodology, Writing – original draft, Writing – review and editing

Wonpil Im: Conceptualization, Funding acquisition, Methodology, Supervision, Writing – review and editing

Funding

Funder	Grant reference number	Author
National Institutes of Health (NIH)	R35-GM153458	Wonpil Im

Author ORCID iDs

Yiwei Cao: https://orcid.org/0000-0002-4516-8689
Wonpil Im: https://orcid.org/0000-0001-5642-6041

Additional files

Supplementary file

References

Alam SM, Morelli M, Dennison SM, Liao HX, Zhang R, Xia SM, Rits-Volloch S, Sun L, Harrison SC, Haynes BF, *et al.* (2009) Role of HIV membrane in neutralization by two broadly neutralizing antibodies. *PNAS* **106**:20234-20239 https://doi.org/10.1073/pnas.0908713106 | PubMed

Aloia RC, Tian H, Jensen FC (1993) Lipid composition and fluidity of the human immunodeficiency virus envelope and host cell plasma membranes. *PNAS* **90**:5181-5185 https://doi.org/10.1073/pnas.90.11.5181 | PubMed

Apellaniz B, Rujas E, Serrano S, Morante K, Tsumoto K, Caaveiro JM, Jimenez MA, Nieva JL (2015) The Atomic Structure of the HIV-1 gp41 Transmembrane Domain and Its Connection to the Immunogenic Membrane-proximal External Region. *Journal of Biological Chemistry* **290**:12999-13015 https://doi.org/10.1074/jbc.m115.644351 | PubMed

Baker MK, Abrams CF (2014) Dynamics of lipids, cholesterol, and transmembrane alpha-helices from microsecond molecular dynamics simulations. *The Journal of Physical Chemistry B* **118**:13590-13600 https://doi.org/10.1021/jp507027t | PubMed

Baker MK, Gangupomu VK, Abrams CF (2014) Characterization of the water defect at the HIV-1 gp41 membrane spanning domain in bilayers with and without cholesterol using molecular simulations. *Biochimica et Biophysica Acta* **1838**:1396-1405 https://doi.org/10.1016/j.bbamem.2014.01.009 | PubMed

Behrens AJ, Vasiljevic S, Pritchard LK, Harvey DJ, Andev RS, Krumm SA, Struwe WB, Cupo A, Kumar A, Zitzmann N, *et al.* (2016) Composition and Antigenic Effects of Individual Glycan Sites of a Trimeric HIV-1 Envelope Glycoprotein. *Cell Reports* **14**:2695-2706 https://doi.org/10.1016/j.celrep.2016.02.058 | PubMed

Berendsen HJC, Postma JPM, van Gunsteren WF, DiNola A, Haak JR (1984) Molecular dynamics with coupling to an external bath. *The Journal of Chemical Physics* **81**:3684-3690 https://doi.org/10.1063/1.448118

Brugger B, Glass B, Haberkant P, Leibrecht I, Wieland FT, Krausslich HG (2006) The HIV lipidome: a raft with an unusual composition. *PNAS* **103**:2641-2646 https://doi.org/10.1073/pnas.0511136103 | PubMed

Cao L, Diedrich JK, Kulp DW, Pauthner M, He L, Park SR, Sok D, Su CY, Delahunty CM, Menis S, *et al.* (2017) Global site-specific N-glycosylation analysis of HIV envelope glycoprotein. *Nature Communications* **8**:14954 https://doi.org/10.1038/ncomms14954 | PubMed

Cardoso RM, Zwick MB, Stanfield RL, Kunert R, Binley JM, Katinger H, Burton DR, Wilson IA (2005) Broadly neutralizing anti-HIV antibody 4E10 recognizes a helical conformation of a highly conserved fusion-associated motif in gp41. *Immunity* **22**:163-173 https://doi.org/10.1016/j.immuni.2004.12.011 | PubMed

Checkley MA, Luttge BG, Freed EO (2011) HIV-1 envelope glycoprotein biosynthesis, trafficking, and incorporation. *Journal of Molecular Biology* **410**:582-608 https://doi.org/10.1016/j.jmb.2011.04.042 | PubMed

Chen J, Frey G, Peng H, Rits-Volloch S, Garrity J, Seaman MS, Chen B (2014) Mechanism of HIV-1 neutralization by antibodies targeting a membrane-proximal region of gp41. *Journal of Virology* **88**:1249-1258 https://doi.org/10.1128/jvi.02664-13 | PubMed

Chen J, Kovacs JM, Peng H, Rits-Volloch S, Lu J, Park D, Zablowsky E, Seaman MS, Chen B (2015) HIV-1 ENVELOPE. Effect of the cytoplasmic domain on antigenic characteristics of HIV-1 envelope glycoprotein. *Science* **349**:191-195 https://doi.org/10.1126/science.aaa9804 | PubMed

Cheng X, Im W (2012) NMR observable-based structure refinement of DAP12-NKG2C activating immunoreceptor complex in explicit membranes. *Biophysical Journal* **102**:L27-29 https://doi.org/10.1016/j.bpj.2012.03.002 | PubMed

Chiliveri SC, Louis JM, Ghirlando R, Baber JL, Bax A (2018) Tilted, Uninterrupted, Monomeric HIV-1 gp41 Transmembrane Helix from Residual Dipolar Couplings. *Journal of the American Chemical Society* **140**:34-37 https://doi.org/10.1021/jacs.7b10245 | PubMed

Dalgleish AG, Beverley PC, Clapham PR, Crawford DH, Greaves MF, Weiss RA (1984) The CD4 (T4) antigen is an essential component of the receptor for the AIDS retrovirus. *Nature* **312**:763-767 https://doi.org/10.1038/312763a0 | PubMed

Dev J, Park D, Fu Q, Chen J, Ha HJ, Ghantous F, Herrmann T, Chang W, Liu Z, Frey G, *et al.* (2016) Structural basis for membrane anchoring of HIV-1 envelope spike. *Science* **353**:172-175 https://doi.org/10.1126/science.aaf7066 | PubMed

Edwards TG, Wyss S, Reeves JD, Zolla-Pazner S, Hoxie JA, Doms RW, Baribaud F (2002) Truncation of the cytoplasmic domain induces exposure of conserved regions in the ectodomain of human immunodeficiency virus type 1 envelope protein. *Journal of Virology* **76**:2683-2691 https://doi.org/10.1128/jvi.76.6.2683-2691.2002 | PubMed

Essmann U, Perera L, Berkowitz ML, Darden T, Lee H, Pedersen LG (1995) A smooth particle mesh Ewald method. *The Journal of Chemical Physics* **103**:8577-8593 https://doi.org/10.1063/1.470117

Feng Y, Broder CC, Kennedy PE, Berger EA (1996) HIV-1 entry cofactor: functional cDNA cloning of a seven-transmembrane. *G protein-coupled receptor Science* **272**:872-877 https://doi.org/10.1126/science.272.5263.872 | PubMed

Frey G, Peng H, Rits-Volloch S, Morelli M, Cheng Y, Chen B (2008) A fusion-intermediate state of HIV-1 gp41 targeted by broadly neutralizing antibodies. *PNAS* **105**:3739-3744 https://doi.org/10.1073/pnas.0800255105 | PubMed

Fu Q, Shaik MM, Cai Y, Ghantous F, Piai A, Peng H, Rits-Volloch S, Liu Z, Harrison SC, Seaman MS, *et al.* (2018) Structure of the membrane proximal external region of HIV-1envelope glycoprotein. *PNAS* **115**:E8892-E8899 https://doi.org/10.1073/pnas.1807259115 | PubMed

Gangupomu VK, Abrams CF (2010) All-atom models of the membrane-spanning domain of HIV-1 gp41 from metadynamics. *Biophysical Journal* **99**:3438-3444 https://doi.org/10.1016/j.bpj.2010.09.054 | PubMed

Guvench O, Hatcher ER, Venable RM, Pastor RW, Mackerell AD (2009) CHARMM Additive All-Atom Force Field for Glycosidic Linkages between Hexopyranoses. *Journal of Chemical Theory and Computation* **5**:2353-2370 https://doi.org/10.1021/ct900242e | PubMed

Guvench O, Mallajosyula SS, Raman EP, Hatcher E, Vanommeslaeghe K, Foster TJ, Jamison FW, Mackerell AD (2011) CHARMM additive all-atom force field for carbohydrate derivatives and its utility in polysaccharide and carbohydrate-protein modeling. *Journal of Chemical Theory and Computation* **7**:3162-3180 https://doi.org/10.1021/ct200328p | PubMed

Hess B, Bekker H, Berendsen HJC, Fraaije JGEM (1997) LINCS: A linear constraint solver for molecular simulations. *Journal of Computational Chemistry* **18**:1463-1472 https://doi.org/10.1002/(sici)1096-987x(199709)18:12<1463::aid-jcc4>3.0.co;2-h

Hollingsworth LRt, Lemkul JA, Bevan DR, Brown AM (2018) HIV-1 Env gp41 Transmembrane Domain Dynamics Are Modulated by Lipid. *Water, and Ion Interactions Biophysical Journal* **115**:84-94 https://doi.org/10.1016/j.bpj.2018.05.022 | PubMed

Hoover WG (1985) Canonical dynamics: Equilibrium phase-space distributions. *Physical Review A, General Physics* **31**:1695-1697 https://doi.org/10.1103/physreva.31.1695 | PubMed

Hopkins CW, Le Grand S, Walker RC, Roitberg AE (2015) Long-Time-Step Molecular Dynamics through Hydrogen Mass Repartitioning. *Journal of Chemical Theory and Computation* **11**:1864-1874 https://doi.org/10.1021/ct5010406 | PubMed

Huang J, Kang BH, Pancera M, Lee JH, Tong T, Feng Y, Imamichi H, Georgiev IS, Chuang GY, Druz A, *et al.* (2014) Broad and potent HIV-1 neutralization by a human antibody that binds the gp41-gp120 interface. *Nature* **515**:138-142 https://doi.org/10.1038/nature13601 | PubMed

Huang J, Ofek G, Laub L, Louder MK, Doria-Rose NA, Longo NS, Imamichi H, Bailer RT, Chakrabarti B, Sharma SK, *et al.* (2012) Broad and potent neutralization of HIV-1 by a gp41-specific human antibody. *Nature* **491**:406-412 https://doi.org/10.1038/nature11544 | PubMed

Huang J, Rauscher S, Nawrocki G, Ran T, Feig M, de Groot BL, Grubmuller H, MacKerell AD (2017) CHARMM36m: an improved force field for folded and intrinsically disordered proteins. *Nature Methods* **14**:71-73 https://doi.org/10.1038/nmeth.4067 | PubMed

Huang Y, Paxton WA, Wolinsky SM, Neumann AU, Zhang L, He T, Kang S, Ceradini D, Jin Z, Yazdanbakhsh K, *et al.* (1996) The role of a mutant CCR5 allele in HIV-1 transmission and disease progression. *Nature Medicine* **2**:1240-1243 https://doi.org/10.1038/nm1196-1240 | PubMed

Huarte N, Carravilla P, Cruz A, Lorizate M, Nieto-Garai JA, Krausslich HG, Perez-Gil J, Requejo-Isidro J, Nieva JL (2016) Functional organization of the HIV lipid envelope. *Scientific Reports* **6**:34190 https://doi.org/10.1038/srep34190 | PubMed

Humphrey W, Dalke A, Schulten K (1996) VMD: visual molecular dynamics. *Journal of Molecular Graphics and Modelling* **14**:33-38 https://doi.org/10.1016/0263-7855(96)00018-5 | PubMed

Ichiye T, Karplus M (1991) Collective motions in proteins: a covariance analysis of atomic fluctuations in molecular dynamics and normal mode simulations. *Proteins* **11**:205-217 https://doi.org/10.1002/prot.340110305 | PubMed

Ingolfsson HI, Melo MN, van Eerden FJ, Arnarez C, Lopez CA, Wassenaar TA, Periole X, de Vries AH, Tieleman DP, Marrink SJ (2014) Lipid organization of the plasma membrane. *Journal of the American Chemical Society* **136**:14554-14559 https://doi.org/10.1021/ja507832e | PubMed

Jo S, Cheng X, Islam SM, Huang L, Rui H, Zhu A, Lee HS, Qi Y, Han W, Vanommeslaeghe K, *et al.* (2014) CHARMM-GUI PDB manipulator for advanced modeling and simulations of proteins containing nonstandard residues. *Advances in Protein Chemistry and Structural Biology* **96**:235-265 https://doi.org/10.1016/bs.apcsb.2014.06.002 | PubMed

Jo S, Kim T, Im W (2007) Automated builder and database of protein/membrane complexes for molecular dynamics simulations. *PLoS One* **2**:e880 https://doi.org/10.1371/journal.pone.0000880 | PubMed

Jo S, Kim T, Iyer VG, Im W (2008) CHARMM-GUI: a web-based graphical user interface for CHARMM. *Journal of Computational Chemistry* **29**:1859-1865 https://doi.org/10.1002/jcc.20945 | PubMed

Jo S, Lim JB, Klauda JB, Im W (2009) CHARMM-GUI Membrane Builder for mixed bilayers and its application to yeast membranes. *Biophysical Journal* **97**:50-58 https://doi.org/10.1016/j.bpj.2009.04.013 | PubMed

Jo S, Song KC, Desaire H, MacKerell AD, Im W (2011) Glycan Reader: automated sugar identification and simulation preparation for carbohydrates and glycoproteins. *Journal of Computational Chemistry* **32**:3135-3141 https://doi.org/10.1002/jcc.21886 | PubMed

Jorgensen WL, Chandrasekhar J, Madura JD, Impey RW, Klein ML (1983) Comparison of simple potential functions for simulating liquid water. *The Journal of Chemical Physics* **79**:926-935 https://doi.org/10.1063/1.445869

Kim JH, Hartley TL, Curran AR, Engelman DM (2009) Molecular dynamics studies of the transmembrane domain of gp41 from HIV-1. *Biochimica et Biophysica Acta* **1788**:1804-1812 https://doi.org/10.1016/j.bbamem.2009.06.011 | PubMed

Klauda JB, Venable RM, Freites JA, O'Connor JW, Tobias DJ, Mondragon-Ramirez C, Vorobyov I, MacKerell AD, Pastor RW (2010) Update of the CHARMM all-atom additive force field for lipids: validation on six lipid types. *The Journal of Physical Chemistry B* **114**:7830-7843 https://doi.org/10.1021/jp101759q | PubMed

Kong L, He L, de Val N, Vora N, Morris CD, Azadnia P, Sok D, Zhou B, Burton DR, Ward AB, *et al.* (2016) Uncleaved prefusion-optimized gp140 trimers derived from analysis of HIV-1 envelope metastability. *Nature Communications* **7**:12040 https://doi.org/10.1038/ncomms12040 | PubMed

Kwon B, Lee M, Waring AJ, Hong M (2018) Oligomeric Structure and Three-Dimensional Fold of the HIV gp41 Membrane-Proximal External Region and Transmembrane Domain in Phospholipid Bilayers. *Journal of the American Chemical Society* **140**:8246-8259 https://doi.org/10.1021/jacs.8b04010 | PubMed

Lee J, Cheng X, Swails JM, Yeom MS, Eastman PK, Lemkul JA, Wei S, Buckner J, Jeong JC, Qi Y, *et al.* (2016) CHARMM-GUI Input Generator for NAMD, GROMACS, AMBER, OpenMM, and CHARMM/OpenMM Simulations Using the CHARMM36 Additive Force Field. *Journal of Chemical Theory and Computation* **12**:405-413 https://doi.org/10.1021/acs.jctc.5b00935 | PubMed

Lee J, Patel DS, Stahle J, Park SJ, Kern NR, Kim S, Lee J, Cheng X, Valvano MA, Holst O, *et al.* (2019) CHARMM-GUI Membrane Builder for Complex Biological Membrane Simulations with Glycolipids and Lipoglycans. *Journal of Chemical Theory and Computation* **15**:775-786 https://doi.org/10.1021/acs.jctc.8b01066 | PubMed

Lee JH, Ozorowski G, Ward AB (2016) Cryo-EM structure of a native, fully glycosylated, cleaved HIV-1 envelope trimer. *Science* **351**:1043-1048 https://doi.org/10.1126/science.aad2450 | PubMed

Maillie CA, Golden K, Wilson IA, Ward AB, Mravic M (2025) Ab initio prediction of specific phospholipid complexes and membrane association of HIV-1 MPER antibodies by multi-scale simulations. *eLife* **12** https://doi.org/10.7554/elife.90139 | PubMed

Majumder A, Voth GA (2025) Structural Heterogeneity of the Membrane-Interacting Region of the HIV-1 Envelope Glycoprotein. *Journal of the American Chemical Society* **147**:45347-45356 https://doi.org/10.1021/jacs.5c15421 | PubMed

McCune JM, Rabin LB, Feinberg MB, Lieberman M, Kosek JC, Reyes GR, Weissman IL (1988) Endoproteolytic cleavage of gp160 is required for the activation of human immunodeficiency virus. *Cell* **53**:55-67 https://doi.org/10.1016/0092-8674(88)90487-4 | PubMed

McGibbon RT, Beauchamp KA, Harrigan MP, Klein C, Swails JM, Hernandez CX, Schwantes CR, Wang LP, Lane TJ, Pande VS (2015) MDTraj: A Modern Open Library for the Analysis of Molecular Dynamics Trajectories. *Biophysical Journal* **109**:1528-1532 https://doi.org/10.1016/j.bpj.2015.08.015 | PubMed

McLellan JS, Pancera M, Carrico C, Gorman J, Julien JP, Khayat R, Louder R, Pejchal R, Sastry M, Dai K, *et al.* (2011) Structure of HIV-1 gp120 V1/V2 domain with broadly neutralizing antibody PG9. *Nature* **480**:336-343 https://doi.org/10.1038/nature10696 | PubMed

Miyauchi K, Komano J, Yokomaku Y, Sugiura W, Yamamoto N, Matsuda Z (2005) Role of the specific amino acid sequence of the membrane-spanning domain of human immunodeficiency virus type 1 in membrane fusion. *Journal of Virology* **79**:4720-4729 https://doi.org/10.1128/jvi.79.8.4720-4729.2005 | PubMed

Mucksch F, Citir M, Luchtenborg C, Glass B, Traynor-Kaplan A, Schultz C, Brugger B, Krausslich HG (2019) Quantification of phosphoinositides reveals strong enrichment of PIP(2) in HIV-1 compared to producer cell membranes. *Scientific Reports* **9**:17661 https://doi.org/10.1038/s41598-019-53939-z | PubMed

Munro JB, Gorman J, Ma X, Zhou Z, Arthos J, Burton DR, Koff WC, Courter JR, Smith AB, Kwong PD, *et al.* (2014) Conformational dynamics of single HIV-1 envelope trimers on the surface of native virions. *Science* **346**:759-763 https://doi.org/10.1126/science.1254426 | PubMed

Murphy RE, Samal AB, Vlach J, Saad JS (2017) Solution Structure and Membrane Interaction of the Cytoplasmic Tail of HIV-1 gp41 Protein. *Structure* **25**:1708-1718.e1705 https://doi.org/10.1016/j.str.2017.09.010 | PubMed

Nosé S (2006) A molecular dynamics method for simulations in the canonical ensemble. *Molecular Physics* **52**:255-268 https://doi.org/10.1080/00268978400101201

Nosé S, Klein ML (2006) Constant pressure molecular dynamics for molecular systems. *Molecular Physics* **50**:1055-1076 https://doi.org/10.1080/00268978300102851

Ofek G, Tang M, Sambor A, Katinger H, Mascola JR, Wyatt R, Kwong PD (2004) Structure and mechanistic analysis of the anti-human immunodeficiency virus type 1 antibody 2F5 in complex with its gp41 epitope. *Journal of Virology* **78**:10724-10737 https://doi.org/10.1128/jvi.78.19.10724-10737.2004 | PubMed

Pancera M, Zhou T, Druz A, Georgiev IS, Soto C, Gorman J, Huang J, Acharya P, Chuang GY, Ofek G, *et al.* (2014) Structure and immune recognition of trimeric pre-fusion HIV-1 Env. *Nature* **514**:455-461 https://doi.org/10.1038/nature13808 | PubMed

Park SJ, Kern N, Brown T, Lee J, Im W (2023) CHARMM-GUI PDB Manipulator: Various PDB Structural Modifications for Biomolecular Modeling and Simulation. *Journal of Molecular Biology* **435**:167995 https://doi.org/10.1016/j.jmb.2023.167995 | PubMed

Park SJ, Lee J, Patel DS, Ma H, Lee HS, Jo S, Im W (2017) Glycan Reader is improved to recognize most sugar types and chemical modifications in the Protein Data Bank. *Bioinformatics* **33**:3051-3057 https://doi.org/10.1093/bioinformatics/btx358 | PubMed

Park SJ, Lee J, Qi Y, Kern NR, Lee HS, Jo S, Joung I, Joo K, Lee J, Im W (2019) CHARMM-GUI Glycan Modeler for modeling and simulation of carbohydrates and glycoconjugates. *Glycobiology* **29**:320-331 https://doi.org/10.1093/glycob/cwz003 | PubMed

Parrinello M, Rahman A (1981) Polymorphic transitions in single crystals: A new molecular dynamics method. *Journal of Applied Physics* **52**:7182-7190 https://doi.org/10.1063/1.328693

Pejchal R, Gach JS, Brunel FM, Cardoso RM, Stanfield RL, Dawson PE, Burton DR, Zwick MB, Wilson IA (2009) A conformational switch in human immunodeficiency virus gp41 revealed by the structures of overlapping epitopes recognized by neutralizing antibodies. *Journal of Virology* **83**:8451-8462 https://doi.org/10.1128/jvi.00685-09 | PubMed

Piai A, Fu Q, Cai Y, Ghantous F, Xiao T, Shaik MM, Peng H, Rits-Volloch S, Chen W, Seaman MS, *et al.* (2020) Structural basis of transmembrane coupling of the HIV-1 envelope glycoprotein. *Nature Communications* **11**:2317 https://doi.org/10.1038/s41467-020-16165-0 | PubMed

Piai A, Fu Q, Sharp AK, Bighi B, Brown AM, Chou JJ (2021) NMR Model of the Entire Membrane-Interacting Region of the HIV-1 Fusion Protein and Its Perturbation of Membrane Morphology. *Journal of the American Chemical Society* **143**:6609-6615 https://doi.org/10.1021/jacs.1c01762 | PubMed

Pogozheva ID, Armstrong GA, Kong L, Hartnagel TJ, Carpino CA, Gee SE, Picarello DM, Rubin AS, Lee J, Park S, *et al.* (2022) Comparative Molecular Dynamics Simulation Studies of Realistic Eukaryotic. *Prokaryotic, and Archaeal Membranes Journal of Chemical Information and Modeling* **62**:1036-1051 https://doi.org/10.1021/acs.jcim.1c01514 | PubMed

Qi Y, Zhang S, Wang K, Ding H, Zhang Z, Anang S, Nguyen HT, Kappes JC, Sodroski J, Mao Y (2025) The membrane-proximal external region of human immunodeficiency virus (HIV-1) envelope glycoprotein trimers in A18-lipid nanodiscs. *Communications Biology* **8**:442 https://doi.org/10.1038/s42003-025-07852-z | PubMed

Raman EP, Guvench O, MacKerell AD (2010) CHARMM additive all-atom force field for glycosidic linkages in carbohydrates involving furanoses. *The Journal of Physical Chemistry B* **114**:12981-12994 https://doi.org/10.1021/jp105758h | PubMed

Rantalainen K, Berndsen ZT, Antanasijevic A, Schiffner T, Zhang X, Lee WH, Torres JL, Zhang L, Irimia A, Copps J, *et al.* (2020) HIV-1 Envelope and MPER Antibody Structures in Lipid Assemblies. *Cell Reports* **31**:107583 https://doi.org/10.1016/j.celrep.2020.107583 | PubMed

Reardon PN, Sage H, Dennison SM, Martin JW, Donald BR, Alam SM, Haynes BF, Spicer LD (2014) Structure of an HIV-1-neutralizing antibody target, the lipid-bound gp41 envelope membrane proximal region trimer. *PNAS* **111**:1391-1396 https://doi.org/10.1073/pnas.1309842111 | PubMed

Roe DR, Cheatham TE (2013) PTRAJ and CPPTRAJ: Software for Processing and Analysis of Molecular Dynamics Trajectory Data. *Journal of Chemical Theory and Computation* **9**:3084-3095 https://doi.org/10.1021/ct400341p | PubMed

Salzwedel K, West JT, Hunter E (1999) A conserved tryptophan-rich motif in the membrane-proximal region of the human immunodeficiency virus type 1 gp41 ectodomain is important for Env-mediated fusion and virus infectivity. *Journal of Virology* **73**:2469-2480 https://doi.org/10.1128/jvi.73.3.2469-2480.1999 | PubMed

Sampaio JL, Gerl MJ, Klose C, Ejsing CS, Beug H, Simons K, Shevchenko A (2011) Membrane lipidome of an epithelial cell line. *PNAS* **108**:1903-1907 https://doi.org/10.1073/pnas.1019267108 | PubMed

Sanders RW, Derking R, Cupo A, Julien JP, Yasmeen A, de Val N, Kim HJ, Blattner C, de la Pena AT, Korzun J, *et al.* (2013) A next-generation cleaved, soluble HIV-1 Env trimer, BG505 SOSIP.664 gp140, expresses multiple epitopes for broadly neutralizing but not non-neutralizing antibodies. *PLOS Pathogens* **9**:e1003618 https://doi.org/10.1371/journal.ppat.1003618 | PubMed

Sarkar A, Bale S, Behrens AJ, Kumar S, Sharma SK, de Val N, Pallesen J, Irimia A, Diwanji DC, Stanfield RL, *et al.* (2018) Structure of a cleavage-independent HIV Env recapitulates the glycoprotein architecture of the native cleaved trimer. *Nature Communications* **9**:1956 https://doi.org/10.1038/s41467-018-04272-y | PubMed

Sharma SK, de Val N, Bale S, Guenaga J, Tran K, Feng Y, Dubrovskaya V, Ward AB, Wyatt RT (2015) Cleavage-independent HIV-1 Env trimers engineered as soluble native spike mimetics for vaccine design. *Cell Reports* **11**:539-550 https://doi.org/10.1016/j.celrep.2015.03.047 | PubMed

Sharp PM, Hahn BH (2011) Origins of HIV and the AIDS pandemic. *Cold Spring Harbor Perspectives in Medicine* **1**:a006841 https://doi.org/10.1101/cshperspect.a006841 | PubMed

Shehata M, Casalino L, Duquette M, Chen S, Flaherty A, Villa E, Amaro RE (2025) N-Glycans Modulate HIV-1 Env Conformational Plasticity. *bioRxiv* 2025.2003.2026.645577 https://doi.org/10.1101/2025.03.26.645577

Steinbach PJ, Brooks BR (2004) New spherical-cutoff methods for long-range forces in macromolecular simulation. *Journal of Computational Chemistry* **15**:667-683 https://doi.org/10.1002/jcc.540150702

Sun ZY, Oh KJ, Kim M, Yu J, Brusic V, Song L, Qiao Z, Wang JH, Wagner G, Reinherz EL (2008) HIV-1 broadly neutralizing antibody extracts its epitope from a kinked gp41 ectodomain region on the viral membrane. *Immunity* **28**:52-63 https://doi.org/10.1016/j.immuni.2007.11.018 | PubMed

Tomishige N, Bin Nasim M, Murate M, Pollet B, Didier P, Godet J, Richert L, Sako Y, Mely Y, Kobayashi T (2023) HIV-1 Gag targeting to the plasma membrane reorganizes sphingomyelin-rich and cholesterol-rich lipid domains. *Nature Communications* **14**:7353 https://doi.org/10.1038/s41467-023-42994-w | PubMed

Van Der Spoel D, Lindahl E, Hess B, Groenhof G, Mark AE, Berendsen HJ (2005) GROMACS: fast, flexible, and free. *Journal of Computational Chemistry* **26**:1701-1718 https://doi.org/10.1002/jcc.20291 | PubMed

van Meer G, Voelker DR, Feigenson GW (2008) Membrane lipids: where they are and how they behave. *Nature Reviews Molecular Cell Biology* **9**:112-124 https://doi.org/10.1038/nrm2330 | PubMed

Walker LM, Huber M, Doores KJ, Falkowska E, Pejchal R, Julien JP, Wang SK, Ramos A, Chan-Hui PY, Moyle M, *et al.* (2011) Broad neutralization coverage of HIV by multiple highly potent antibodies. *Nature* **477**:466-470 https://doi.org/10.1038/nature10373 | PubMed

Walker LM, Phogat SK, Chan-Hui PY, Wagner D, Phung P, Goss JL, Wrin T, Simek MD, Fling S, Mitcham JL, *et al.* (2009) Broad and potent neutralizing antibodies from an African donor reveal a new HIV-1 vaccine target. *Science* **326**:285-289 https://doi.org/10.1126/science.1178746 | PubMed

Wei X, Decker JM, Wang S, Hui H, Kappes JC, Wu X, Salazar-Gonzalez JF, Salazar MG, Kilby JM, Saag MS, *et al.* (2003) Antibody neutralization and escape by HIV-1. *Nature* **422**:307-312 https://doi.org/10.1038/nature01470 | PubMed

Williams LD, Ofek G, Schatzle S, McDaniel JR, Lu X, Nicely NI, Wu L, Lougheed CS, Bradley T, Louder MK, *et al.* (2017) Potent and broad HIV-neutralizing antibodies in memory B cells and plasma. *Science Immunology* **2**:eaal2200 https://doi.org/10.1126/sciimmunol.aal2200 | PubMed

Wu EL, Cheng X, Jo S, Rui H, Song KC, Davila-Contreras EM, Qi Y, Lee J, Monje-Galvan V, Venable RM, *et al.* (2014) CHARMM-GUI Membrane Builder toward realistic biological membrane simulations. *Journal of Computational Chemistry* **35**:1997-2004 https://doi.org/10.1002/jcc.23702 | PubMed

Wu X, Yang ZY, Li Y, Hogerkorp CM, Schief WR, Seaman MS, Zhou T, Schmidt SD, Wu L, Xu L, *et al.* (2010) Rational design of envelope identifies broadly neutralizing human monoclonal antibodies to HIV-1. *Science* **329**:856-861 https://doi.org/10.1126/science.1187659 | PubMed

Wyatt R, Sodroski J (1998) The HIV-1 envelope glycoproteins: fusogens, antigens, and immunogens. *Science* **280**:1884-1888 https://doi.org/10.1126/science.280.5371.1884 | PubMed

Yang J, Zhang Y (2015) I-TASSER server: new development for protein structure and function predictions. *Nucleic Acids Research* **43**:W174-181 https://doi.org/10.1093/nar/gkv342 | PubMed

Yang S, Hiotis G, Wang Y, Chen J, Wang JH, Kim M, Reinherz EL, Walz T (2022) Dynamic HIV-1 spike motion creates vulnerability for its membrane-bound tripod to antibody attack. *Nature Communications* **13**:6393 https://doi.org/10.1038/s41467-022-34008-y | PubMed

Zhang S, Nguyen HT, Ding H, Wang J, Zou S, Liu L, Guha D, Gabuzda D, Ho DD, Kappes JC, *et al.* (2021) Dual Pathways of Human Immunodeficiency Virus Type 1 Envelope Glycoprotein Trafficking Modulate the Selective Exclusion of Uncleaved Oligomers from Virions. *Journal of Virology* **95** https://doi.org/10.1128/jvi.01369-20 | PubMed

Zhang Y, Skolnick J (2005) TM-align: a protein structure alignment algorithm based on the TM-score. *Nucleic Acids Research* **33**:2302-2309 https://doi.org/10.1093/nar/gki524 | PubMed

Zhou T, Zhu J, Wu X, Moquin S, Zhang B, Acharya P, Georgiev IS, Altae-Tran HR, Chuang GY, Joyce MG, *et al.* (2013) Multidonor analysis reveals structural elements, genetic determinants, and maturation pathway for HIV-1 neutralization by VRC01-class antibodies. *Immunity* **39**:245-258 https://doi.org/10.1016/j.immuni.2013.04.012 | PubMed

Peer reviews

Reviewer #3 (Public review):

Summary:

This study uses large-scale all-atom molecular dynamics simulations to examine the conformational plasticity of the HIV-1 envelope glycoprotein (Env) in a membrane context, with particular emphasis on how the transmembrane domain (TMD), cytoplasmic tail (CT), protomer cleavage, and membrane environment influence ectodomain orientation and antibody epitope exposure. By comparing Env constructs with and without the CT, explicitly modeling glycosylation, and embedding Env in an asymmetric lipid bilayer, the authors aim to provide an integrated view of how membrane-proximal regions and lipid interactions shape Env antigenicity, including epitopes targeted by MPER-directed antibodies.

Strengths:

The authors have made a heroic effort to address the concerns raised in the first two rounds of review, and the revised manuscript is substantively improved. The addition of dynamical cross-correlation maps, expanded citation of prior computational work, clarification of the membrane composition rationale, data deposition to Zenodo, and new contextualization has improved the flow and interpretation of the manuscript throughout. Several scientifically interesting aspects of the work merit highlighting with a brief discussion on how future studies can leverage this data to build upon its impact.

A key strength of this work remains the scope, scale, and realism of the simulation systems. The authors construct a very large, nearly complete-Env-scale model that includes a glycosylated Env trimer embedded in an asymmetric bilayer, enabling analysis of membrane-protein interactions that are difficult to capture experimentally. The inclusion of specific glycans at reported sites, and the focus on constructs with and without the CT or cleavage, are well motivated by existing biological and structural data.

The observation that R696 orientation and its interacting partners give rise to asymmetric protomer conformations and distinct TMD tilts is a notable finding. The statement that interactions between R696 and lipid headgroups or CT residues can be strong enough to introduce a kink into the TMD is well-supported by representative snapshots and consistent with prior isolated-TMD simulations. The use of two initialization depths ("high" and "low") to probe R696 leaflet preference is methodologically interesting and the authors' interpretation - that there is a slight bias toward cytoplasmic leaflet interactions, but that these contacts could be highly dynamic over the course of viral entry - is appropriately cautious. It would be valuable to explicitly frame this as a hypothesis with testable predictions that future experimental or enhanced-sampling work could address. Similarly, the equilibration-driven kinking of the TMD core, consistent with prior isolated-TMD studies, represents a useful validation that extends those earlier observations to the intact trimeric context.

The simulations reveal substantial tilting motions of the ectodomain relative to the membrane, with angles spanning roughly 0-30{degree sign} (and up to ~40{degree sign} in some analyses), while the ectodomain itself remains relatively rigid. This framing, that much of Env's conformational variability arises from rigid-body tilting rather than large internal rearrangements, is an important conceptual contribution. The authors also provide interesting observations regarding asymmetric bilayer deformations, including localized thinning and altered lipid headgroup interactions near the TMD and CT, which suggest a reciprocal coupling between Env and the surrounding membrane.

The analysis of antibody-relevant epitopes across the prefusion state, including the V1/V2 and V3 loops, the CD4 binding site, and the MPER, is another strength. The study makes effective use of existing experimental knowledge in this context, for example by focusing on specific glycans known to occlude antibody binding, to motivate and interpret the simulations.

Finally, the revised text provides clear context that situates the study's findings and discrepancies within the broader literature, strengthening the manuscript's clarity and interpretability.

Future work in the field:

As the authors appropriately acknowledge within in the text, these microsecond simulations capture only the closed ground state and with limited sampling due to the already computationally intensive nature of these simulations. Their simulation setup provides interesting foundational knowledge of this state and a framework for these additional important questions.

Additionally, the authors appropriately acknowledge that CT-TMD and CT-ectodomain correlations are difficult to interpret given limited structural confidence in these regions. Future experimental and computational work in the field can extend and build upon the author's framework, particularly as the authors have made their trajectories available for the public. Re-analysis of the authors' deposited MD trajectories-such as probing for exposure of cryptic epitopes and potential allosteric coupling-could serve as valuable extensions of this work, particularly as advancements in computational analysis has reached an inflection point.

Comments on revised version.

Bravo! The improved clarity was a delight to read and will increase the impact this study has on the field.

https://doi.org/10.7554/eLife.110107.3.sa1

Author response:

The following is the authors’ response to the previous reviews

> ***Public Reviews:***
>
> ***Reviewer #1 (Public review):***
>
> *Summary:*
>
> *In the manuscript "Conformational Variability of HIV-1 Env Trimer and Viral Vulnerability", the authors study the fully glycosylated HIV-1 Env protein using an all-atom forcefield. It combines long all-atom simulations of Env in a realistic asymmetric bilayer with careful data analysis. This work clarifies how the CT domain modulates the overall conformation of the Env ectodomain and characterizes different MPER-TMD conformations. The authors also carefully analyze the accessibility of different antibodies to the Env protein.*
>
> *Strengths:*
>
> *This paper is state-of-the-art given the scale of the system and the sophistication of the methods. The biological question is important, the methodology is rigorous, and the results will interest a broad elife audience. The authors also establish strong connections to previous literature and acknowledge the limitations of the CT-truncated protein construct, which enhances the manuscript's relevance to the community.*
>
> ***Reviewer #2 (Public review):***
>
> *In this work, the authors elucidate how a viral surface protein behaves in a membrane environment and how its large-scale motions influence the exposure of antibody-binding sites. Using long-timescale, all-atom molecular dynamics simulations of a fully glycosylated, full-length protein embedded in a virus-like membrane, the study systematically examines the coupling between ectodomain motion, transmembrane orientation, membrane interactions, and epitope accessibility. Multiple model variants differing in cleavage state, initial transmembrane configuration, and presence of the*

cytoplasmic tail are compared to identify general features of protein-membrane dynamics relevant to antibody recognition.

A major strength of this study is the scope and ambition of the simulations. The authors perform multiple microsecond-scale simulations of a highly complex, biologically realistic system that includes the full ectodomain, transmembrane region, cytoplasmic tail, glycans, and a heterogeneous membrane. The finding that the ectodomain explores a wide range of tilt angles while the transmembrane region remains more constrained, with limited correlation between the two, offers useful conceptual insight into how global motions may be accommodated without large rearrangements at the membrane anchor. The explicit consideration of membrane and glycan steric effects on antibody accessibility further strengthens the study.

The main limitations relate to sampling and model dependence inherent to simulations of this size and complexity. The analysis of antibody accessibility is based on geometric and steric criteria, which do not capture potential conformational adaptations of antibodies or membrane remodeling during binding; the authors have appropriately noted this as a limitation.

In the revised manuscript, the authors have addressed all previously raised concerns. Time series plots of the tilt angles have been added, figure captions and visual encodings have been clarified, quantitative descriptions of angular distributions have been strengthened, and the distance metric for MPER exposure is now accompanied by temporal data. The overall presentation is substantially improved, and the conclusions are well supported by the data as presented.

Reviewer #3 (Public review):

Summary:

This study uses large-scale all-atom molecular dynamics simulations to examine the conformational plasticity of the HIV-1 envelope glycoprotein glycoprotein (Env) in a membrane context, with particular emphasis on how the transmembrane domain (TMD), cytoplasmic tail (CT), protomer cleavage, and membrane environment influence ectodomain orientation and antibody epitope exposure. By comparing Env constructs with and without the CT, explicitly modeling glycosylation, and embedding Env in an asymmetric lipid bilayer, the authors aim to provide an integrated view of how membrane-proximal regions and lipid interactions shape Env antigenicity, including epitopes targeted by MPER-directed antibodies.

Strengths:

The authors have made a genuine effort to address the concerns raised in the first round of review, and the revised manuscript is substantively improved. The addition of dynamical cross-correlation maps, expanded citation of prior computational work, clarification of the membrane composition rationale, data deposition to Zenodo, and the new discussion contextualizing the independence of ectodomain and TMD motions are all welcome. Several scientifically interesting aspects of the work merit highlighting before the remaining concerns are addressed.

A key strength of this work remains the scope, scale, and realism of the simulation systems. The authors construct a very large, nearly complete-Env-scale model that includes a glycosylated Env trimer embedded in an asymmetric bilayer, enabling analysis of membrane-protein interactions that are difficult to capture experimentally. The inclusion of specific glycans at reported sites, and the focus on constructs with and without the CT or cleavage, are well motivated by existing biological and structural data.

The observation that R696 orientation and its interacting partners give rise to asymmetric protomer conformations and distinct TMD tilts is a notable finding. The statement that interactions between R696 and lipid headgroups or CT residues can be strong enough to introduce a kink into the TMD is well-supported by representative snapshots and consistent with prior isolated-TMD simulations. The use of two initialization depths ("high" and "low") to probe R696 leaflet preference is methodologically interesting and the authors' interpretation - that there is a slight bias toward cytoplasmic leaflet interactions, but that these contacts could be highly dynamic over the course of viral entry - is appropriately cautious. It would be valuable to explicitly frame this as a hypothesis with testable predictions that future experimental or enhanced-sampling work could address. Similarly, the equilibration-driven kinking of the TMD core, consistent with prior isolated-TMD studies, represents a useful validation that extends those earlier observations to the intact trimeric context.

The simulations reveal substantial tilting motions of the ectodomain relative to the membrane, with angles spanning roughly 0-30° (and up to ~40° in some analyses), while the ectodomain itself remains relatively rigid. This framing, that much of Env's conformational variability arises from rigid-body tilting rather than large internal rearrangements, is an important conceptual contribution. The authors also provide interesting observations regarding asymmetric bilayer deformations, including localized thinning and altered lipid headgroup interactions near the TMD and CT, which suggest a reciprocal coupling between Env and the surrounding membrane.

The analysis of antibody-relevant epitopes across the prefusion state, including the V1/V2 and V3 loops, the CD4 binding site, and the MPER, is another strength. The study makes effective use of existing experimental knowledge in this context, for example by focusing on specific glycans known to occlude antibody binding, to motivate and interpret the simulations.

Finally, the revised discussion provides more context that situates the study's findings and discrepancies within the broader literature, strengthening the manuscript's clarity and interpretability.

Weaknesses:

The revised work is much improved, but still includes substantive issues with writing including organization, such as paragraph run-ons, and citation issues. Improving these would help readers make the most of this important study.

The revised Introduction now includes a paragraph summarizing prior MD work, which is an Improvement. However, the paragraph remains structured around the limitations and setup of previous studies (e.g., "early studies were constrained by limited computational resources", short trajectory lengths, isolated constructs) rather than their findings. Readers benefit most from understanding what those studies showed - and where the present work confirms, extends, or diverges from those results. The current framing inadvertently positions prior work as deficient scaffolding rather than as independent data points converging on shared conclusions. The Introduction could be revised to briefly summarize the key biological conclusions from prior MD studies alongside their technical context, which could then be revisited in their appropriate place alongside key results.

The authors have verified that PDB entries are cited at first mention, and this is noted. However, a recurring issue remains: key literature-supported conclusions appear in the Results and Discussion sections without accompanying citations at each point of use. Passages that summarize experimental or computational findings - particularly those

> *used to validate or contextualize the authors' own results - require citation at every point of claim, not only at first introduction of a reference. This is not a minor stylistic preference. Downstream readers, systematic reviewers, and automated tools that map literature to claims (e.g., scite) rely on co-occurrence of claims and citations within the same passage. A citation appearing several paragraphs earlier does not carry attribution forward. As a practical example: the statement that "MPER-targeting antibodies bind effectively only after the gp120-gp41 trimer undergoes major conformational rearrangements toward a fusion-intermediate or post-fusion state (Frey et al., 2008; Alam et al., 2009; Chen et al., 2014; Lee et al., 2016)", which is appropriate. That same standard of inline attribution should be applied throughout - including in Results and Discussion subsections where prior experimental findings are mentioned without citation.*
>
> *Additionally, cited literature should be framed to highlight convergence with the authors' conclusions, not primarily to limitations of previous studies. Where prior studies independently support a finding, this should be stated explicitly. Independent replication across methods and systems is one of the strongest arguments for ground truth; treating it as such would improve the manuscript's scientific standing.*
>
> *Finally, the dynamical cross-correlation maps assess ectodomain-TMD coupling, and the authors appropriately acknowledge that microsecond simulations capture only the closed ground state. However, the revised manuscript does not address the question raised in the first review regarding CT-TMD and CT-ectodomain correlations. The Results section states that "very weak correlations between the ectodomain and the TMD" were found, but it is not clear whether the CT was included in this analysis or whether analogous correlation maps for CT-TMD and CT-ectodomain pairs were computed for the full-length systems. Additional analyses of the authors' deposited MD trajectories-such as probing for exposure of cryptic epitopes and potential allosteric coupling-could serve as valuable extensions of this work.*

We thank the Reviewer for the further comments and suggestions. We have revised the manuscript accordingly.

> *The observation that R696 orientation and its interacting partners give rise to asymmetric protomer conformations and distinct TMD tilts is a notable finding. The statement that interactions between R696 and lipid headgroups or CT residues can be strong enough to introduce a kink into the TMD is well-supported by representative snapshots and consistent with prior isolated-TMD simulations. The use of two initialization depths ("high" and "low") to probe R696 leaflet preference is methodologically interesting and the authors' interpretation - that there is a slight bias toward cytoplasmic leaflet interactions, but that these contacts could be highly dynamic over the course of viral entry - is appropriately cautious. It would be valuable to explicitly frame this as a hypothesis with testable predictions that future experimental or enhanced-sampling work could address. Similarly, the equilibration-driven kinking of the TMD core, consistent with prior isolated-TMD studies, represents a useful validation that extends those earlier observations to the intact trimeric context.*

At the end of the subsection “The energetically unfavorable R696 in the hydrophobic core results in asymmetric, kinked TMD conformations and disrupts membrane integrity” we have added

“Taken together, these observations suggest that interactions of R696 with lipid headgroups and CT residues may modulate TMD tilt and kink formation during viral entry. However, whether the orientation of R696 dynamically switches between the two leaflets over longer timescales and whether a preference exists for either leaflet remain to be examined in future experimental and/or enhanced sampling simulation studies.”

> *The revised Introduction now includes a paragraph summarizing prior MD work, which is an improvement. However, the paragraph remains structured around the limitations and setup of previous studies (e.g., "early studies were constrained by limited computational resources", short trajectory lengths, isolated constructs) rather than their findings. Readers benefit most from understanding what those studies showed - and where the present work confirms, extends, or diverges from those results. The current framing inadvertently positions prior work as deficient scaffolding rather than as independent data points converging on shared conclusions. The Introduction could be revised to briefly summarize the key biological conclusions from prior MD studies alongside their technical context, which could then be revisited in their appropriate place alongside key results.*

We have modified the original fifth paragraph in the Introduction section and subdivided it into two separate paragraphs to emphasize the key biological conclusions in prior simulation studies.

“Molecular dynamics (MD) simulations have been employed to investigate the stability and conformational properties of monomeric and trimeric TMD. An early study of the trimeric TMD established a foundational understanding of the domain's stability, though it was limited by the computational resources available at the time (Kim et al., 2009). Subsequent work utilizing metadynamics found that the monomeric TMD is characterized by significant conformational plasticity and multiple metastable states, with the individual helix tilting in the bilayer and the midspan arginine (R696) interacting with lipid headgroups in either leaflet (Gangupomu et al., 2010; Baker et al., 2014). Baker et al. also simulated the monomeric TMD on Anton supercomputers, extended sampling to the multi-microsecond time scale, and demonstrated that TMD tilting and the interaction of R696 with lipids lead to local membrane thinning and water defects (Baker et al., 2014). Hollingsworth et al. modeled and simulated trimeric TMD in an asymmetric membrane and observed that TMD tilting and membrane thinning also occurred for the trimeric helical bundle, where water and ions permeated to stabilize the three positively charged R696 residues (Hollingsworth et al., 2018).

Piai et al. determined the NMR structure of a construct comprising the MPER, TMD, and CT, which currently serves as the only PDB structure to include the majority of the CT residues. They complemented this structural work with MD simulations to assess the structural stability of the trimeric MPER–TMD–CT complex (Piai et al., 2021). Recently, Majumder et al. simulated the same MPER–TMD–CT complex and applied a machine learning-based approach to classify the diverse conformational ensemble of the MPER-TMD-CT (Majumder et al., 2025). Maillie et al. combined conventional MD, steered MD, and coarse-grained simulations to demonstrate that interactions between MPER-targeting antibodies and membrane lipids are critical for effective epitope recognition (Maillie et al., 2025). In addition, MD simulations have been extensively applied to characterize the well-studied ectodomain.”

> *The authors have verified that PDB entries are cited at first mention, and this is noted. However, a recurring issue remains: key literature-supported conclusions appear in the Results and Discussion sections without accompanying citations at each point of use. Passages that summarize experimental or computational findings - particularly those used to validate or contextualize the authors' own results - require citation at every point of claim, not only at first introduction of a reference. This is not a minor stylistic preference. Downstream readers, systematic reviewers, and automated tools that map literature to claims (e.g., scite) rely on co-occurrence of claims and citations within the same passage. A citation appearing several paragraphs earlier does not carry attribution forward. As a practical example: the statement that "MPER-targeting antibodies bind effectively only after the gp120-gp41 trimer undergoes major conformational rearrangements toward a fusion-intermediate or post-fusion state (Frey et al., 2008; Alam et al., 2009; Chen et al., 2014; Lee et al., 2016)", which is appropriate. That same*

> *standard of inline attribution should be applied throughout - including in Results and Discussion subsections where prior experimental findings are mentioned without citation.*
>
> *Additionally, cited literature should be framed to highlight convergence with the authors' conclusions, not primarily to limitations of previous studies. Where prior studies independently support a finding, this should be stated explicitly. Independent replication across methods and systems is one of the strongest arguments for ground truth; treating it as such would improve the manuscript's scientific standing.*

In addition to summarizing the biological conclusions from prior simulation studies in our response to the previous comment, we have also added the following citations.

“Human immunodeficiency virus type 1 (HIV-1) is the most prevalent strain of HIV responsible for the development of acquired immunodeficiency syndrome (AIDS) (Sharp et al., 2011). The HIV-1 envelop (Env) consists of a host cell-derived lipid membrane and viral glycoproteins that play a crucial role in mediating viral entry into host cells. The Env glycoprotein is initially synthesized in the endoplasmic reticulum (ER) as a precursor gp160 and cleaved by furin into two subunits, gp120 and gp41. The non-covalently associated gp120–gp41 complex is transported to the cell surface in the form of a trimer, where it is subsequently incorporated into the envelope of nascent virions during viral assembly (Wyatt et al., 1998). The exposure of Env protein is essential for binding to the primary receptor CD4 and the co-receptors CCR5 or CXCR4, triggering membrane fusion and viral entry (Dalgleish et al., 1984; Feng et al., 1996; Huang et al., 1996). However, this exposure also renders the virus susceptible to immune attack. In response to host immune pressure, Env is densely coated with N-linked glycans added during post-translational modification in the ER and Golgi apparatus, which effectively shield vulnerable epitopes from immune recognition (Wei et al., 2003).”

“While MPER plasticity has been linked to its role in virus-host membrane fusion because it enables the ectodomain and TMD to adopt distinct orientations during large-scale structural rearrangements (Salzwedel et al., 1999), our results show that this flexibility is already inherently present in the prefusion state.”

“However, transition among these three states occur on millisecond-to-second timescales (Munro et al., 2014).”

> *Finally, the dynamical cross-correlation maps assess ectodomain-TMD coupling, and the authors appropriately acknowledge that microsecond simulations capture only the closed ground state. However, the revised manuscript does not address the question raised in the first review regarding CT-TMD and CT-ectodomain correlations. The Results section states that "very weak correlations between the ectodomain and the TMD" were found, but it is not clear whether the CT was included in this analysis or whether analogous correlation maps for CT-TMD and CT-ectodomain pairs were computed for the full-length systems. Additional analyses of the authors' deposited MD trajectories-such as probing for exposure of cryptic epitopes and potential allosteric coupling-could serve as valuable extensions of this work.*

We have updated the manuscript to address the correlations involving the CT. Figure 2—figure supplements 12 and 13 display the dynamical cross-correlation maps (DCCM) for the full-length systems (including the CT), which indicate low correlations between the ectodomain and the CT. We have modified the figure captions to explicitly state that the CT is included in these analyses. We have also clarified in the text that we do not further interpret the coupling of the CT with the other domains. As the Reviewer noted, the high structural heterogeneity of the CT makes defining consistent parameters (such as a tilt angle) impractical. Given this variability, along with the inherent uncertainty in the experimental structure of the CT, we believe it is important to avoid over interpreting these observations.

“Although Figure 2—figure supplements 12 and 13 also show low correlations between the ectodomain and the CT, we do not further interpret the coupling of the CT with the other domains due to its structural heterogeneity and the inherent uncertainty in its experimental structure.”

We have modified captions of Figure 2—figure supplements 10–13

> ***Recommendations for the authors:***
>
> ***Reviewer #3 (Recommendations for the authors):***
>
> *The authors have made meaningful progress in addressing first-round concerns. The remaining issues center on how prior literature is framed and integrated - not just cited - throughout the manuscript, consistent attribution at each point of claim, clarification of the CT correlation analysis, and major writing improvements. Addressing these points would substantially strengthen the manuscript's contribution to the field.*
>
> *Abstract*
>
> *"knowledge of the cytoplasmic tail (CT) is virtually absent" is overstated. While structural data for the CT are limited and largely uncertain, the CT has been extensively studied functionally and some NMR structural data exist (Piai et al., 2021; Murphy et al., 2017). Suggest revising to reflect that high-resolution structural information for the CT in the context of the intact trimer remains limited*

We have revised the abstract according to the Reviewer’s suggestion.

“While structural information is available for the membrane-proximal external region (MPER) and transmembrane domain (TMD), these regions remain comparatively understudied. Furthermore, high-resolution structural information for the cytoplasmic tail (CT), particularly within the context of the intact trimer, is limited and largely uncertain.”

> *Introduction*
>
> *The first paragraph is unreferenced. Foundational claims about HIV-1 biology, Env processing, and glycan shielding should carry at least landmark citations for readers new to the field.*

We have added references to the first paragraph.

“Human immunodeficiency virus type 1 (HIV-1) is the most prevalent strain of HIV responsible for the development of acquired immunodeficiency syndrome (AIDS) (Sharp et al., 2011). The HIV-1 envelop (Env) consists of a host cell-derived lipid membrane and viral glycoproteins that play a crucial role in mediating viral entry into host cells. The Env glycoprotein is initially synthesized in the endoplasmic reticulum (ER) as a precursor gp160 and cleaved by furin into two subunits, gp120 and gp41. The non-covalently associated gp120–gp41 complex is transported to the cell surface in the form of a trimer, where it is subsequently incorporated into the envelope of nascent virions during viral assembly (Wyatt et al., 1998). The exposure of Env protein is essential for binding to the primary receptor CD4 and the co-receptors CCR5 or CXCR4, triggering membrane fusion and viral entry (Dalgleish et al., 1984; Feng et al., 1996; Huang et al., 1996). However, this exposure also renders the virus susceptible to immune attack. In response to host immune pressure, Env is densely coated with N-linked glycans added during post-translational modification in the ER and Golgi apparatus, which effectively shield vulnerable epitopes from immune recognition (Wei et al., 2003).”

> *A paragraph break after "... and cytoplasmic tail (CT), are relatively understudied" would improve readability by separating the general context from the MPER/TMD-specific discussion that follows.*
>
> *A paragraph break before "Similarly, there are different conclusions about" would separate the TMD oligomeric state discussion from the MPER conformation discussion and improve navigation.*
>
> *A paragraph break after "Despite these advances, it remains challenging to investigate the gp120-gp41 trimer as an intact entity considering its structural complexity" would clearly delineate the literature context from the description of the present work.*

We have introduced paragraph breaks as suggested to improve the flow and readability of the introduction.

> *The biological rationale for simulating both cleaved and uncleaved systems should be stated explicitly in the Introduction. Readers unfamiliar with the furin cleavage biology and NFL trimer constructs will benefit from a sentence explaining why this comparison is informative.*

In the middle of the last paragraph in the Introduction section we have added

“While host furin cleavage of the gp160 precursor into gp120 and gp41 is a prerequisite for viral infectivity (McCune et al., 1988), native virions also incorporate a fraction of uncleaved gp160 (Zhang et al., 2021). Furthermore, many current immunogen designs, such as NFL and UFO constructs, utilize a covalent linker to stabilize the metastable prefusion conformation (Sharma et al., 2015; Kong et al., 2016). Therefore, we simulated both cleaved and uncleaved trimers to explore how the absence of proteolytic cleavage impacts the conformational landscape.”

> *The modifier “subsequently” in “Majumder et al. subsequently simulated...” implies temporal sequence and invites the inference that Majumder et al.'s work is less sophisticated or prior. Given that both works are recent and peer-reviewed, a neutral modifier such as “recently” or “independently” is more appropriate.*

We agree that a more neutral modifier is appropriate and have replaced “subsequently” with “recently” to avoid any unintended inference.

In the beginning of the sixth paragraph in the Introduction section we have modified

“Piai et al. determined the NMR structure of a construct comprising the MPER, TMD, and CT; to date, this is the only PDB structure including the majority of CT residues. They complemented this structural work with MD simulations to access the structural stability of the trimeric MPER–TMD–CT complex (Piai et al., 2021). Recently, Majumder et al. simulated the same MPER–TMD–CT complex and applied a machine learning-based approach to classify its conformational ensemble (Majumder et al., 2025).”

> *The sentence "Moreover, we selected several bNAbs targeting the epitopes across different regions of the Env protein and demonstrate that the simulation trajectories can be used to assess the epitope accessibility" implies that simulations of antibody binding were performed. This should be rephrased, for example: "Moreover, we selected various epitopes across Env that are targeted by bNAbs and demonstrate that the MD simulation trajectories can be used to assess epitope accessibility."*

At the end of the Introduction section we have modified

“Moreover, by analyzing epitopes targeted by various bNAbs, we demonstrate that the simulation trajectories can be leveraged to assess the epitope accessibility.”

> *The revised Methods section now cites van Meer et al. (2008) and Sampaio et al. (2011) as primary experimental sources for plasma membrane composition, which is appropriate. However, the Introduction still contains the statement: "we built a model of full-length gp120-gp41 trimer embedded in a lipid bilayer mimicking the lipid composition of the mammalian plasma membrane (Pogozheva et al., 2022)". This cites only the authors' own prior simulation study. A primary experimental reference (van Meer et al., 2008 and/or Sampaio et al., 2011) should be added here as well, so that readers encountering the claim in the Introduction have direct access to the supporting evidence.*

At the beginning of the last paragraph in the Introduction section we have modified

“In this work, we built a model of full-length gp120–gp41 trimer embedded in a lipid bilayer mimicking the lipid composition of the mammalian plasma membrane (van Meer et al., 2008; Sampaio et al., 2011; Ingolfsson et al., 2014; Pogozheva et al., 2022) (Figure 1).”

> *Additionally, a brief note in the Introduction on the cell type specificity of the plasma membrane model used (or its absence) would be informative, as membrane composition varies substantially across mammalian cell types and the choice has potential consequences for the conclusions.*

We have added a brief note clarifying that differences between the model membrane and the native viral envelope may influence the study's conclusions, particularly regarding protein-lipid interactions.

“We chose this composition as a representative baseline, though we acknowledge that the native viral envelope may exhibit a distinct lipid profile that could influence protein-lipid interactions.”

> *Results*
>
> *Connecting the observed accessibility frequencies to known neutralization potency, breadth, or escape propensity for each antibody class (PGT128, PG9, VRC01, 35O22, 10E8, 4E10) would provide a mechanistic framework and substantially increase the impact of this section. Even a brief discussion of how glycan shielding dynamics relate to reported neutralization sensitivity data would add value.*

We have expanded the Results section to include a comparison between our computational accessibility frequencies and established experimental metrics (potency and breadth).

At the end of each paragraph in the subsection “Ectodomain epitopes are conditionally accessible, whereas MPER epitopes are virtually inaccessible in the closed prefusion state” we have added

“The high accessibility frequency observed for the PGT128 epitope aligns with its exceptional potency. As demonstrated by Walker et al., PGT128 is capable of neutralizing approximately 72% of global isolates with a median IC_{50} of ~0.02 μg/mL. This potency is approximately 10-fold greater than that of PG9 and VRC01, though its breadth is lower than the 93% reported for VRC01 (Walker et al., 2011). This comparatively lower breadth may be attributed to strict sequence dependency. Because PGT128 recognition depends on the N332-centered glycan epitope, loss, truncation, or shifting of the N332 glycan to N334 prevents productive engagement regardless of local steric accessibility.”

“This is consistent with the lower neutralization potency and moderate breadth of PG9, which exhibits a median IC_{50} of ~0.22 μg/mL and a breadth of ~79% (Walker et al., 2009).”

"This intermediate accessibility is consistent with the biological requirement of the CD4 binding site to remain periodically available for receptor engagement while maintaining a certain degree of glycan shielding to evade neutralization. The potency of VRC01 is even lower than that of PG9, with a reported median $IC50$ of ~0.32 μg/mL, but it possesses an exceptionally high breadth of ~93% (Wu et al., 2010; Walker et al., 2011)."

"Altogether, these results demonstrate that epitope accessibility for this antibody is highly sensitivity to the membrane environment, glycan orientation and ectodomain tilting. This complex dependency provides a structural context for the experimental profile of 35O22, which exhibits high potency with a median IC_{50} of ~0.03 μg/mL, but a relatively limited breadth of ~62% (Huang et al., 2014)."

"Though differing in potency — with 10E8 exhibiting a median IC_{50} of ~0.35 μg/mL compared to ~1.93 μg/mL for 4E10 — both antibodies demonstrate extremely high breadth of ~98% (Huang et al., 2012). This extensive breadth is primarily attributed to the high sequence conservation of the MPER across global isolates. The negligible epitope accessibility observed in the prefusion trimer supports the conclusion that these antibodies require the transition of the Env trimer into intermediate states to fully engage their epitopes (Frey et al., 2008)."

> *The first paragraph of the Results section dives directly into trajectory notation without a brief summary of the simulation systems. A short opening paragraph (2-3 sentences) summarizing the number of systems, the variables tested (cleavage, CT presence, TMD position), and the total number of trajectories would orient the reader before the naming convention is introduced.*

We have moved the original first sentence in the Material and methods — Simulation details subsection to the beginning of the Results section. This sentence summarizes all the configurations we have considered and the number of independent trajectories for each configuration.

"The combination of cleavage state (cleaved vs. uncleaved), sequence length (full-length vs. CT-truncated), and initial TMD position in the membrane (high vs. low) resulted in eight distinct configurations, and we performed three independent 1-μs all-atom MD simulations for each configuration."

> *The statement "very weak correlations between the ectodomain and the TMD" leaves open the question of CT-TMD and CT-ectodomain correlations. If a tilt angle cannot be defined for the CT due to its structural heterogeneity, this should be stated.*

We have updated the manuscript to address the correlations involving the CT. Figure 2—figure supplements 12 and 13 display the dynamical cross-correlation maps (DCCM) for the full-length systems (including the CT), which indicate low correlations between the ectodomain and the CT. We have modified the figure captions to explicitly state that the CT is included in these analyses. We have also clarified in the text that we do not further interpret the coupling of the CT with the other domains. As the Reviewer noted, the high structural heterogeneity of the CT makes defining consistent parameters (such as a tilt angle) impractical. Given this variability, along with the inherent uncertainty in the experimental structure of the CT, we believe it is important to avoid over interpreting these observations.

"Although Figure 2—figure supplements 12 and 13 also show low correlations between the ectodomain and the CT, we do not further interpret the coupling of the CT with the other domains, considering its structural heterogeneity and the inherent uncertainty in its experimental structure."

We have modified captions of Figure 2—figure supplements 10–13

> *Throughout the Results, several long paragraphs could be broken up. In particular, the TMD section and the MPER exposure section each contain dense multi-example run-on paragraphs that would benefit from subdivision.*

We agree with the Reviewer and have introduced multiple paragraph breaks in the Results section to improve the flow and readability. In instances where longer paragraphs remain, they have been intentionally preserved to maintain the logical integrity of closely linked results, ensuring the reader can follow a single cohesive argument without interruption.

> *Discussion*
>
> *The statement "transition among three states occur on millisecond-to-second timescales" is an important claim that contextualizes the limitations of the microsecond simulations, but it is currently uncited. This should be attributed to the relevant experimental smFRET work (Munro et al., 2014 is cited in the preceding sentence, but not explicitly for this claim) and/or any additional literature that established these timescales for Env conformational switching.*

We have now explicitly attributed the claim regarding the millisecond-to-second timescales of Env conformational transitions to the relevant smFRET literature (Munro et al., 2014).

In the middle of the second paragraph in the Discussion section we have added

“However, transition among these three states occur on millisecond-to-second timescales (Munro et al., 2014).”

> *The Discussion contains several extended paragraphs that could be subdivided to improve readability and help the reader navigate between distinct topics (e.g., MPER flexibility, CT effects, coupling, lipid composition, antibody accessibility).*

We have subdivided the Discussion section as suggested by the Reviewer to improved readability.

https://doi.org/10.7554/eLife.110107.3.sa0